Mechanics of Size and Dimensionality Effects in Metal Plasticity

by

Benjamin A. Szajewski

B.S., Rensselaer Polytechnic Institute, 2010
Sc.M., Brown University, 2013

A dissertation submitted in partial fulfillment of the requirements for the Degree of Doctor of Philosophy in the School of Engineering at Brown University

Providence, Rhode Island
May, 2016

This dissertation by Benjamin A. Szajewski is accepted in its present form by the School of Engineering as satisfying the dissertation requirement for the degree of Doctor of Philosophy.

Date_____ _____

William A. Curtin, Director

Recommended to the Graduate Council

Date_____ _____

Huajian Gao, Reader

Date_____ _____

Nitin Padture, Reader

Approved by the Graduate Council

Date_____ _____

Peter M. Weber, Dean of the Graduate School

Vita

Ben Szajewski was born in Rochester, New York on November 7^{th}, 1984. The frigid, cold winters of upstate New York allowed Ben the ideal environment to grow and learn. Ben found he was most suited to engineering and subsequently, he moved to Troy, New York, where he completed a B.S. in Mechanical Engineering at Rensselaer Polytechnic Institute in May, 2010. His continued enthusiasm for Mechanical Engineering led him in pursuit of a PhD in Solid Mechanics at Brown University starting in the Fall of 2010. Upon learning that his adviser was moving abroad in 2011, the only natural choice was for Ben to follow. Therefore, in early 2012 Ben, while still a student at Brown, moved to Switzerland to continue his work with Professor William A. Curtin on dislocation mechanics related problems, where he has been ever since (mostly).

Acknowledgements

First, I would like to express my utmost gratitude to my adviser, Professor William A. Curtin. Without his encouragement and inspiration this thesis would not have been possible. I would also like to extend my most sincere thank you to Professors Huajian Gao and Nitin Padture for agreeing to serve as my thesis readers and defense committee members. The Brown mechanics community and School of Engineering also are owed a well-deserved thank you for making my limited time there a wonderful learning experience and one in which I will always remember.

Second, I am forever indebted to Professors David Bacon and Wei Cai for their countless journal articles from which I learned many of the subtleties of dislocation theory. As well, I would like to thank Professor Alan Bower for his online Linear Elasticity lecture notes. I would also like to extend a thank you to Professors Jon Dantzig, Srinath Chakravarthy, John Wadach and Antoinette Maniatty for being a constant source of inspiration throughout my research.

Third, I would like to thank Pradrag for printing the thesis submission paper. Without him this would not have been possible. I would also like to thank Yinfeng Li, Sara Kadkhodaei, and Dibakar Datta for making my limited time at Brown University unforgettable and overall an enjoyable experience. While in Europe, I was fortunate enough to make a number of friends as well, some of whom deserve a thanks. In particular a number of flat mates in Lausanne, Liran Weiss, David Lasry, Petra Zvárová, Lena Woodward, Suzy Greenberg and and Isha all made my stay here more enjoyable. As well, at EPFL Nassima Nasri and Nicolas Chobaut and Tom Marshall and Harry Hood will be remembered for reminding me where to go when the lights go out.

Fourth, I am forever indebted to the ever circulating army of postdocs Dr. Curtin has under his reign. In unison with my readings, they have provided a very general knowledge otherwise beyond the scope of my immediate research. As well, several of his students have made a lasting impression on me. Explicitly

these are Yi Dong, Fabio Pavia, Sutee Olarnrithinun from Brown and Mostafa, Ali, Max and Wolfram from EPFL. I am very fortunate to have interacted with all.

Last, and most importantly, I need to thank my family. Without their support and love, this could not have been possible.

Contents

List of Tables

List of Figures

Chapter 1

Introduction

Historically, metals and in particular alloys have served as candidate materials [1–4] for a variety of structural and electronic applications. With the inception of the Bronze Age the benefits of alloying (copper and tin) to produce a mechanically superior metal were discovered [1]. By the second millennium BC, developments in ferrous metallurgy were under way across a wide range of cultures in both the near and middle east [4]. Finally, written documentation in the 16^{th} century AD [3] described (in detail) modern mining, smelting, extraction and metallurgical methods of the time. While centuries of research have greatly advanced our knowledge in the realm of processing versus mechanical property relationships of metals a multitude of unanswered, and valuable questions remain. Understanding the relationships between alloying elements, processing, and the resulting macroscopic properties is of central interest across a variety of industries such as the aerospace, semiconductor, and automotive sectors.

Upon discovery that metals consisted of periodic, organized arrangements of atoms forming a crystalline structure attention immediately turned to directly estimating their strength. Among the simplest models of (perfect) crystal strength derived was that by Frenkel [5]. Frenkel postulated that under an applied shear stress (τ) a perfect crystal would undergo a sinusoidal lattice energy potential and in turn an equivalent shear response with amplitude τ_{flow} and period b, i.e.

$$\tau = \tau_{flow} \sin\left(\frac{2\pi x}{b}\right) \tag{1.1}$$

Under the same applied shear stress (τ) for sufficiently small shear strain ($x/d << 1$) a linear stress-strain relation in shear must hold:

$$\tau = \mu \frac{x}{d} \tag{1.2}$$

where d is the atomic inter-planar spacing. Combining 1.2 and 1.1 (in the small-strain limit) then leads to an estimate on the order of the shear modulus for the ideal strength of a perfect crystal.

$$\tau_{theo} \approx \mathcal{O}(\mu) \tag{1.3}$$

Despite its elegance, this predicted flow stress of metals drastically differs from experimental observations. Experiments dating back to the $\sim$ 1960s [6] have led to a true flow stress of metal on the order of $\sim 10e^{-9}\mu$. A factor of 10^9 therefore exists between the (simple) initial estimates of Frenkel outlined above and experiments. Several opposing theories were postulated to explain this discrepancy.

Unrelated to crystals, shortly after the turn of the century Volterra [7] and other elasticians were working on problems involving the stress distribution in elastic cylinders with various displacement-jump boundary conditions. It was only after nearly 30 years that the existence of mechanical defects (i.e. dislocations) was postulated, and suggested as a possible explanation and mechanism for the greatly reduced flow stress measured in experiments. Qualitatively the basic concept was that at experimentally observed flow stresses (τ_{flow}) plastic deformation was accommodated entirely by the motion of line defects (termed dislocations). While the initial structures envisioned by Volterra were a rather crude approximation to the dislocation types of structures that researchers currently study both computationally and experimentally, the concept paved the way for further

discovery.

Miraculously years after the concepts introduced by Vito Volterra, experiments successfully verified both the existence of dislocations, and their central role in the deformation of metals. With the notion of dislocations governing plastic flow, it folllows naturally that inhibiting their motion translates to observable macroscopic strengthening and hardening. Solutes, "*forest*" dislocations and other inhomogeneities are all known to be sources of enhanced strength or ductility. Often however these relationships are understood in only a qualitative way at best, and so intense research efforts targeted at strengthening and building a more quantitative understanding of these processes are a continuing phenomenon.

The scope of this thesis is therefore targeted at developing a better understanding of the fundamental mechanisms of plastic flow in *spatially confined* systems where both the size and geometry of the structure have a marked influence on the flow stress of the material. Also of interest is the basic energetics of dislocations, and how changes in both length and orientation lead to self-restoring forces (e.g. Line Tension).

1.1 Basics of Dislocation Theory

In order to provide the necessary background for the subsequent chapters in this thesis, several of the basic concepts of dislocation theory are relayed here. The simple dislocations as envisioned by Volterra are created as follows. An otherwise pristine crystal is envisioned to experience a constant, planar slip of magnitude $\mathbf{b}$ which terminates abruptly within the specimen. The point of abrupt termination is then the location of the dislocation (at x_0) where the gradient of the displacement discontinuity is infinite at the point of termination, and the magnitude of the displacement discontinuity is a single Burgers vector, defined as

$$\mathbf{b} = \int_{-\infty}^{+\infty} \frac{\partial \mathbf{u}}{\partial x} \mathrm{d}x \tag{1.4}$$

where

$$\frac{\partial \mathbf{u}}{\partial x} = \mathbf{b}\delta(x - x_0) \tag{1.5}$$

and $\delta(x - x_0)$ represents the usual delta function. Equivalently eq. 1.4 can be written as a contour integral around the defect in which case it is referred to as a Burgers circuit. The relationship between the (plastic) displacement vector ($\mathbf{u}$) and the line of displacement termination (i.e. the "*line* direction, $\mathbf{t}$) defines the dislocation character. For a *perfect* edge dislocation the displacement vector is perpendicular to the line direction ($\mathbf{b} \cdot \mathbf{t} = 0$) and for a *perfect* screw dislocation the two directions are parallel (i.e. $\mathbf{b} \cdot \mathbf{t} = ||\mathbf{b}||$).

Given these simple, idealized models where the dislocation is said to be "*singular*" the field equations of linear elasticity become soluble and quantitative analyses involving dislocations become plausible. Following elementary linear elasticity theory a screw dislocation displacement field follows the Laplace equation i.e.

$$\nabla^2 \mathbf{u} = 0 \tag{1.6}$$

The solution to this equation (for a dislocation oriented along the z-axis) in polar coordinates which then satisfies the jump displacement boundary condition is [8]

$$u_z(r, \theta) = \frac{\theta b}{2\pi} \tag{1.7}$$

Given this displacement field, the stress field then follows from differentiation and multiplication by a constant shear modulus, which in polar coordinates is

$$\sigma_{\theta z} = \frac{\mu b}{2\pi r} \tag{1.8}$$

Similar analyses can be applied to the edge dislocation. The only caveat is that because the the displacement field of a screw dislocation is by definition an anti-plane strain problem, it satisfies the Laplace equation making its solution considerably less complicated. The edge dislocation is by definition a plane strain problem, and

so one method of solving for the edge dislocation stress and displacement fields is to use Airy functions [8]. The end result however leads to qualitatively similar stress fields ($\sim \frac{\mu b}{r}$).

Finally the energies (per unit length) contained within a finite linear elastic cylinder with inner and outer radii ρ and R can then be obtained by integrating the strain energy density ($\boldsymbol{\sigma} : \mathrm{d}\boldsymbol{\epsilon}$) which scales with the square of the stress fields, i.e.

$$\frac{W_{el}}{L} = \int_{\rho}^{R} (\mathrm{d}V)(\boldsymbol{\sigma} : \mathrm{d}\boldsymbol{\epsilon}) \tag{1.9}$$

The end result for both the (infinite, straight) screw and edge dislocation depends only on both the inner and outer cutoff radius (ρ, R) and the angle between the Burgers vector and the line direction (ϕ) and is given by

$$\frac{W_{el}}{L} = \frac{\mu b^2}{4\pi(1-\nu)} \left(1 - \nu \cos^2(\phi)\right) ln \left(\frac{R}{\rho}\right) \tag{1.10}$$

One subtle feature of this result is the "*hollow*" nature of the dislocation core (i.e. $r < \rho$). Recognizing that atomic displacement gradients are indeed the greatest near and within the dislocation core what is frequently done is to add a core energy term ($\frac{W_{tot}}{L} = \frac{W_{el}}{L} + W_{core}$), the details of which remain an intense area of research, which is partially the subject of this thesis.

1.2 Frank-Read Sources, Dislocation Pileups and Hall-Petch

Under laboratory conditions pristine, or nearly perfect crystals, can be "*grown*" with dislocation densities near 0 [9]. However under plastic deformation dislocation densities are known to grow up to $\sim 10^{16}/m^2$. Therefore mechanisms must exist to accommodate this rapid growth in dislocation density under plastic deformation. These mechanisms are known as dislocation sources, and they take a

variety of forms, however in all cases they serve as a point of dislocation multiplication. While a variety of different dislocation multiplication mechanisms must exist, it is often difficult to assess accurately which mechanism (if any) is dominant in a given mode of deformation [8]. One of the classically known (and studied) mechanisms however is the Frank-Read (FR) source which is the subject of part of this thesis. It is therefore worthwhile to review the basic mechanics of a FR source in terms of what the typical operation criteria is, how they "*produce*" dislocations and their role in macroscopic plasticity.

FR sources are typically formed by an otherwise mobile dislocation becoming pinned, whether by forest dislocations, other inhomogeneities and obstacles, or by cross-slipping type mechanisms. In all of these cases the result is a dislocation segment of length l pinned between two obstacles. Under an applied shear stress (τ_{app}) the dislocation begins to bow-out by glide in an effort to minimize the potential equation

$$\Pi = \int_S \Gamma \mathrm{d}S - \int_A \tau_{app} b \mathrm{d}A \tag{1.11}$$

where Γ in the first term is the "*line tension*" which will be detailed in a subsequent section, and the second term is the interaction energy (which is dissipated) between the applied field and the termination of the displacement discontinuity of the dislocation. A competition therefore exists between the energy dissipated in bow-out of the dislocation and the energy gained in increasing the length of the dislocation due to Γ. In the regime where $\tau_{app} < \tau_{crit}$ a series of stable bow-out solutions exist where the bowed-out dislocation forms an arc with an approximately constant radius that scales inversely with the applied field ($R \sim \tau_{app}^{-1}$). Beyond a critical stress, once $\tau_{app} \geq \tau_{crit}$ there is no longer a stable solution for eq. 1.11 and so the dislocation begins to loop around on itself. Once the unstably expanding dislocation has formed a near complete arc which completely encircles the initial pinning points it annihilates along a small portion of the length forming both a complete dislocation loop, completely removed from the source and simultaneously

reconstituting the source. The isolated loop then continues to expand to dissipate energy. The exact solution for $\tau_{crit} = \tau_{crit}(\mu, b, \Gamma, l)$ obviously depends on the exact value of Γ which in-turn depends on the nominal dislocation orientation (ϕ), l, and the inner cutoff parameter (ρ). Given all of these intricacies the estimate

$$\tau_{crit} \approx \frac{\mu b}{l} \tag{1.12}$$

has often been used with a certain level of success.

While FR sources provide a simple mechanism to understand the increase in dislocation density under an applied load, they, alone, do not contribute to or explain any hardening behavior. One of the simplest mechanisms responsible for a hardening effect are dislocation pileups. Whether due to the presence of a grain boundary, an obstacle, or other forest dislocations some inhomogeneity serves to locally inhibit flow on a certain slip plane, and in the simplest models is infinite along the out-of-plane direction and so the source is considered to emit dipoles. If that same slip plane contains a dislocation source (such as the FR source above), and sufficient shear stress to operate the source (τ_{crit}), the source will indeed begin to operate as described above. However as dislocations are emitted they will eventually approach the inhomogeneity. Because the source of the pileup will locally prevent flow, but simulatneously each dislocation (of the same sign) is repelled from each of the other dislocations the result is a dislocation *pileup* on one side of the inhomogeneity, where (i) the applied shear stress, (ii) the local stress fields of the inhomogeneity, and (iii) the interaction amongst each of the dislocations within the *pileup* creates an equilibrium dislocation distribution.

Among the simplest models of a pileup is quantified as follows. Consider a *pileup* as described above, except where a leading dislocation is effectively rigidly pinned and all of the other (N-1) dislocations between the source and the pileup are held in equilibrium by the applied field, the pinned dislocation and the interaction with each of the other dislocations. The change in interaction energy for any perturbation of any one of the unpinned dislocations must be balanced by the linear

dependence of the interaction energy between the applied field and the dislocation on the dislocations position. Thus, for each of the unpinned dislocations

$$\tau_{app} b - \frac{\partial W_{int}}{\partial x_i} = 0 \tag{1.13}$$

where i = 1,2,...(N-1) unpinned dislocations in the pileup. Because this relationship has to hold for all of the N-1 *free* dislocations in the pileup, and because an additional shear stress τ_{app} is applied to the leading dislocation, the force (per unit length) on the leading dislocation in the pileup is then [8]

$$\frac{F}{L} = \tau_{app} N b \tag{1.14}$$

Frequently in simple models of flow in the presence of grain boundaries, or other inhomogeneities it is assumed that the pileup has a critical strength, beyond which it will break. It follows that the criteria for flow is $\frac{F}{L}\big|_{\tau_{app}=\tau_{crit}} = \frac{F_{crit}}{L}$.

Next it is conceptually worthwhile to consider the distribution of dislocations within the pileup. Simple dimensional arguments lead to a scaling relation for the dislocation density (dislocations per unit length) as [8]

$$\eta(\frac{x}{l}) \propto \frac{\tau_{app}}{\mu b} \tag{1.15}$$

The density may be integrated over the total length of the *pileup* to obtain the total number (N) of dislocations within the *pileup* as

$$\begin{aligned} N &= \int_l \eta(\frac{x}{l}) \mathrm{d}x \\ &\propto \frac{\tau_{app} l}{\mu b} \end{aligned} \tag{1.16}$$

As originally discovered by Hall [10] and shortly thereafter by Petch [11] the yield stress of metals scales inversely with the square root of the grain size ($\tau_{crit} \sim l^{-1/2}$). These initially experimental scaling observations have consistently proven

so robust and reliable that a general consensus exists that there must be some direct, physical, rationalization for them. One simple argument which has been successful in reproducing a multitude of data is the combination of an active FR source confined within a grain. By considering a pileup generated by an FR source where eq. 1.14 determines the stress at the head of the pileup, substituting eq. 1.16 in to eq. 1.14, and then solving for τ_{crit} yields a critical flow stress which scales inverseley with the grain size (l) as

$$\tau_{crit} \propto l^{-1/2} \tag{1.17}$$

In reality however what is observed experimentally is that for sufficently large grains the critical resolved flow stress (τ_{crit}) saturates to some constant value (τ_0). The Hall-Petch equation in its celebrated form then reads

$$\tau_{crit} = \tau_0 + \frac{K}{\sqrt{d}} \tag{1.18}$$

where d is the grain size. A number of competing theories exist to rationalize the τ_0 term [8]. One possibility is that it is a friction stress which is necessary to generate flow, independent of grain size. This possibility however remains slightly nebulous because thermal activation and creep type events would overcome any friction stresses on macroscopic time scales at or near room temperature. A second possibility which is widely believed to be more likely, however remains experimentally inaccessible, is that it represents the interactions between strong pinning points and un-nucleated dislocations [8]. More sophisticated models with underpinnings in the simple Hall-Petch analysis remain a very much active area of research.

1.3 Modeling of Strengthening Mechanisms and Dislocation-Obstacle Interactions

While the interactions between dislocations and other inhomogeneities (e.g. grain boundaries, inclusions, solute atoms, etc.) are known to be important in characterizing a materials behavior, as demonstrated in the example(s) above, until quite recent, studies have been limited either to experiments, which are quite complex to analyze, or simple theoretical models that require many assumptions in order to remain analytically soluble. Until quite recently, work was hindered to approximate analytical methods which require a host of a priori assumptions, some of which remain to be validated. Examples of necessary approximations include isotropy, 2d dislocation dipoles, linear elasticity and completely phenomenological rules for local dislocation interactions. Despite significant insights gained from both analytical approaches, as well as experiments a continued discrepancy between experiments lacking a full analysis and theory with perhaps over simplifications of important details has remained.

With the advent of modern, fast, parallel computation however a variety of methods have emerged to reduce the gap between theory and experiment noted above. Parallel computations have led to a host of new insights in metal plasticity over the past several decades. Perhaps one of the most powerful tools for investigating plastic phenomena are Molecular Dynamics (MD) Simulations [12]. These simulations rely on solving Newton's equations for very many interacting particles (on the order of millions), however the interactions between the particles are governed by a *user-input* (in the form of an interatomic potential) and so the final outcome of the simulation can be very dependent on the interatomic potential used [13].

Of particular interest to the computational materials science community within the field of dislocations and plasticity are *dislocation-obstacle* interactions where MD is used to explicitly treat the local interactions between dislocations and inho-

mogeneities without all of the *ad-hoc* assumptions listed above. Examples of this include, but are not limited to (i) interactions with inhomogeneities (such as voids [14–20] and other dislocation loops [21, 22]), (ii) solute strengthening [23, 24], and (iii) interactions with grain boundaries [25–32]. All of these simulations have several features in common. First, because both the cost and the volume of these simulations scales with the number of atoms in the simulation, MD simulators are typically motivated to use *enough* atoms, but not much more. The strict definition of "*enough*" of course varies widely throughout the field and is a subject of a latter part of this thesis. Second, because very small time steps are required for these simulations unrealistically large strain rates must be used which require a certain level of care and analysis to ensure that the data generated from such simulations can be meaningfully interpreted within the context of physically realistic strain rates. Third, because finite, small volumes have to be used, interfaces are effectively introduced in to the simulation which can unduly influence the mechanical behavior which is supposed to be the topic of investigation. This, as well, is a topic covered in the latter part of this thesis and is an extension of the classical "*image effects*" analysis as presented in Hirth and Lothe [8].

1.4 The Force to Bow-Out a Dislocation

Of, perhaps, the most fundamental significance both in dislocation theory and in MD simulations of "*dislocation-obstacle*" interactions is the "*Line Tension*" (subsequently referred to as Γ) of a dislocation. Quantitatively, this single parameter describes the incremental change in energy for an incremental change in dislocation line length i.e.

$$\Gamma = \frac{\delta W}{\delta S} \tag{1.19}$$

The simplest realization of this is the "*small bow-out*" model as described in chapter 5. This single parameter however is ubiquitous to all levels and applications

of dislocation theory.

One example, which becomes immediately apparent, in the subsequent chapter (2) is the line tension in numerical simulations of discrete dislocations. Due to the singular, and inelastic nature of the dislocation core whether the cutoff procedure of Hirth and Lothe [8] or the more recent Non-Singular Theory by Cai et al. [33] is employed a numerical value must be chosen for the cutoff parameter used. While this will be explored in depth in chapter 5, it will become apparent that the only way to accurately calibrate *higher-level* DDD models to *lower-level*, higher fidelity numerical simulations (such as MD, or DFT) is to choose the cutoff parameter to match the line tension on both scales. The known DDD code `ParaDiS` [34] contains an artifact of a cutoff parameter, as well the older DDD code `MicroMegas` [35] contains an explicit line tension term, both of which must be calibrated against a more accurate dislocation simulation method such as MD for DDD to even begin to match MD results.

Numerical fitting procedures aside, the line tension of a dislocation has also been used successfully in a number of predictive analytical models [23, 36, 37]. All of these models rely on the *Line Tension* as a fundamental parameter, and measure of the force required for flow and to operate an FR source, as described above. Consequently, phenomenological values, as are typically used, in the absence of lower scale data (MD, DFT), such as $\sim (1/2)(\mu/b^2)$ can drastically hinder the accuracy and predictability of such models.

1.5 Outline and Scope of Thesis

The purpose of the introduction given above is to (i) motivate further research in to dislocations (and this thesis), (ii) provide a literature review of the current state-of-the-art and more so (iii) provide some of the background details necessary for the comprehension of this thesis. The above text is not meant to be a comprehensive development of the theory of dislocations, and for this the reader

is referred to such texts as Hirth and Lothe The Theory of Dislocations [8] and, more recently Computer Simulations of Dislocations [38]. What is hopefully conveyed by the introduction however is that many of the current hurdles existent in technological evolution, both in the development of futuristic structural materials, and electronic materials are very much metallurgical problems, at the nucleus of which is dislocations. While the past century has in fact provided a wealth of knowledge about dislocation-based mechanisms in metals and alloys there still remains a large gap in our understanding of all of the key processes associated with plastic deformation. Most importantly, it has been demonstrated that in structural materials systems where geometric lengths approach the order of internal length scales associated with dislocations, such as Burgers vectors, and distances between other inhomogeneities, conventional, size-independent descriptions of plasticity fail. This scope of this thesis is to bring a level of quantitative understanding to several of these phenomena by way of example.

In summary, the accomplishments of this work are (i) the demonstration of size and dimensionality effects in metal plasticity where a purely continuum description lacking any material length scale is insufficient to describe the plastic behavior, and (ii) the reconciliation of discrepancies between a continuous elastic (DDD) line tension model and that computed directly from Molecular Statics Simulations. These accomplishments are detailed through the remainder of this thesis, which is organized as follows. Chapter 2 focuses on the basics of Discrete Dislocation Dynamics (3d-DDD) simulations and provides a background for the simulations which are referred to in subsequent chapters. Chapter 3 focuses on the operation of a Frank-Read (FR) source in a linearly varying stress gradient where the magnitude of the gradient serves as the key length scale. Unlike a conventional FR source it is found that a new series of stable configurations exist, and that the source stress required for nucleation of additional dislocations becomes linearly dependent on both the relevant length scale of the stress gradient and on the number of already emitted dislocations. Chapter 4 focuses on an application of a

thin film mechanics problem where the thickness of the film is the critical dimension controlling the size-dependent plasticity. In this case, the affected material volume is that of a Molecular Dynamics simulation cell, and so the size-effect manifests itself in terms of spurious image forces acting on dislocations. A smaller is stronger effect is present. Chapter 5 focuses on dislocation line tension calculated both (i) by Molecular Statics simulations and then (ii) as computed using linear elastic line tension models. The two are shown not to match in the coefficient of the natural logarithm of the scaling with the obstacle spacing. The difference is rationalized through nonlinear lattice type effects, which prevent the continuous, smooth bow-out resulting from elasticity. Finally in Chapter 6 a summary and conclusion is provided along with recommendations for future work.

Chapter 2

3d Discrete Dislocation Dynamics (3d-DDD)

Throughout this work elastic analyses of discrete dislocations of both an analytical and a computational nature are applied to a series of physically motivated problems. While the analytical aspects are treated directly in the text a level of familiarity with the methodology of 3d Discrete Dislocation Dynamics (3d-DDD) is assumed. Therefore, to aid in the understanding and interpretation of future chapters it is of value to briefly review the fundamental concepts and ingredients contained within a 3d-DDD simulation. Much of the numerical analyses contained within this thesis rely on the 3d-DDD code `ParaDiS`[34, 39] as well as an in-house DDD code which follows similar algorithms and so the theory and implementation presented in this chapter is written particularly from that vantage point. With that said however, it is kept sufficiently general so as to be applicable to most DDD codes used within a research enviornment.

2.1 Discretization

Omnipresent in any DDD code is a method for representing and cataloguing a potentially complex, continuous network of dislocations. This is typically achieved through a discretization method where continuous lines of dislocations are divided

in to a series of segments (with line direction $\mathbf{t}$) interconnected by nodes. In addition each segment must be assigned both a Burgers vector ($\mathbf{b}$) and a glide plane (with direction normal $\mathbf{n}$). Therefore the position of two (interconnected) nodes, a Burgers vector, and a plane-normal fully describe a discrete dislocation segment. Because some ambiguity exists in the sign of $\mathbf{t}$ for a given dislocation segment a conservation law must be enforced (consistent with the line sense dictated by a Burgers circuit) such that at each node the sum of the Burgers vectors "*entering*" the node from adjacent segments must equal the sum of the Burgers vectors "*exiting*" the node from adjacent segments, or

$$\sum_k sgn(\mathbf{t}_k^{ij} \cdot \mathbf{t}_k^{12})\mathbf{b}_k = 0 \tag{2.1}$$

where k spans over the segments connected to a node and the argument of the *sgn* functions returns a +1 for a segment with starting node 1 and end node 2 (e.g.. ij=12) *entering* the node, and a -1 for a segment with starting node 2 and ending node 1 (e.g. ij=21) *exiting* the node.

2.2 Dislocation Energetics, Stresses, and Nodal Forces

Once an entire dislocation network has been catalogued and discretized as described above forces must eventually be computed and projected on to nodes in order to evolve the system through time. However, prior to the discussion of forces acting directly on segments (or nodes) it is of value to reproduce the energetics of dislocation interactions with (i) other dislocations, (ii) externally applied stresses, and (iii) "*core*" interactions recognizing that it is the spatial difference in these terms with respect to the rotation and translation of segments that leads to a force. As derived in Hirth and Lothe [8] the elastic interaction energy between two continuous loops with each differential segment separated by $R \equiv ||\mathbf{x}_1 - \mathbf{x}_2||$ may be expressed as

$$
\begin{aligned}
W_{el} = &- \frac{\mu}{2\pi} \oint_{C1} \oint_{C2} \frac{(\mathbf{b}_1 \times \mathbf{b}_2) \cdot (\mathrm{d}\mathbf{l}_1 \times \mathrm{d}\mathbf{l}_2)}{R} \\
&+ \frac{\mu}{4\pi} \oint_{C1} \oint_{C2} \frac{\mathbf{b}_1 \cdot \mathrm{d}\mathbf{l}_1)(\mathbf{b}_2 \cdot \mathrm{d}\mathbf{l}_2)}{R} \\
&+ \frac{\mu}{4\pi(1-\nu)} \oint_{C1} \oint_{C2} (\mathbf{b}_1 \times \mathrm{d}\mathbf{l}_1) \cdot \mathbf{T} \cdot (\mathbf{b}_2 \times \mathrm{d}\mathbf{l}_2)
\end{aligned}
\tag{2.2}
$$

where

$$
\mathbf{T} = \frac{\partial^2 R}{\partial \mathbf{x} \partial \mathbf{x}}
$$

It is clear by inspection of the above (eq. 2.2) that the integrals diverge as $\lim_{\mathbf{x}_1 \to \mathbf{x}_2} R = 0$. In the DDD code `ParaDiS`, for example, this is circumvented by a modified interaction energy, which, in the near-field is finite with $\lim_{\mathbf{x}_1 \to \mathbf{x}_2} R_a = a$. This is achieved by substituting $R \equiv R_a$ where $R_a = \sqrt{R^2 + a^2}$ as detailed in the Non-Singular theory by Cai and coworkers [33]. While expression 2.2 was initially derived for loops, it has been demonstrated [8] that its piecewise application to segments as discussed here and reproduced in closed form in [8] is entirely appropriate.

Similarly, the incremental change in interaction energy between an externally applied field (σ_{app}) and a discrete dislocation segment for an incremental displacement of the discrete dislocation segment (of length $\mathrm{d}\mathbf{l}$) [8] is

$$
\delta W_{ext} = \oint_C [(\mathbf{b} \cdot \sigma_{app}) \times \mathrm{d}\mathbf{l}] \cdot \delta \mathbf{r} \tag{2.3}
$$

where the integral is taken along the segment and $\delta\mathbf{r}$ represents the incremental advance of the segment.

Finally, the dislocation-self interaction energy of a discrete dislocation segment requires some discussion because of the unphysical elastic singularity located at the dislocation core. The approach taken within `ParaDiS` [34] as well as the approach followed where necessary throughout this work is to assume an additional, local *core-energy* (E_{core}) which scales exactly as elasticity with respect to the ori-

entational dependence of the energy of the segment. Therefore the energy cost associated either with a longitudinal displacement of a node (elongation), or a torque of a discrete dislocation segment scales exactly as elasticity with the exception of the prefactor, E_{core} exactly replacing $\mu/(4\pi)$ and the omission of the *log* term. In the interest of completeness, the relevant *core-energy* of a discrete dislocation segment per unit length (with orientation $\phi = \arccos(\mathbf{b} \cdot \mathbf{t})$) is [40]

$$\frac{W_{core}}{L} = \frac{E_{core} b^2}{(1-\nu)} \left(1 - \nu \cos^2(\phi)\right) \tag{2.4}$$

Once the elastic interaction energy between all of the segments, the interaction between the applied field and the segment, and the dislocation-self interaction energy of the entire system is computed, using either the Non-Singular theory [33] or the conventional elastic interaction energy equations [8] the vectorial force acting on a node is then soluble by computing the incremental change in the elastic interaction energy of the system for an incremental change in the position of the node ($\delta\mathbf{r}$) and follows as

$$\begin{aligned} \mathbf{f} &= -\frac{\partial W}{\partial \mathbf{r}} \\ &= -\frac{\partial [W_{el} + W_{ext} + W_{core}]}{\partial \mathbf{r}} \end{aligned} \tag{2.5}$$

While the first term in 2.5 is cumbersome and so is not reproduced here, the second and third terms yield a certain level of insight and are referred to later in the text, and so are expanded upon here. The force produced by an externally applied stress (also known as the Peach-Koehler Force [41]) is

$$\mathbf{f}^{app} = (\boldsymbol{\sigma} \cdot \mathbf{b}) \times \mathrm{d}\mathbf{l} \tag{2.6}$$

The core energy, as noted above, produces both a longitudinal force (due to change in length) and a torque-like force (due to change in orientation). Each of these are found by taking the respective derivatives, and are given by

$$\begin{aligned}\mathbf{f}_l &= \frac{E_{core}b^2}{(1-\nu)}\left(1-\nu\cos^2(\phi)\right)\\ \mathbf{f}_t &= \frac{E_{core}b^2}{(1-\nu)}\left(2\nu\cos(\phi)\sin(\phi)\right)\end{aligned} \tag{2.7}$$

Utilizing the above expressions forces can be directly computed on nodes by considering the net change in the system energy for infinitesimal displacements of each node. This procedure for computing forces indirectly from energies as outlined above is an unnecessarily cumbersome burden, however, and so in practice and with respect to what is implemented both in `ParaDiS` and in our in-house DDD code forces are computed directly from a pre-computed stress tensor which in turn is evaluated at only a finite number of points along the discrete dislocation network. Using the Non-Singular theory [33], the stress tensor for a discrete dislocation segment is given by (following the work of Cai and Bulatov [39])

$$\begin{aligned}\sigma_{\alpha\beta}(\mathbf{x}) = &\frac{\mu}{8\pi}\oint_C \partial_i\partial_p\partial_p R_a(b_m\epsilon_{im\alpha}\mathrm{d}x'_\beta + b_m\epsilon_{im\beta}\mathrm{d}x'_\alpha)\\ &+\frac{\mu}{4\pi(1-\nu)}\oint_C b_m\epsilon_{imk}(\partial_i\partial_\alpha\partial_\beta R_a - \delta_{\alpha\beta}\partial_i\partial_p\partial_p R_a)\mathrm{d}x'_k\end{aligned} \tag{2.8}$$

Similar expressions exist within Hirth and Lothe [8], chapter five. The resulting expressions, i.e. 2.8 and σ_{app} provide a direct way to compute the stress at any point (or on any segment) within the material. The (Peach-Koehler) force acting on every differential segment ($\mathrm{d}\mathbf{l}$) which then must be projected on to nodes is then given by:

$$\mathbf{f}^{PK}(\mathbf{x}) = (\boldsymbol{\sigma}(\mathbf{x})\cdot\mathbf{b})\times\mathrm{d}\mathbf{l} \tag{2.9}$$

Obviously, evaluating eq. 2.9 directly on nodes *only* is unphysical, as well, eq. 2.9 cannot be evaluated continuously, or even near continuously along each line segment due to excessive computational cost and so we adopt a simple linear in-

terpolation scheme as follows. In the simplest case (as implemented within our in-house DDD code) we assume that the nodes are sufficiently close that assuming the stress field varies linearly along the dislocation line is an acceptable approximation. We can then proceed to compute the stress tensor *at nodes only* without loss of generality. Given the stress tensor evaluated at two nodes connected by a segment (of length L), i.e. $\boldsymbol{\sigma}(\mathbf{x}_1)$ and $\boldsymbol{\sigma}(\mathbf{x}_2)$ the stress (approximated to first order) along the segment may be projected on to node 1 at $\mathbf{x}_1$ and on to node 2 at $\mathbf{x}_2$. We start by defining a local coordinate system where node 2 is at the origin and the normalized length to node 1 is (i.e. the unit length of the segment) unity. We assume not only that the stress tensor varies linearly along the segment but also that the net force on the segment may be partioned, linearly, on to each node. We define two shape functions,

$$\begin{aligned} N_2(x) &= (L-x)/L \\ N_1(x) &= x/L \end{aligned} \tag{2.10}$$

and we assume, as noted above, that the stress is distributed along the segment as

$$\boldsymbol{\sigma}(\mathbf{x}) = \boldsymbol{\sigma}(\mathbf{x}_2) + \frac{(\boldsymbol{\sigma}(\mathbf{x}_2) - \boldsymbol{\sigma}(\mathbf{x}_1))}{L} x \tag{2.11}$$

The Peach-Koehler force on each node may then be computed as

$$\begin{aligned} \mathbf{f}_1^{PK} &= \int_0^L (\boldsymbol{\sigma}(\eta) \cdot \mathbf{b} \times \mathbf{t}) N_1(\eta) \mathrm{d}\eta \\ \mathbf{f}_2^{PK} &= \int_0^L (\boldsymbol{\sigma}(\eta) \cdot \mathbf{b} \times \mathbf{t}) N_2(\eta) \mathrm{d}\eta \end{aligned} \tag{2.12}$$

for nodes 1 and 2 respectively.

2.3 Mobility

Given the scheme presented above, forces (representing the stress integrated over segments) can be directly computed on nodes. The system requires a mobility law however to evolve towards an energy minima. With the exception of particularly high strain-rate phenomena [42] inertial effects are negligible and so the concepts of both an *effective* dislocation mass and an acceleration term can be safely disregarded. A linear, viscous *over damped* mobility description is entirely appropriate however and this is readily expressed as

$$\mathbf{v}(\mathbf{t}) = \mathbf{B}(\mathbf{t})\mathbf{f}^{PK} \tag{2.13}$$

where $\mathbf{B}(\mathbf{t})$ is a linear orientation-dependent mobility function, $\mathbf{t}$ is the local line direction and $\mathbf{f}^{PK}$ is the force, computed as described above.

Because the system evolves entirely through the motion of nodes, the shape functions described in the previous section can be applied analogous to relating stresses along segments to forces on nodes, however, in this case to compute the velocity at any point along a dislocation segment as

$$\mathbf{v}(\mathbf{x}) = \sum_i \mathbf{v}_i N_i(\mathbf{x}) \tag{2.14}$$

where the sum i is over the nodes, and the shape function is non-zero *only* along segment(s) containing position $\mathbf{x}$. To compute velocities ($\mathbf{v}_i$) on each node given only the forces ($\mathbf{f}^{PK}$) it has been demonstrated [39] that solving the linear system of equations (for $\mathbf{v}_j$) given by

$$\sum_j \mathbf{B}_{ij} \cdot \mathbf{v}_j = \mathbf{f}_i^{PK} \tag{2.15}$$

where $\mathbf{B}_{ij}$ is a function of the shape functions defined earlier (i.e. $\mathbf{B}_{ij} = \mathbf{B}_{ij}(N_i, N_j)$) and the sums i, and j are over each node gives velocities on each node that are thermodynamically consistent with the rate of energy dissipation of the entire

system.

Now that we have established both a general (*viscous*, *over-damped*) mobility law as well as a self-consistent discretization scheme for this force-velocity relationship several important features of mobility that are specific to dislocations within metals are worthwhile of discussion. The first is the existence of glide planes and conservative versus nonconservative motion of dislocations. Except under conditions of extreme shear *not* acting on a glide plane dislocations are typically thought to be confined to, and glide along a pre-defined glide plane. Within DDD codes these glide planes are usually defined by a glide plane-normal vector ($\mathbf{n}$) and segments (and nodes) are fixed to their respective glide plane by a modification to the velocity vector on each node such as

$$\mathbf{v}_i \equiv \mathbf{v}_i - \mathbf{n} \cdot \mathbf{v}_i \tag{2.16}$$

where i, again, indicates a node and not an indice. Other more sophisticated schemes to incorporate non-glide effects have been proposed where the climb mobility (B_{climb}) is a small fraction of the glide mobility (B_{glide}). Schemes such as this however are still very much in a development phase and are not widely accepted.

A subtle feature which must be implemented within DDD codes for both physical as well as numerical reasons is a velocity cut-off (v_{cut}) for each node. Physically, under typical strain rate circumstances a forbidden velocity which is related to phonon interactions, and the shear wave speed of the material sets an upper-bound to the velocity [43]. Assigning an upper velocity limit consequently is an easy way to reproduce this effect within DDD models. More importantly however is the relationship between v_{cut}, δt and L_{int}, which is a maximum *local* interaction length for nearby segments (detailed in section 2.5). The detection of, and subsequent formation of junctions of nearby dislocation segments requires that segments be within a minimum distance of each other L_{int}. Simultaneously, the maximum distance that a segment can travel in a given time step is $v_{cut}\delta t$. Therefore it is necessary to ensure that two nearby segments will "*see*" each other. Otherwise the

entire junction formation process can be missed, and the simulation will continue erroneously. Therefore, when selecting v_{cut}, δt, and L_{int} as input parameters they should be chosen such that the inequality

$$v_{cut}\delta t < L_{int} \tag{2.17}$$

is obeyed. The following discussion examines δt and its potentially decreasing value throughout the simulation. Therefore the above guideline may in reality serve as an upper bound, or a starting condition for δt.

2.4 Time-Integration

The velocity on each node can vary rapidly even with respect to relatively small movements of each node. Similar to the discretization applied earlier creating nodes and segments, time requires a discretization scheme. One popular method which is both available within `ParaDiS` and is directly implemented within our DDD code is the *Euler-Trapezoid*, or otherwise referred to as the *predictor-corrector* method where two different sets of updated nodal positions are computed. For both computed *new* nodal positions a sufficiently small time step (δ t) is considered and both sets of candidate node positions are

$$\begin{aligned} \mathbf{r}_p &= \mathbf{r}_0 + \mathbf{v}(\mathbf{r}_0)\delta t \\ \mathbf{r}_c &= \mathbf{r}_0 + \frac{\mathbf{v}(\mathbf{r}_0) + \mathbf{v}(\mathbf{r}_p)}{2}\delta t \end{aligned} \tag{2.18}$$

Notice that the second set of computed nodal positions (the *corrector*, $\mathbf{r}_c$) is a function of the first (the *predictor*, $\mathbf{r}_p$). The premise of the *predictor-corrector* scheme is that the time step (δt) is sufficiently small such that the magnitude of the difference, $|\mathbf{r}_p - \mathbf{r}_c| < \epsilon$, is below some predetermined error tolerance, ϵ. If the error between the *predictor* and *corrector* is too large, i.e. $|\mathbf{r}_p - \mathbf{r}_c| \geq \epsilon$ then the time step (δt) must be sufficiently reduced to reduce the error to an acceptable

level. This is usually accomplished by decreasing the time step by a factor of 2, $\delta t \equiv \delta t/2$. The overall time-integration algorithm then can be summarized in four steps. First a nominally small time step, δt_0 is selected prior to the start of a simulation. Second, once velocities are computed on each node both the *predictor* and subsequently the *corrector* are computed using 2.18. Third, the magnitude of the error, $|\mathbf{r}_p - \mathbf{r}_c|$ is then compared to the preset error tolerance, ϵ. Fourth, if the computed error is *less than* ϵ the simulation proceeds, if otherwise the time step is reduced (nominally by a factor of two) and the candidate, updated nodal positions ($\mathbf{r}_p$ and $\mathbf{r}_c$) are re-computed.

2.5 Topological Changes

To this point, only the initial discretization has been discussed. DDD simulations however have a tendency to start with a relatively small number of straight dislocation segments and rapidly evolve in such a way that both the dislocation density, and the complexity of the network markedly increase with increased (plastic) strain. Because the computational cost of DDD simulations scales with the number of dislocation segments, but the overall resolution and accuracy of the simulation is dependent on a fine discretization, there is an unavoidable need to use the minimum amount of segments necessary to accurately capture the fields and evolution of a curved dislocation network. Due to the evolution of plasticity the necessary number of discrete segments is expected to greatly increase throughout the simulation. In order to both minimize computational expense and maximize resolution (i.e. more segments in regions of higher plastic evolution) dynamic topological changes, and multiple re-discretization steps throughout the simulation are absolutely necessary.

The simplest case, and that which we will start by examining is re-discretization, or remeshing during a simulation amongst nodes with only two neighbors or single segments which are sufficiently long. There are several reasons in even these relatively trivial situations that remeshing may be necessary. First, consider multiple

short, straight dislocation segments (as usually present during initialization of the simulation) interconnected by many nodes. When the angle made between two segments connected by a single node is π or nearly π the existence of the node itself becomes trivial, and the two collinear parallel segments could be replaced by a single, longer segment without any loss of fidelity. Conversely, a single (straight) segment cannot represent any bow-out or a curved dislocation segment. In fact the net-radius of curvature of a bow-out is limited by the maximum segment length contained within the bow-out. Furthermore, if sufficiently higher order stress gradients are acting across a single segment, the simple linear interpolation of stresses evaluated (only) at nodes and then directly projecting (integrated) forces on to these same nodes becomes a very poor approximation. Given even these two trivial examples it is clear that algorithms need to be in place to dynamically refine the dislocation network on a local level.

Considering the two scenarios presented above, the simplest approach, and an option which has been implemented within `ParaDiS` [34] is to prescribe bounds to segment lengths, a maximum length (L_{max}) and a minimum length (L_{min}). The maximum length must be such that even the smallest distance expected between pinning points (L_{pin}) throughout a simulation is greater than L_{max}. This will ensure an *unpinned* node independent of the details of the simulation and so fundamental processes such as *bow-out* will proceed physically with the addition of nodes as the single *unpinned* node begins to glide. The length L_{min} should be on the order of or less than half of L_{max} to prevent repeated creation and annihilation of node(s) on a single segment. L_{min} however should also be chosen such that it is greater than $\sim 10r_c$ where r_c is the core radius parameter. There are terms in both the energies (and forces) of the Non-Singular Theory [33] that scale as $\sim \mathcal{O}\left(\frac{r_c}{L_{min}}\right)$, and given the lack of physical significance of these terms their influence on the simulation results should be kept to a minimal. To summarize the requisite placed on the maximum (L_{max}) and minimum (L_{min}) segment lengths, $10r_c < L_{min} < L_{max}/2 < L_{pin}/2$ is required to minimize unphysical effects due to

the discreteness of the simulation.

Given the two bounds prescribed above (L_{min} and L_{max}) an additional step and algorithm is required within the simplest DDD model to enforce them. The most direct method to accomplish this is to add a remesh step immediately after *time-integration* and the computation of *new* nodal positions, but before *forces* are computed. More elegant procedures for either remeshing, or computation of forces may be employed to increase efficiency, such as non-uniform time stepping where the time step is a function of the local discreteness of the dislocation network, and far-field approximate summation techniques where a dislocation mass is "*lumped*" together to compute approximate fields and so the degree of resolution of the mesh becomes irrelevant.

The entire discussion above is limited to simple annihilation or addition of nodes and remeshing within the context of the overall DDD algorithm. The evolution of plasticity however involves the (*local*) interaction of dislocation lines both to merge and form junctions as well as annihilation of junctions. Both of these processes entail nodes with more than one (*pinned* node) or two (*free* node) adjacent segments as well as accompanying detection algorithms.

In the interest of overall clarity we will proceed to focus on the (simplest) detection algorithm next. The simplest model of possible junction detection and subsequent formation is based on a preset local interaction length, L_{int}. If two segments are detected to be at any point along each segment (d) to be separated by less than L_{int}, then a merging sequence should be initiated and the local energetics for a possible merge checked. The minimum length between two discrete segments (d) with nodes $\mathbf{r}_1$, $\mathbf{r}_2$ located on segment A and nodes $\mathbf{r}_3$, $\mathbf{r}_4$ located on segment B may be computed as follows [39]. The minimum length, d, satisfies

$$d = \sqrt{\min_{\alpha,\beta} F(\alpha,\beta)} \tag{2.19}$$

where

$$F(\alpha,\beta) \equiv ||[(1-\alpha)\mathbf{r}_1 + \alpha\mathbf{r}_2] - [(1-\beta)\mathbf{r}_3 + \beta\mathbf{r}_4]||^2 \tag{2.20}$$

the α and β which solve the minimization problem may then be solved for directly (with $\mathbf{r}_{ij} = \mathbf{r}_j - \mathbf{r}_i$) as

$$\begin{aligned} \frac{\partial F}{\partial \alpha} &\equiv \mathbf{r}_{12} \cdot \mathbf{r}_{31} + (\mathbf{r}_{12} \cdot \mathbf{r}_{12})\alpha - (\mathbf{r}_{12} \cdot \mathbf{r}_{34})\beta = 0 \\ \frac{\partial F}{\partial \beta} &\equiv \mathbf{r}_{34} \cdot \mathbf{r}_{31} + (\mathbf{r}_{34} \cdot \mathbf{r}_{12})\alpha - (\mathbf{r}_{34} \cdot \mathbf{r}_{34})\beta = 0 \end{aligned} \tag{2.21}$$

Once it has been determined that d, as described above, between any two segments, is less than L_{int} ($d < L_{int}$) it is necessary to initiate a merge procedure. The first two steps of the merge procedure are straightforward and require no additional algorithmic operations. The third step however is dependent on the local energetics of the merged configuration, and so several outcomes are possible.

For any two segments A with nodes $\mathbf{r}_1$, $\mathbf{r}_2$ and B with nodes $\mathbf{r}_3$, $\mathbf{r}_4$ and with $d < L_{int}$ the merge and junction/splitting operations proceed as follows. First, two nodes are created at the minimum distance points on each segment, for clarity an additional node **A**' is added to segment A and an additional node **B**' is added to segment B. Second, the now four segments ($\mathbf{r}_1$-**A**', **A**'-$\mathbf{r}_2$, $\mathbf{r}_3$-**B**', **B**'-$\mathbf{r}_4$) are brought together between **A**' and **B**' and a single node with four segments is created. What happens next is, as stated above, very dependent on the local energetics of the interaction, and is determined as follows.

In the third step, the rate of energy dissipation for all plausible outcomes of the previously merged **A**' and **B**' nodes are checked, and the outcome which maximizes the rate of energy dissipation is then chosen. The definition of the rate of energy dissipation [39] is

$$\dot{Q}_i = \mathbf{f}_i \cdot \mathbf{v}_i \tag{2.22}$$

where $\dot{Q}_i$ is the rate of energy dissipation on node i and $\mathbf{f}_i$ and $\mathbf{v}_i$ maintain their usual definitions from above. Given the above construction, for a single node with four segments there are seven plausible outcomes. The obvious outcome is that nothing happens, and the single node with four segments remains. This

is dependent on eq. 2.22 being the greatest with respect to the following six possibilities. Three plausible outcomes exist where the single node (with four segments) splits in to two nodes, each with three segments. The additional three plausible outcomes are that the single node splits in to two nodes, each with two segments. Various types of dislocation junctions are known to exist, and have been documented throughout the literature [38]. The six possible split-node configurations outlined here are checked for the greatest rate of energy dissipation, i.e.

$$\dot{Q}_{\mathbf{A'B'}} = \mathbf{f}_{\mathbf{A'}} \cdot \mathbf{v}_{\mathbf{A'}} + \mathbf{f}_{\mathbf{B'}} \cdot \mathbf{v}_{\mathbf{B'}} \tag{2.23}$$

Of the seven possible split configurations the split which dissipates energy the fastest is then selected and the simulation proceeds.

2.6 The Overall DDD Scheme

The five sections above provide all of the ingredients necessary for a simple DDD simulation. The purpose of this section is to assemble them and provide a simple, coherent algorithm that can be readily implemented and used for DDD problems.

Before the simulation is run, several input parameters must be chosen. The initial time step (δt), the core parameter(s) (E_{core}, r_c), the acceptable error contained within the time integration, the minimum and maximum segment lengths (L_{min}, L_{max}), and the segment interaction length (L_{int}) must all be selected such that the lengths do not violate any of the above requisites. Additionally, boundary conditions must be imposed, whether its a constant applied stress, or a constant strain rate. Finally, an initial dislocation configuration must be prescribed. This usually consists of several dislocation segments pinned by nodes.

Once the simulation has started the basic run algorithm is listed below.

1. Compute the Stress tensor (σ) on each node. Using an interpolation scheme, such as that described above, approximately integrate the stress fields along each segment and project the stress on to nodes in terms of a force. The stress should include (i) all applied fields, (ii) the interaction with all other

segments, and (iii) any "*core*" forces.

2. Assuming non-high strain rate loading, compute and solve the linear system of equations ($\mathbf{f} = \mathbf{Bv}$) governing the force-velocity relationship.

3. Apply a *Time-Integration* scheme, such as that outlined above to compute *new* nodal positions. Iterate until the *new* nodal positions are all within the prescribed error tolerance.

4. Compute the relative rates of energy dissipation for all multiply (greater than 2) connected nodes. Also compute the minimum distance between segments and compare to L_{int} for possible junction formation.

5. Apply all necessary merge and split operations. Then advance all nodes to their *new* positions.

6. *Remesh* the entire dislocation network and then repeat.

Finally, in a post-processing stage various information from the simulation can be output. Final dislocation configurations, accumulated plastic strain, the evolution of dislocation density, particular formation of junctions, etc. are all possible outputs which are interpretable within the context of macroscopic stress versus strain type data.

Chapter 3

Operation of a 3D Frank-Read Source in a Stress Gradient and Implications For Size-Dependent Plasticity

3.1 Introduction

Size effects in crystalline plasticity at the micron scale are now well established experimentally in various materials, geometries [44, 45] and loading configurations [46–51]. While the origins of these effects have been attributed to geometrically necessary dislocation hardening [52–56], dislocation starvation [57–61] and dislocation source truncation [62–68] predictive models associated with many of these mechanisms are lacking, as is an understanding of the material length scales that govern the observed size effects. As technological systems move increasingly toward smaller scales, the understanding and description of size-dependent plasticity gains increasing engineering significance.

Taking a different mechanistic view to many current theories [52], we have recently demonstrated that size effects can emerge due to stress gradients [69–71]

acting on the dislocation source-obstacle configurations that control the initiation of plastic flow. This "stress gradient plasticity" was analyzed within the context of plane strain dislocation pile-ups, and was demonstrated numerically using two-dimensional (2-D) plane strain dislocation dynamics models [69]. The plane strain derivation and demonstration do not reflect the *state-of-the-art* level of full 3-D discrete dislocation dynamics (DDD) simulations [39, 72, 73] and lack a description of the precise details responsible for the source operation in a gradient.

Here we seek to understand the role of the stress gradients on the operation of a 3-D Frank-Read (FR) source. Operation of an FR source of length l and Burgers vector b under constant shear stress τ_{app} [8] is well known: The dislocation bows-out under increasing load until an instability is reached at approximately $\tau_{FR} \equiv \tau_{app} \approx \mu b/l$, which neglects a *weak log(l)* dependence, beyond which a full loop is formed, the source is reconstituted and it begins to operate again, leading to repeated nucleation of loops. Operation of an FR source in a spatially varying stress field has not been studied directly. The structure of 2-D dislocation pile-ups in a linear stress gradient is well established [74], and these results have been used together with some approximations to estimate the back stresses acting on a 2-D FR source in a beam bending configuration [75]. However, the approximations made in Ref.[75] have not been validated and the model predictions deviate from the trends in our full 3-D simulations here. Therefore, in this chapter, we use 3-D discrete dislocation simulations to study the operation of a real FR source in a stress gradient. In a linearly varying stress field, we show that the source operation changes fundamentally, with the dislocation unable to cross the "neutral axis" or position of zero stress, preventing pinch-off on the lower-stress side of the pinned FR source. The emitted loop pinned at the neutral axis then exerts a back stress on the reformed source and inhibits further operation. Increasing the stress leads to the eventual operation of the source, but each emitted loop joins a pile-up around the neutral axis. The simulations reveal a new set of metastable states and an associated strengthening of the source as a function of the stress gradient and of

the number of previously nucleated dislocation loops. We present and validate a simple 2-D analytic model that captures key features of the operation of an FR source operation in the presence of a stress gradient. We then apply both the simulation results and the analytic model to rationalize some experimental and numerical results on the size dependence of plasticity in the bending of single-crystal beams.

3.2 Methodology

The 3-D DDD code `ParaDiS` [34, 39] was used to conduct the simulations. `ParaDiS` allows for the implementation of arbitrary dislocation configurations with prescribed material properties, boundary conditions, and loading conditions. The initial configuration of an FR source is shown in Fig. 3.1a: a single straight edge dislocation segment along the y axis is pinned at its two ends and is centered at x = y = z = 0 within a large cubic simulation box for which image forces are verified to be negligible. The prescribed boundary conditions are periodic along the faces normal to y and traction free along the faces normal to x and z. Four initial source lengths are analyzed, l = 250b, 500b, 1000b and 2000b. While the results are essentially independent of physical material properties, values are needed in the code and we use a shear modulus μ = 130 GPa, a Poissons ratio ν = 0.305 and b = 2.725 Å. A simple face-centered cubic mobility slip law is used, where slip is only permitted on the z = 0 (001) plane containing the source, with no cross-slip and a maximum dislocation segment velocity of 5e7b/s. A dislocation core cut-off radius (within `ParaDiS`) of r_c = 2b was selected such that an FR source in a constant stress field operates at approximately $\tau_{FR} = \mu b/l$ over all lengths investigated here. `ParaDiS` adaptively discretizes the dislocation segment as the simulation evolves, with a maximum segment length of $l/2$. A spatially varying shear stress

$$\tau_{xz} = \tau_0(1 - \chi x) \tag{3.1}$$

is imposed, where τ_0 is the magnitude of the stress at the initial source location and χl is a normalized measure of the stress gradient: $\chi = (\frac{-1}{\tau_0})(\frac{d\tau_{xz}}{dx})$. The distance $1/\chi$ is then also the distance from the source to the plane at which the applied stress becomes zero (the neutral axis or neutral plane), and we use a simulation box length of size $4/\chi$. The evolution of the dislocations is examined for increasing values of the *applied* stress τ_0, for a range of dimensionless gradient values $0.2 \leq \chi l \leq 1$.

The simulations proceed as follows. The stress τ_0 is incremented, inducing dislocation glide. During glide, the cumulative average velocity of every node is recorded. Once (i) at least 400 time steps have passed, (ii) the ratio of the change in the cumulative average velocity of each node to the cumulative average velocity of each node is less than 0.1% for 300 steps and (iii) the maximum node velocity is less than 5e7b/s, the stress is incremented again, by 0.5% of the current value. During glide, two types of segment collisions can occur. First, the dislocation can reach the periodic boundaries of the simulation cell and react with itself to form two separate dislocations, one that glides out of the simulation space at $x << 0$ and the other that glides toward $x = 1/\chi$. Second, dislocation segments on the two sides of the latter dislocation can meet and annihilate, forming a new FR source and a separated dislocation. The stress at which the latter event occurs is recorded as the operating stress for the source. Fluctuations present within the data are attributable to numerical issues resolving the equilibrium position of all nodes. As the simulation proceeds with continued operation of the source, we obtain the FR source strength τ_0 as a function of the number of nucleated dislocations (N-1) and the dimensionless stress gradient χl, e.g.

$$\tau_0 = \tau_0(N, \chi l) \tag{3.2}$$

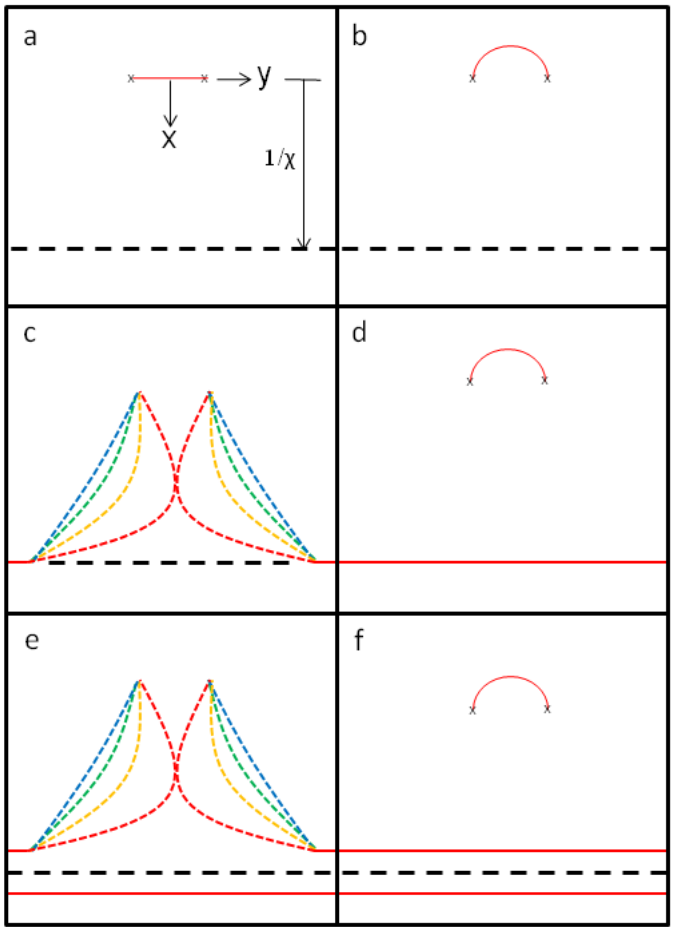

Figure 3.1: Evolution of an FR source operating in an applied stress gradient: (a) initial configuration under no applied stress; (b) first critical configuration, qualitatively similar to that found under zero stress gradient; (c) sequence of stable configurations under increasing applied load for larger stress gradients, culminating in pinch off; (d) second nucleated loop at first critical condition (as in (b)), in the presence of the first nucleated dislocation that sits at distance $1/\chi$; (e) sequence of stable configurations under further increasing load culminating in pinch off; and (f) third nucleated loop in the presence of the prior two nucleated dislocations at positions around $1/\chi$.

3.3 Results and Analysis

Figure 3.1 shows a sequence of dislocation configurations under increasing load in the presence of a high stress gradient. The source first bows out into the increasing stress region (x $<$ 0), and becomes unstable (Figure 3.1b.), similar to a Frank-Read source in a constant stress field but at a lower applied stress $\tau_0 < \tau_{FR}$ because the local stress fields on the dislocation segments are larger than τ_0 in the x $<$ 0 region. However, as the dislocation expands and loops around into the region x $>$ 0, the

decreasing stress field inhibits further glide. The loop can expand in x < 0 and laterally along y < 0 and y < 0, annihilating along the periodic boundaries and creating a dislocation in the region x < 0 that moves off towards x $= -\infty$. The remaining dislocation remains trapped in the region x > 0 and is unable to pinch-off and reconstitute the source. Trapping and inhibition of the pinch-off are the key features of the Frank-Read operation in a graded stress field. With increasing applied stress (Figure. 3.1c), the first dislocation bows increasingly inward and eventually reaches pinch-off, but the new nucleated dislocation rapidly becomes straight and glides to x $= 1/\chi$, where $\tau_{xz} = 0$. The reconstituted FR source then starts to act again (Figure. 3.1d), but when this second dislocation enters the x > 0 region there is a back stress due to the first dislocation that impedes the glide and further inhibits pinning (Figure. 3.1e). The first dislocation does move into the region where $\tau_{xz} < 0$ due to the forces exerted by the second dislocation, but the overall interactions inhibit pinch-off. With further increased load, pinch-off is achieved, a two-dislocation pile-up is formed (Figure. 3.1f) centered around x=$1/\chi$, and the source begins to operate again. But, pinch-off of the next emitted dislocation is further inhibited by the back stresses from the two-dislocation pile-up. This evolution continues, with increasing applied stress needed to pinch-off each subsequent dislocation and an increasing dislocation pile-up around x $= 1/\chi$.

The applied stress required to nucleate successive dislocations from the Frank-Read source in the presence of a stress gradient, i.e. to achieve pinch-off and reconstitute the Frank-Read source, is shown in Figure 3.2. The source strength is normalized by the standard Frank-Read strength (τ_{FR}) and is shown as a function of the number of emitted dislocations for a range of normalized stress gradient values χl.

For the initial source operation (N = 1) there is a slight weakening effect ($\tau_0 < \tau_{FR}$) for low gradients ($\chi l < 0.4$). In this domain, the region of higher stress (x $<$ 0) drives the initial loop instability and the lower stresses in x > 0 are insufficient to inhibit pinch-off. However, for larger gradients ($\chi l \geq 0.4$), a strengthening

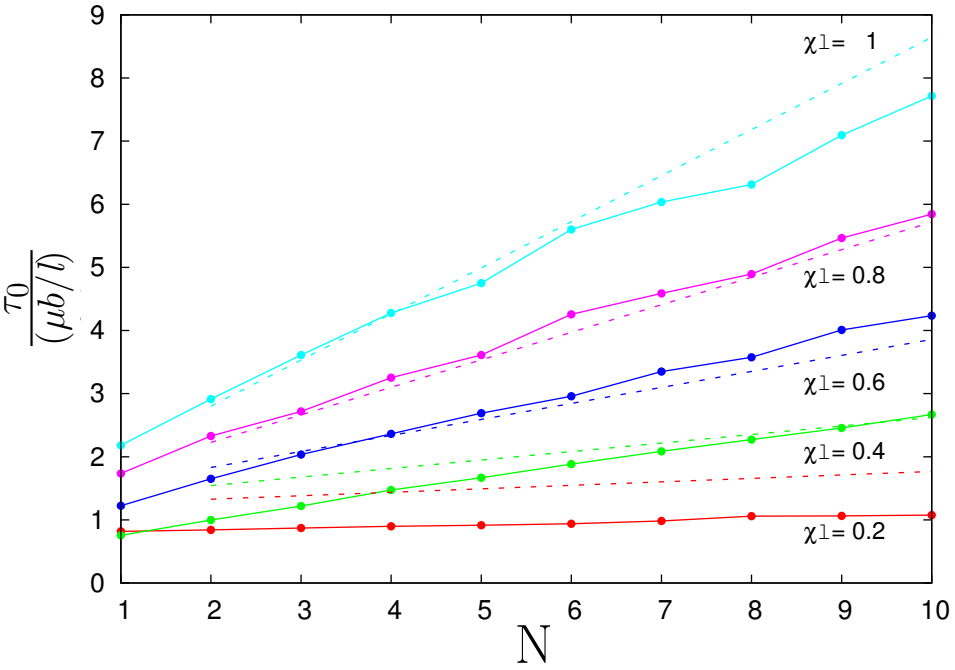

Figure 3.2: Normalized FR source strength $\left(\frac{\tau_0}{\mu b/l}\right)$ versus number (N) of dislocations emitted from the source, for various values of the normalized gradient χl. Solid line: DDD simulation data; dashed line: analytical model of 3.8. Results here use l=250b, τ_c=1.16τ_{FR} and x_c=0.44l in 3.8; similar results are obtained for other values of l.

effect is observed due to the inhibition of pinch-off (Figure. 3.1c), a new feature that is unique to the stress gradient problem. In this strengthening regime, the strengthening scales approximately linearly with χl. We can estimate the pinch-off stress for the first dislocation by approximating the interactions between the two arc-like segments. We equate the self-force of a bowing arc segment to the sum of the attractive force between two opposite signed screws (treated as straight, and of length $1/\chi$) and the integrated applied force. The result qualitatively captures the linear strengthening with respect to χl observed in the simulations (N = 1) but is quantitatively quite poor. To make any quantitative comparison requires a priori knowledge of the exact length, orientation and shape of the two arc-like segments, which rapidly becomes unwieldy and approaches execution of precisely what is computed in the `ParaDiS` simulations.

Figure 3.2. shows that, after the first dislocation (N = 1) is emitted, operation of the source to emit additional dislocations (N > 1) requires an increasing applied

stress at any normalized gradient χl. Even at the smallest gradient values studied here ($\chi l = 0.2$) there is some strengthening effect due to the gradient field after several dislocations (N = 4) are emitted. Overall, the magnitude of the strengthening is significant e.g. twice the nominal source strength τ_{FR} can be achieved for moderate gradients ($\chi l = 0.4$) and moderate numbers of dislocations (N = 7) emitted. Overall, Figure. 3.2 demonstrates a clear effect of a spatial stress gradient on the operation of a full 3D Frank-Read source and is the first main result of this chapter.

We can understand and unify the simulation results shown in Figure 3.2 for N>1 through a model that considers the back stresses due to the previously emitted dislocations. First, we ignore the two curved segments of the current dislocation that has not yet pinched off, and treat it as a long straight edge dislocation. The positions of the prior N-1 dislocations and this last dislocation are then the equilibrium positions of an N-dislocation pile-up in a linear gradient field, a problem solved by Eshelby and Bilby [74] and shown schematically in the inset of Figure 3.3. The Peach-Koehler force on each edge dislocation in a stress field of the form $\tau = -\tau_0 \chi x$ is satisfied by [74].

$$H_N^{''} - 2\tau_0 \chi x H_N^{'} + 2N\chi H_N = 0 \tag{3.3}$$

where H_N is the N^{th} Hermite polynomial, and the equilibrium positions x_i, where i = 1, , N are associated with the roots of H_N, e.g.

$$0 = H_N \left(\frac{\tau_0^{1/2} \chi^{1/2} x (2\pi(1-\nu))^{1/2}}{\mu^{1/2} b^{1/2}} \right) \tag{3.4}$$

The solutions of 3.4 are in excellent agreement with our discrete simulations over the entire range of parameters studied, with the trivial difference that our coordinate system is shifted relative to that of Eshelby and Bilby by $1/\chi$. For instance, figure 3.3 shows the normalized position of the N^{th} dislocation, x_N/l, as a function of the normalized gradient χl, for several values of N, as measured in our

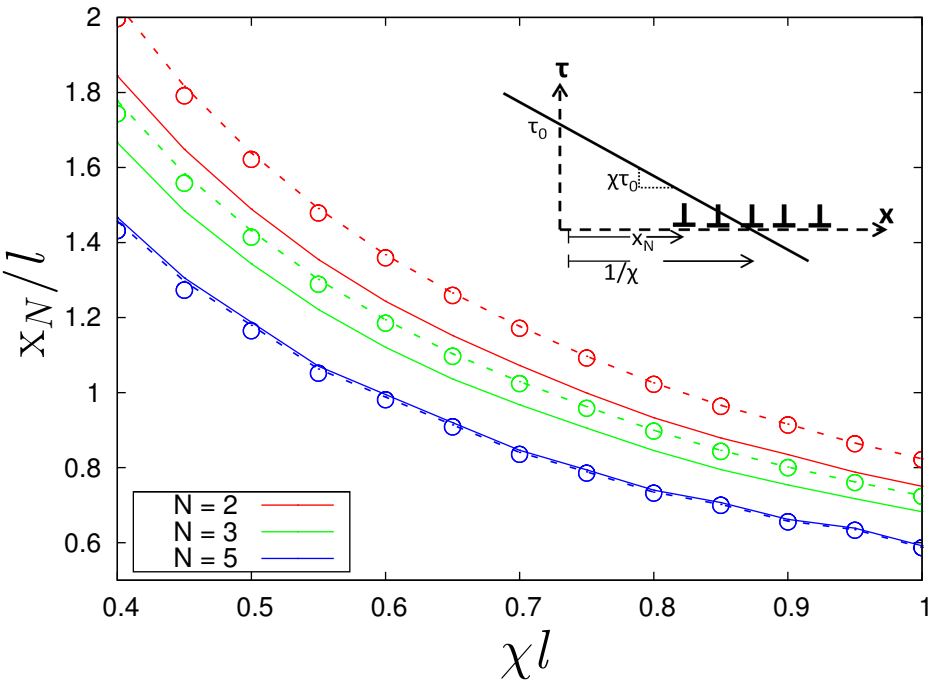

Figure 3.3: Normalized distance (x_N/l) from the source to the last (N^{th}) dislocation versus normalized stress gradient (χl) as measured in simulations (circles), as predicted by the Hermite polynomial solution of 3.4 (dashed) and as predicted using the superdislocation approximation of 3.7 (solid). Inset: schematic of the N-dislocation pile-up in the linear stress gradient.

simulations and as predicted by 3.4. Now, given the positions x_i of the i = 1, , N dislocations, the total resolved shear stress at a point x due to the first N-1 dislocations is

$$\tau(x) = \tau_0(1 - \chi x) - \frac{\mu b}{2\pi(1-\nu)} \sum_{j=1}^{N-1} \frac{1}{x_j - x} \tag{3.5}$$

This stress field operates on the N^{th} dislocation, influencing its pinch-off and reconstitution of the Frank-Read source for the next emission. Qualitatively, the prior N-1 edge dislocations emitted from the source symmetrically pile-up around $x = 1/\chi$ and produce a back stress on the N^{th} dislocation connected to the source, pushing the long, straight segments back toward the source and thus decreasing the ability of the two arc-like segments to bow-out (Figure 3.1e), thereby inhibiting their intersection and reconstitution of the Frank-Read source.

Equation 3.5 requires the solution of 3.4, which must be done numerically.

To obtain a very useful analytical approximation, we first note that half of the dislocations are at distances $x > 1/\chi$ and half at $x < 1/\chi$ (when N is odd, one dislocation sits exactly at $x = 1/\chi$). Therefore, we group the initial N-1 dislocations into a single super-dislocation located at $x = 1/\chi$ and approximate 3.5 as

$$\tau(x) = \tau_0(1 - \chi x) - \frac{\mu b \chi (N-1)}{2\pi(1-\nu)(1-\chi x)} \tag{3.6}$$

The position x_N of the N^{th} dislocation satisfies $\tau(x_N) = 0$ and is given by

$$x_N = \frac{1}{\chi} - \left(\frac{\mu b}{2\pi(1-\nu)}\right)^{1/2} \left(\frac{N-1}{\tau_0 \chi}\right)^{1/2} \tag{3.7}$$

The predictions of 3.7 are compared to our simulation data in figure 3.3 for several of the initially emitted dislocations following the initial pinch-off. The error in using the super-dislocation approach is consistently $\sim 0.1l$ for N=2, $\sim 0.05l$ for N=3 and negligible for higher N. We thus proceed to use the super-dislocation approximation below.

Next, we postulate that pinch-off of the two arcs of the N^{th} dislocation (see Figure 3.1c) is determined by the attainment of some critical stress τ_c at some critical location x_c, both to be determined, independent of any other details of the configuration (e.g. independent of the magnitude of the gradient, the applied stress or the number of previously emitted dislocations). To test this postulate, we plot the normalized stress field $\tau(x)$ versus x computed via 3.6 for every value

Normalized Source Length (l/b)	250	500	1000	2000	All Source Lengths
x_c/l	0.44	0.45	0.47	0.49	0.48
τ_c/τ_{FR}	1.16	1.45	1.43	1.55	1.33
Average Error (%)	6.75	9.29	4.94	6.76	10.72

Table 3.1: Normalized critical position x_c/l and critical stress τ_c/τ_{FR} for operation of a 3-D FR source in the presence of a gradient and induced dislocation pile-up, for various FR source lengths. Average error in this effective point source condition for τ_c/τ_{FR} is generally less than 10%.

of (τ_0, , N) (N>1) at which source operation is observed in the simulations (i.e. the data of Figure 3.3). We then search for a unique point (x_c, τ_c) through which all these stress fields pass. The result is shown in Figure 3.4 for one case ($l = 250b$). Although the stress fields do not all pass through exactly one point, there is a remarkable convergence of the stress fields in the vicinity of $x/l = 0.44$ and $\tau/\tau_{FR} = 1.16$. Similar results are obtained for the other source sizes, as shown in Table 3.1. The standard deviation in the critical stress at the critical location is on the order of 7% across all source sizes, and most of the error comes from the cases with N=2 and where source operation is controlled by the initial instability rather than the second pinch-off instability; such cases are outside the scope of our model. There is a slight dependence of the optimal values of x_c and τ_c on the value of l but the dependence is weak for $l/b \geq 500$. Using the critical stress τ_c at the critical location x_c, we can thus express the strength τ_0 of the Frank-Read source in the presence of a gradient field including the effects of all prior source emissions as

$$\tau_0(\chi, N) = \frac{\tau_c}{1 - \chi x_c} + \frac{\mu b \chi (N-1)}{2\pi(1-\nu)(1-\chi x_c)^2} \tag{3.8}$$

for N > 1. The predictions of 3.8 are shown in Figure 3.2. The model captures the initial strengthening and subsequent hardening associated with the inhibited Frank-Read source operation in the stress gradient. The model is based on the existence of a new stable configuration for the Frank-Read source, so is quite accurate in the regime controlled by that stable configuration, i.e. $\chi l \geq 0.4$ and $N \geq 2$. The model is not accurate for low normalized gradients ($\chi l = 0.2$), where the 3D Frank-Read source operation is controlled by the high-stress region $x < 0$, a regime outside the scope of this model. The demonstration that operation of a 3D Frank-Read source in the presence of a stress gradient can be accurately represented by a (nearly) unique critical stress τ_c at a critical position x_c, with an accurate analytic model for the source strength (3.8), is the second main result of this chapter.

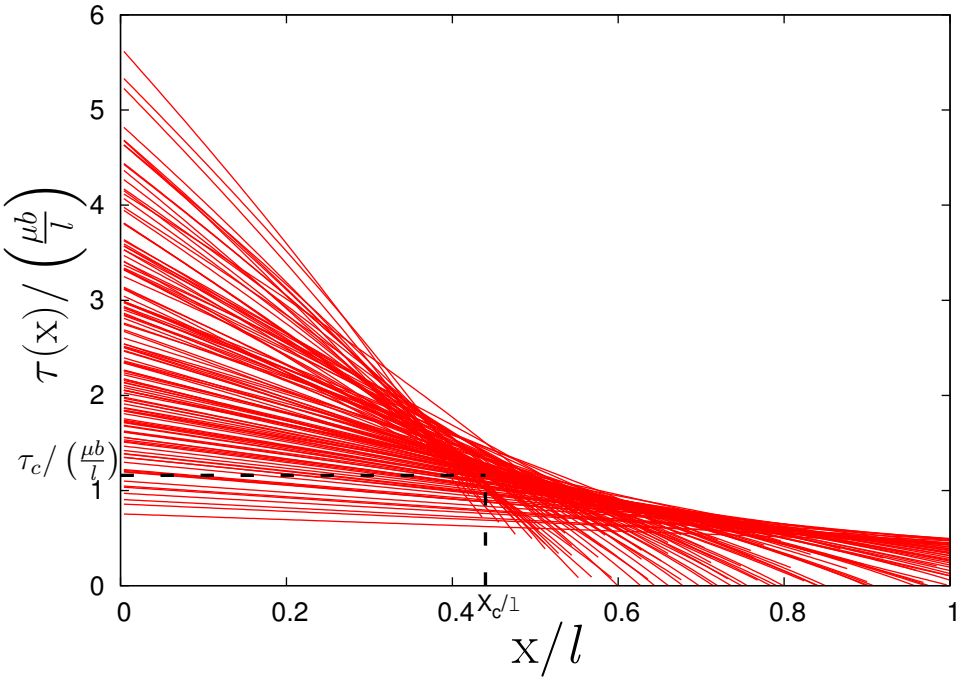

Figure 3.4: Normalized stress field $\tau(x)$ versus position x, evaluated at all operating source strengths measured in the simulations (l=250b, χ $l\geq$0.4, N$\geq$2). All stress fields nearly pass through a single critical operating stress τ_c at a critical distance x_c from the source, as indicated. Similar results are obtained for other values of l.

3.4 Applications

3.4.1 Comparison to 3-D DDD Simulations

Motz et al. [75] performed full-sample 3-D DDD simulations of pure bending of micron-scale beams containing an initial distribution of FR sources, and measured size-dependent strengthening and hardening. Here, we show that the full 3-D DDD simulations can be accurately interpreted simply through consideration of the operation of a single FR source in the stress gradient created by the bending deformation.

The Motz et al. simulations were nominally for a single-crystal Al beam, with the bending moment about the (0 0 1) plane and the tensile direction along [0 1 0]. Four {1 1 1}<1 1 0>-type slip directions are active, and intersect the neutral plane of the beam with Schmid factors of 0.408. Motz et al. [75] report the flow stress M/(Bt2) as a function of the normalized total displacement along the

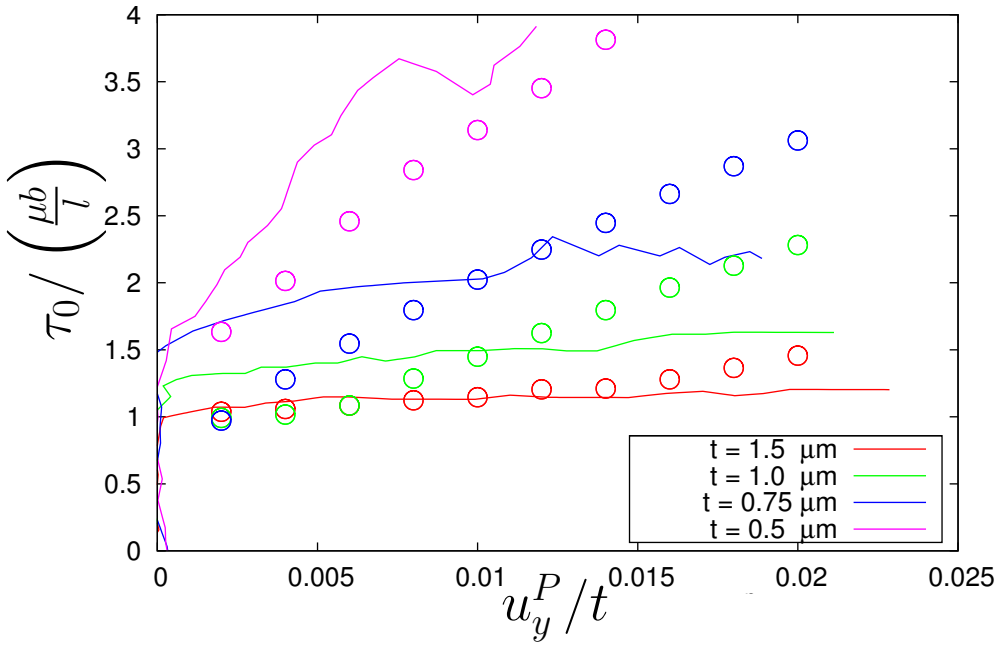

Figure 3.5: Normalized flow stress versus normalized plastic displacement, as obtained in the full 3-D DDD simulations of Motz et al. [75] (solid) and as derived from the present simulations on a single FR source operating in the stress gradient defined by the beam bending (circles).

length of the beam u_y/t for beam thicknesses t = 0.5, 0.75, 1.0 and 1.5 μm. In pure bending, plastic flow initiates on the outer surfaces of the specimen where the local tensile stresses are highest. The relationship between the tensile stress on the surface and the measured bending moment is $\sigma_0 = 6M/(Bt^2)$, where B and t correspond to the breadth and thickness of the beam, respectively. The resolved shear stress driving plastic flow is thus related to tensile stress on the surface as $\tau_0 = 2.45M/(Bt^2)$.

Our simulations and model predict the flow stress for a single FR source as a function of the number of previously emitted dislocations N. To connect to the Motz data we must thus relate dislocation emission to plastic displacement as follows. Each dislocation emitted from an FR source near the surface will produce an edge dislocation that glides a distance $1/\chi = t/\sqrt{2}$ along the glide plane to, on average, the neutral plane of the beam, thereby contributing a total plastic displacement $\mathbf{u}_p = \mathbf{b}/2$ with components $u_x^p = u_y^p = b\sqrt{2}/4$. After N dislocations have been emitted from each active source and for a density of active sources

ρ in a beam of length L (total number of active sources ρL), the normalized plastic displacement along the length direction is then $u_y^p/t = \sqrt{2}N\rho Lb/4t$. Our simulations thus yield a flow stress versus normalized plastic displacement given a density of active sources along the beam.

We can now make a comparison to the results of Motz et al. [75]. Motz et al. use beams with L/t fixed at 3. For such sample dimensions, the normalized plastic displacement along the length is $u_y^p/t = 3\sqrt{2}N\rho b/4$. The density of active sources in the Motz simulations is not known, however. A posteriori, dislocation pile-ups are clearly observed along the length of the beams, though no quantitative results are available. We therefore fitted the quantity ρ to relate our results, based on single-source operation, to the net total response of multiple sources in the Motz model. Motz et al. present the total displacement and so the elastic displacement of the beam is subtracted from that data. Since the plastic displacement depends on the product Nρ, and since our simulations and the Motz et al. data both show nearly linear hardening, our model can be reasonably fitted to the Motz et al. data for any combination satisfying Nρb $\sim$ 0.0189. However, the Motz et al. data shows relatively smooth, continuous evolution of the plastic displacement and clear multi-dislocation pile-ups, so N cannot be too small (i.e. a few dislocations emitted from a large number of sources). Figure 3.5 shows the normalized flow stress τ_0/τ_{FR} versus normalized plastic displacement u_y^p/t as predicted by our model, with $1/\rho$ = 152 nm and N=10, and as obtained in the Motz et al. simulations. Our simulations generally agree well with the Motz et al. data at both small and large beam thicknesses (large and small stress gradients, respectively). At the intermediate thicknesses, stress gradient effects do not set in until a few dislocations have been emitted, so our predictions are only in qualitative agreement with the full simulations of Motz et al. [75]. The general ability of the mechanics of a single FR source operating in a stress gradient to capture the full 3-D DDD bending response of a beam is the third main result of this chapter.

Application of our analytic model yields results comparable to those shown in

Figure 3.2. The model agrees with our simulations and the Motz et al. [75] data at the smallest beam size (highest gradient). At the largest beam size (smallest gradient), the analytic model predicts no hardening but has a higher initial flow stress, since $\tau_c = 1.33\tau_{FR}$ is the smallest possible value in the analytic model. At intermediate beam sizes, corresponding to moderate stress gradients, the analytic model overestimates our simulations at low N, where the analytic model has already been shown to be less accurate.

3.4.2 Comparison to Experiments

In separate work, Motz et al. [50] conducted experiments on the bending of single-crystal Cu microbeams ranging in thickness from 1 to 7.5 μm and oriented with the bending moment about the $(\bar{1}\bar{1}2)$ plane and the tensile direction along $[1\bar{1}0]$. During loading, the force versus end displacement of the beam was recorded and beyond a critical displacement the force reached a plateau. Motz et al. proposed that, due to strain hardening, the best measure of the flow stress is to assume an even distribution of plastic flow through the thickness of the beam, identical to a plastic hinge. Using equilibrium of moments, the average flow stress is related to the force by $\sigma_f = 4\mathrm{M}/(\mathrm{Bt2})$ where $\mathrm{M} = \mathrm{F}_{max}\mathrm{L}$ is the moment. The flow stress computed in this manner scaled nearly inversely with beam thickness, following the power law fit $\sigma_f = 140$ MPa + 881 MPa-$\mu\mathrm{m}^{1.14}\mathrm{t}^{1.14}$. In our model, we assume that the onset of plastic flow occurs along the outermost surface of the beam so that σ_0=6M/(Bt2). This flow stress can thus be computed from the quoted stress of Motz et al. as $\sigma_0 = 3\sigma_f/2$. With a Schmid factor of 0.408 for slip along any of the four {1 1 1}<1 1 0> active slip directions, the average flow stress leads to a critical resolved shear stress τ_0=86 MPa + 539 MPa-$\mu\mathrm{m}^{1.14}\mathrm{t}^{1.14}$ along the outer surface of the beam. Interpreting the experiments within the context of our model, we first assume that the measured critical resolved shear stress of 86 MPa at large beam thicknesses is controlled by FR sources of this strength, i.e. 86 MPa=$\mu\mathrm{b}/l$. We can then calculate the active source length $l = 517$b using the shear modulus

along the slip direction of μ_{110} = 44.3 GPa for Cu [76]. Manipulation of the experimental data [50] yields the normalized scaling

$$\frac{\tau_0 - \tau_{FR}}{\tau_{FR}} = \frac{\Delta\tau}{\tau_{FR}} = 63.1 \left(\frac{t}{l}\right)^{-1.14} \tag{3.9}$$

as shown in figure 3.6 using the right axis. In these experiments, yielding and subsequent plastic flow initiates where the cantilever beam is integrated into the supporting structure. With further displacement, the region of active plastic flow evolves towards the free end of the beam, manifested in a sequence of visible slip bands. We thus interpret the plateau observed in the measured force as the critical force required to initiate the formation and hardening of successive slip bands down the length of the beam. This interpretation is supported by finite element computations on this geometry using conventional size-independent plasticity models. The flow stress derived from analysis of the experimental data should thus correspond approximately to the stress required to form and strengthen/harden an individual slip band.

Turning to predictions of our model, dislocations glide along the slip plane to the neutral axis and this geometry dictates that the normalized (shear) stress gradient is χ=1.71/t. The change in plastic displacement in the direction of flow due to the prior N 1 dislocations is u^p = (N 1)b/2. We can thus take all of our simulation data, subtract the initial strength $\tau_0(\chi l; N = 1)$ and normalize by both the FR strength (similar to above) and the normalized plastic displacement u^p/b, to obtain a normalized scaling

$$\frac{\tau_0(\chi l; N) - \tau_0(\chi l; N = 1)}{\tau_{FR}\left(\frac{u^p}{b}\right)} \sim 2.5 \left(\frac{t}{l}\right)^{-1.16} \tag{3.10}$$

as shown in figure 3.6 using the left axis. This comparison demonstrates the unique size scaling of the hardening found both in our simulations (at any fixed plastic displacement) and in the experiments. Note that, while 3.9 and 3.10 show similar size scaling of the hardening, they differ in that eq. 3.10 is also normalized by the

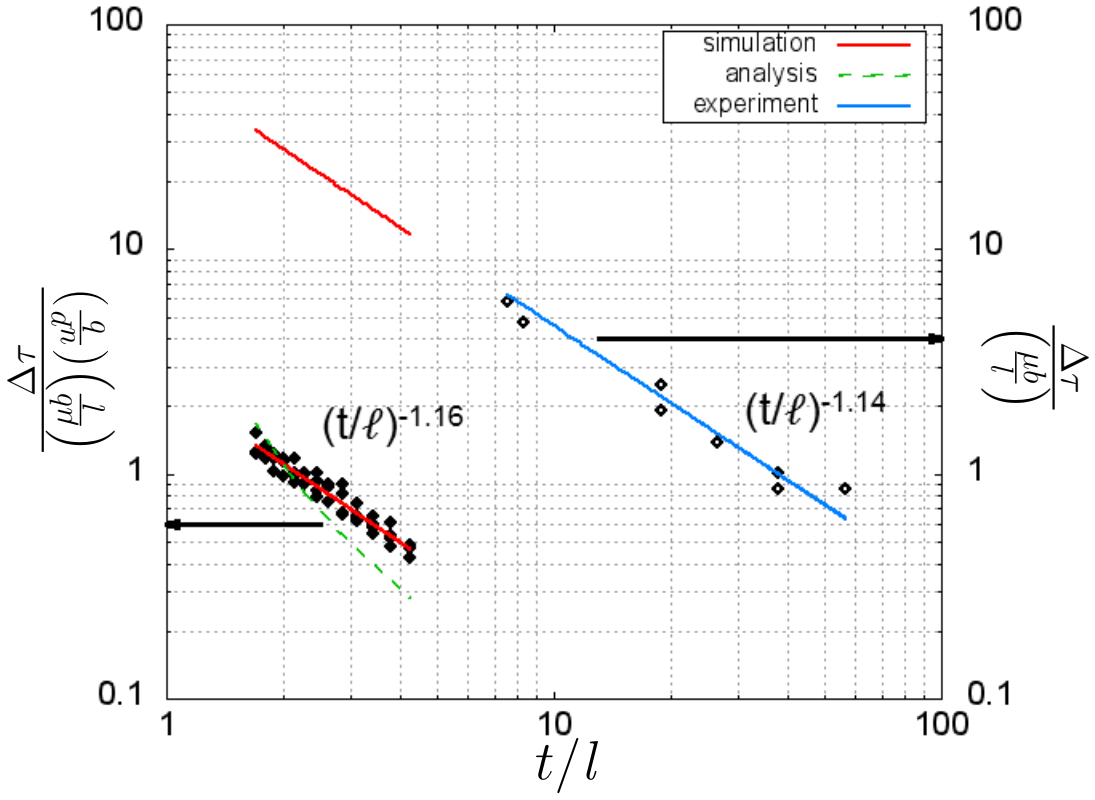

Figure 3.6: Left axis: normalized change in flow stress versus normalized beam thickness, independent of plastic displacement, from simulations (solid squares) and the analytic model of 3.8 (dashed line); right axis: normalized change in flow stress versus beam thickness from experiments [50] (open squares), from simulations (solid line) and from the analytic model (dashed line) assuming NρL = 25.2 (see text).

plastic displacement, leading to the use of different axes in figure 3.6. The analytic model of 3.8 can be manipulated similarly to our simulation data, yielding

$$\frac{\tau_0(\chi l; N) - \tau_0(\chi l; N=1)}{\tau_{FR}\left(\frac{u^p}{b}\right)} = \frac{1.71(t/l)^{-1}}{\pi(1-\nu)\left(1-0.82\left(\frac{t}{l}\right)^{-1}\right)^2} \tag{3.11}$$

where we have substituted the value $x_c/l = 0.48$ derived from our analysis. 3.11 is also shown in figure 3.6, using the left axis. Although 3.11 shows an asymptotic scaling of $(t/l)^1$ in reasonable agreement with the simulations and experiments, the actual values in the simulated range of t/l show a slightly stronger size scaling. In 3.11 we are analyzing the size scaling of the hardening rate (hardening versus plastic strain), and the analytical model predictions of the slope are not as accurate as the overall trends with χl. A quantitative comparison between our results

(3.10 and 3.11) and the experiments of Motz et al. (i.e. to connect the right and left scales in figure 3.6) requires additional information on the total plastic displacement. Equating our result of 3.10 to the data of Motz et al. as expressed in 3.9 requires a plastic displacement per source of $u_p/b = 63.1/2.5 = 25.2$. The prediction of 3.10 with $u_p/b = 25.2$ is shown in figure 3.6 now using the same (right) axis as used for the experiments.

A local plastic displacement of $u_p/b = 25.2$ corresponds to $N \sim 2u_p/b \sim 50$ dislocations emitted per source, which would produce surface steps of magnitude $50b \sim 13$ nm. Shielding of other potential sources by these pile-ups would lead to a slip plane spacing that scales as $\sim t/2$ (the glide distance from source to neutral axis). In the scanning electron micrographs, however, larger displacements and smaller spacing are observed. If the beam rotation of 4° over a length of 20 μm, as shown in the micrograph in figure 2a of [75], is assumed to be accommodated exclusively by plastic displacement on one of the two active slip systems in all of the ∼20 observed slip bands on each side of the specimen, then the step size Nb per slip band can be estimated as $20Nb \sim (20\ \mu m)\tan(4°)$ or $Nb \sim 70$ nm, which is more comparable to the observed step sizes. However, the back stresses associated with the associated $N = 275$ in an individual slip band would give a strengthening effect approximately $275/50 = 5.5$ times higher than observed in the experiments. In general, this comparison indicates that, in the experiments, any FR sources behave like conventional FR sources but operate in the presence of the back stress field created by the pile-up of previously emitted dislocations around the neutral plane of the specimen. The hardening behavior is thus attributable to the stress gradient present in the bending problem, but does not reflect a stress gradient effect on the source operation itself in this regime of very large t/l. Overall, our results for operation of a single FR source in a stress gradient can match the size scaling of the strengthening observed in the experiments, which is the fourth main result of this chapter. In spite of this success, quantitative predictions remain difficult and undoubtedly the experimental situation is more complicated than

envisioned in our basic analysis.

3.5 Summary

The model presented here demonstrates the strengthening and hardening effects arising when a Frank-Read dislocation source operates in a graded stress field. This behavior arises due to the emergence of a new metastable configuration for the Frank-Read source, as demonstrated via 3D-DDD simulations, and for which the length of the Frank-Read source is the physical material length scale controlling the magnitude of the gradient effect. The operation of a Frank-Read source in a stress gradient, including pile-up dislocations formed on the low-stress side of the source, can be captured through an effective Frank-Read source strength associated with the attainment of a critical stress at a critical location near the Frank-Read source. To make connections to full 3D-DDD simulations and experiments requires knowledge of dislocation source densities. Using values estimated from the numerical studies [75, 77], we are able to capture key features of the strengthening and hardening size effects measured in the full 3D-DDD simulations. Our analysis also predicts the scaling of experimentally measured strength versus size in bending of cantilever beams, although quantification remains difficult, suggesting that other factors may enter. These results are achieved without consideration of either dislocation junction formation or *strain gradient plasticity*. While the dislocation pile-ups that form in beam bending do correspond to plastic strain gradients, the *stress gradient plasticity* analysis here is a more physically motivated description of that pile-up phenomenon and has a well-defined material length scale controlling the size-scaling behavior. However, this does not mean that other strain-gradient phenomena are unimportant; rather, our results indicate that the influence of stress gradients should also be considered in understanding size effects in plasticity.

Chapter 4

Analysis of Spurious Image Forces in Atomistic Simulations of Dislocations

4.1 Introduction

Fully atomistic methods have become an indispensible tool for providing direct physical insight into the mechanistic role of defects in materials [14–16, 20, 23, 78]. Molecular statics simulations have been used extensively to study grain boundaries [32, 79, 80], dislocation cross-slip [29, 81, 82], crack tips [83, 84], and dislocation/obstacle interactions [14–20, 22, 23, 85–99]. Due to the high computational cost, the size of simulation volumes (i.e. number of atoms) remains relatively small. For problems involving dislocations, which have long range stress and strain fields, the image forces associated with spurious interactions between dislocations and boundaries of the simulation cell can be non-negligible, but have also been difficult to assess quantitatively. Nonetheless, various proposed methods to simulate dislocations [17–19, 22, 90] have proven useful in providing insight into plasticity phenomena. As computational materials science heads toward the goal of quantitative predictive results relevant to real materials, the issue of accuracy

of the methods becomes more important. While one solution is to increase the simulation cell size, which is becoming more feasible as computational capabilities continue to expand, the need to perform many such simulations makes this only a partial solution. Thus, a quantitative understanding of spurious image interactions in standard MD simulations of dislocations is a useful benchmark for designing and interpreting simulation results. A variety of numerical methods have been developed to incorporate image forces based on finite element computations [100], and fourier-transform methods [101, 102] as well as exact analytic expressions for simple geometries [74, 103]. Here, we pursue a similar goal using other approaches and aimed at quantifying image forces within the standard simulation geometries used for simulating problems involving dislocation bow-out.

Since its inception [104] the Periodic Array of Dislocations (PAD) method [17–19, 105] has emerged, and gained acceptance over the past decade, as a means to model interactions between dislocations and other inhomogeneities. In this method, a single Volterra dislocation is inserted along the x axis with its glide plane normal to the z axis as shown in Fig. 4.1a. The simulation volume V = L_x $\times$ L_y $\times$ L_z has periodicity imposed both along the line (x) and glide directions (y), creating a periodic array of dislocations. Accomplishing periodicity along the glide direction for edge dislocations requires addition or removal of atoms, but various methods to do so are described in the literature [18, 23]. The remaining out-of-plane direction is non-periodic, allowing for the application of stress [22] (or strain [18]). The initial singular dislocation structure is then relaxed using, e.g., the conjugate gradient method. The addition of solutes, precipitates, vacancies, or "*quench methods*"[106, 107] are then used to create obstacles to dislocation motion with the desired physical characteristics for the problem of interest. To apply a stress to the system using traction boundary conditions, the out-of-plane surfaces are subject to in-plane tractions by application of appropriate forces to atoms. For instance, to drive an edge dislocation using a traction boundary condition, the applied shear stress is $\tau_{yz} = F_y/A$ where F_y/N represents the average force on

each of the N atoms acting over the upper or lower surface respectively (surface normal z) of area $A = L_x L_y$. Applied stresses can also be controlled by specifying displacement boundary conditions, i.e. fixing atoms on upper and lower surfaces, to generate the desired "applied" stress state in the interior of the system. Mixed boundary conditions (e.g. normal displacements and in-plane tractions) may also be used [23]. The defect-containing volume is then studied under varying applied loads. These simulations are typically carried out using a large-scale parallel atomistic simulation software such as `LAMMPS` [12].

Within the above scheme, the existence of spurious image forces due to the in-plane periodic images and the out-of-plane free or fixed surface are recognized, and attempts have been made to minimize their influence. Typically both L_y and L_z are made sufficiently large such that both the stacking fault width and the Peierls stress of a nominally straight dislocation converge to published values [18, 22, 88, 108]. Satisfying such conditions is the minimum requirement, and does not consider image forces on non-straight dislocations. Thus, often, simulations are repeated with different simulation cell sizes to examine the reliability of the results. However, in many cases, simulations are performed for various periodic dislocation lengths (dimension L_x) so that the simulation cell dimensions, and corresponding image forces, are changing simultaneously with the problem of physical interest.

Here, we examine the spurious image forces arising in a typical dislocation bow-out simulation due to free out-of-plane surfaces and in-plane periodic images exclusively as a function of the normalized simulation cell volume ($\bar{V} = V/L_x^3$), cell aspect ratio (L_y/L_z), and the extent of bow-out of the dislocation. This is accomplished by direct calculation of the image forces using elasticity theory and a continuum representation of the dislocation and its periodic images. We also develop an analytic model that captures the majority of the spurious image forces. With these analyses, we provide a general map of the spurious forces on nominally edge and screw dislocations as a function of the simulation cell dimensions and the extent of dislocation bow-out. We find that the image forces act against

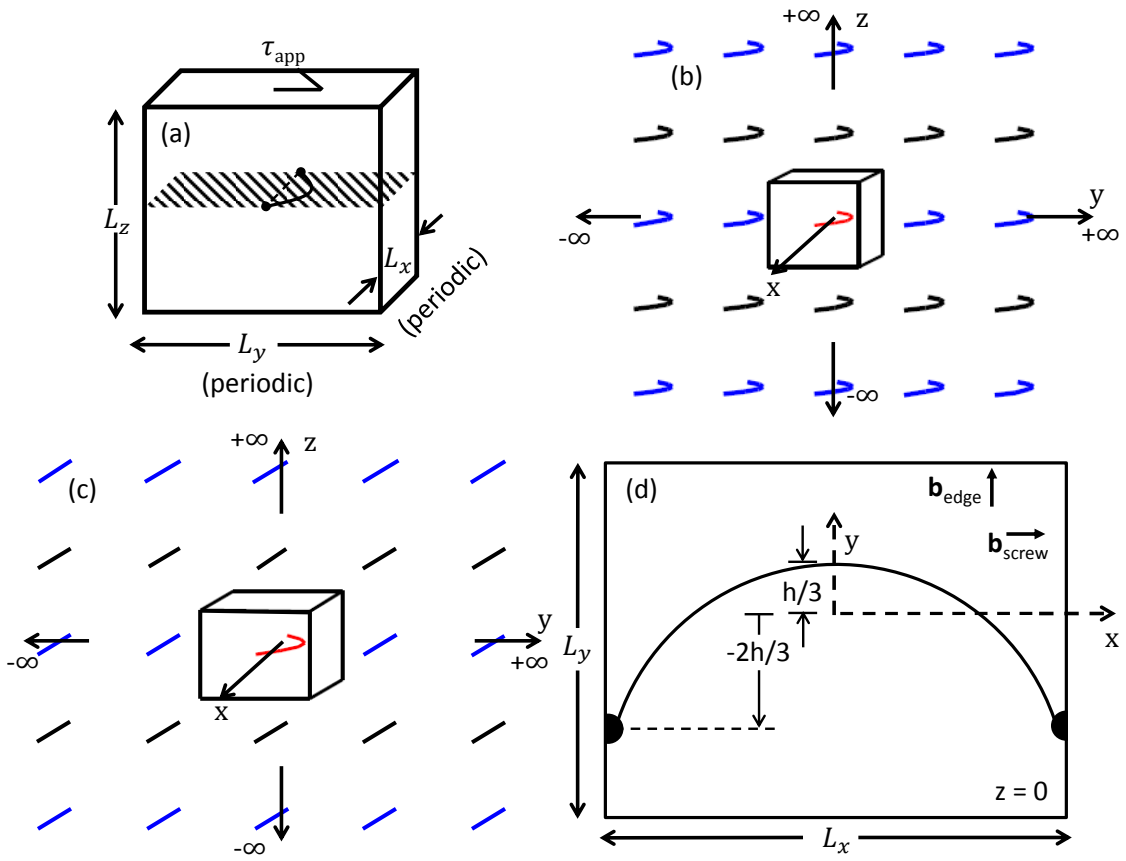

Figure 4.1: (a) Schematic view of the PAD simulation cell containing only the central dislocation; boundary conditions are imposed on the top and bottom surface, while all others surfaces are periodic. (b) Schematic view of the PAD simulation including only two sets of the infinite periodic and image dislocation array (red: primary dislocation along x, blue: images with positive Burgers vectors, black: images with negative Burgers vectors). (c) Schematic of the 2d straight-image-dislocation approximation including only two sets of the infinite periodic and image dislocation array. (d) Top view of the periodic simulation cell depicting a bow-out of extent h and the coordinate system used here with the origin centered at 2h/3 ahead of the pinning points for a dislocation with maximum bow-out h.

the bow-out process, so the applied stress required to achieve any given level of bow-out is larger than in an image-free simulation. The total effect of the image field can be represented by an effective applied stress that counteracts the actual applied stress. We also make a comparison between a bowed-out dislocation in a finite-size simulation cell and in an image-free multiscale simulation [109] and show the difference to be consistent with our computed effective applied stress due to the image forces. We then extend this comparison to several other studies reported in the literature. Our analyses and results provide guidance for estimating image forces in any given PAD simulation or, conversely, for choosing simulation cell sizes and shapes to minimize spurious image forces.

4.2 Methods to Compute Image Forces

The well-known Peach-Koehler equation (e.g. [8]) relates the stress fields ($\boldsymbol{\sigma}$) to the driving force ($\mathbf{F}$) acting on a segment of dislocation ($d\mathbf{l}'$). By projecting this force on to the slip plane (unit normal $\mathbf{n}$) with Burgers vector $\mathbf{b}$,

$$\mathbf{F} \cdot (\mathbf{n} \times \mathrm{d}\mathbf{l}')/|\mathrm{d}\mathbf{l}'|^2 = (\boldsymbol{\sigma}\mathbf{b} \cdot \mathbf{n}) \tag{4.1}$$

the component(s) of stress responsible for glide are obtained. Our goal here is to determine the spurious image stresses, and thus the corresponding spurious Peach-Koehler forces, for the simple problem of a dislocation bowing out around periodically spaced pinning points when simulated by Molecular Statics using the PAD geometry with traction boundary conditions. The geometry of the problem is shown in Fig. 4.1a. We assume a bowed-out dislocation configuration corresponding to an arc with a constant radius of curvature terminating at pinning points on the boundaries of the cell along the x direction, so that in the absence of bow-out the nominal dislocation length is L_x. Fig. 4.1b shows the "image" dislocations that partially satisfy the periodic and free-surface boundary conditions

of the PAD simulation cell. We denote $\tau_{img}^{edge} = \sigma_{yz}|_{x,y,z=0}$ and $\tau_{img}^{screw} = \sigma_{xz}|_{x,y,z=0}$ as the spurious image stress fields at positions (x,y,0) along the (x,y,0) line of the central curved dislocation that arise from the imposed boundary conditions of the (traction) PAD method. Our goal is to compute these image stresses as a function of simulation cell size, cell shape, and dislocation bow-out (curvature). There are three methods to obtain these image stresses. The first method involves solving the posed boundary value problem using a numerical solution via fourier transform methods or Finite Element Methods (FEM) similar to those used in continuum discrete dislocation modeling [101, 110]; both the FEM and fourier transform procedures are general but pose several challenges such as implementation of periodic boundary conditions, computational cost, and complexity, while lacking direct insight and thus are not pursued here. The second method is a direct computation using an infinite array of curved image dislocations, as indicated in Fig. 4.1b, so as to satisfy the imposed *shear* boundary conditions. The third method involves an additional approximation leading to analytic expressions in which the curved image dislocations are replaced by straight dislocations at appropriate positions. For edge dislocations, both the second and third methods require an additional superposed Airy stress function to nullify the *normal* stresses present on the upper and lower surfaces. We discuss and present here both the second and third methods.

4.2.1 Curved Image Dislocations

Our objective is to determine the driving shear stress imposed on a (curved) dislocation configuration with periodicity in the x and y directions confined to the central slip plane, by the boundary conditions $\mathbf{t}|_{z=+/-\frac{L_z}{2}} = \mathbf{0}$. We start by examining two features of existing analytic solutions for the limiting case of a simulation containing only a single, straight, infinite dislocation aligned with the x-axis in an infinite plate, as proposed by Chou [111] for the screw and Nabarro

[112] for the edge. The premise of these solutions involves the superposition of an infinite array of dislocations with alternating Burgers vectors along the out-of-plane direction and an additional Airy stress function for the edge. This scheme is directly extensible to finite dislocation segments and is demonstrated as follows. The stress tensor field at point (x,y,z) generated by a dislocation segment is [8]

$$\begin{aligned}\boldsymbol{\sigma} &= \frac{\mu}{4\pi}\oint(\mathbf{b}\times\nabla')\frac{1}{R}\otimes \mathrm{d}\mathbf{l}' \\ &+ \frac{\mu}{4\pi}\oint \mathrm{d}\mathbf{l}'\otimes(\mathbf{b}\times\nabla')\frac{1}{R} \\ &- \frac{\mu}{4\pi}\oint \frac{\nabla'\cdot(\mathbf{b}\times\mathrm{d}\mathbf{l}')(\nabla\otimes\nabla-\mathbf{I}\nabla^2)R}{(1-\nu)}\end{aligned} \tag{4.2}$$

where μ is the shear modulus, $R = \sqrt{(x'-x)^2+(y'-y)^2+(z'-z)^2}$ and the integrals are taken along the dislocation segment ($\mathrm{d}\mathbf{l}'$) with respect to a field point, $\mathbf{x} = [x, y, z]$. Defining an origin on a *free surface* (unit normal $\mathbf{n}$ oriented along the z direction), two shear stress terms (σ_{xz}, σ_{yz}) and a normal stress (σ_{zz}) arise due to the presence of a dislocation segment having line direction and Burgers vector perpendicular to $\mathbf{n}$, i.e.

$$\begin{aligned}\sigma_{\alpha z} &= \frac{\mu}{4\pi}\oint\frac{\mathbf{n}\cdot(\Delta\mathbf{x}\times\mathbf{b})\mathrm{d}x'_\alpha}{R^3} \\ &+ \frac{\mu}{4\pi}\oint\frac{\Delta x_\alpha(R^2-3z'^2)\mathbf{n}\cdot(\mathbf{b}\times\mathrm{d}\mathbf{l}')}{(1-\nu)R^5}\end{aligned} \tag{4.3}$$

and

$$\sigma_{zz} = \frac{\mu}{4\pi}\oint\frac{(z')(R^2-3z'^2)\mathbf{n}\cdot(\mathbf{b}\times\mathrm{d}\mathbf{l}')}{(1-\nu)R^5} \tag{4.4}$$

where $\Delta\mathbf{x} = [(x'-x),(y'-y),(z'-z)]$ and $\alpha = x, y$.

The *shear* stresses, eq. 4.3, are odd in $\mathbf{b}$ and independent of the side of the plane on which the segment resides (i.e. independent of $sgn(z')$). To annul the shear tractions on both upper and lower surfaces of the plate geometry, we therefore proceed in a similar manner to Chou [111] by superposing alternating

signed dislocation segments outside of the PAD region. Specifically (referring to Fig. 4.1b) for a given dislocation segment within the PAD described by eqs. 4.3 and 4.4 with stress fields $\boldsymbol{\sigma}(+\mathbf{b})$, 2N corresponding segments are placed at distances $z =+/\text{-}iL_z$ with stress fields $\boldsymbol{\sigma}((-1)^i\mathbf{b})$ and $i = 1, 2, 3, ...N$. Within this superposition scheme the resolved *shear* tractions on planes $z =+/\text{-}\frac{L_z}{2}$ as $N \to \infty$ are $\mathbf{0}$.

Second we note that the *normal* stress, eq. 4.4, is both odd in $\mathbf{b}$ and z' and therefore (σ_{zz}) is not necessarily zero on either free surface in the plate geometry when using the above image construction. The plate solution presented by Nabarro [112] edge dislocation uses an Airy stress function $(\chi^s(y, z))$ to annul these surface normal stresses while producing an additional shear stress on the slip plane. To approximately annul the *normal* stress, eq. 4.4, in our problem involving curved dislocations, we include the same Airy stress function as proposed by Nabarro [112] for the straight edge dislocation placed at the origin along the *center-of-mass* line (in the y-direction) of the curved dislocation structure, as indicated in Figs. 4.1c,d. For the circular arc shape considered here, the peak of the bow-out and the *center-of-mass* position of the curved dislocation are at distances h and $2h/3$ ahead of the initial dislocation line, respectively. The origin of the Airy stress function therefore evolves with the bow-out configuration (with increasing h).

The periodicity along the glide direction y of the PAD method is then achieved by superimposing a periodic array of the solutions above for the single dislocation in the infinite plate problem, including the superposition of the Airy stress function evaluated at the *center-of-mass* site of each (edge) dislocation. Since each vertical array plus Airy correction satisfies the desired boundary conditions, the periodic sum over images in the y direction satisfies the desired boundary conditions automatically. For the Airy stress function term, the summation is

$$\tau^{edge}_{img,Airy}(y) = \sum_{i=-N}^{N} - \left(\frac{\partial^2 \chi^s(y,z)}{\partial y \partial z} \right) \Bigg|_{y-iL_y, z=0} \tag{4.5}$$

This discrete sum over i can be simplified using both the angle sum and Lagrange

trig identities resulting in total additional shear stress on the slip plane for a nominally edge dislocation given by

$$\frac{\tau^{edge}_{img,Airy}(y)L_y}{\mu b} = \frac{L_y}{L_z}\int_0^\infty \frac{n^2 \sin(2n\frac{y}{L_y}\frac{L_y}{L_z})\tanh^2(n)\sin((2N+1)(nL_y/L_z))}{\pi(1-\nu)(n-\cosh(n)\sinh(n))\sin(nL_y/L_z)}\mathrm{d}n \tag{4.6}$$

In the limit that $N \to 0$ this additional shear stress term reduces to the result given by Nabarro [112] for the single edge dislocation in an infinite plate.

To implement the above curved image construction, we create the corresponding image dislocations in all three dimensions similar to Fig. 4.1b, but extending out to only a finite number of images (N=25) in each direction, and then add the shear stress generated by the *modified* periodic Airy stress function eq. 4.6 for the nominally edge dislocation. Each curved image dislocation is then represented by a discrete set of straight dislocation segments, i.e. discretized in exactly the same manner as is commonly used in various discrete dislocation simulations. The *modified* periodic Airy stress function is evaluated numerically using the "integral" function within `Matlab`. When the central dislocation is included, the sum over an infinite number of images produces nearly zero tractions on both free surfaces of the simulation cell. To obtain the image forces on the central dislocation, we sum the stress fields of the finite set of discretized image dislocations along the line of the central dislocation. This is similar to nodal force calculations performed within 3d discrete dislocation codes such as `ParaDiS` [34] but we have written a separate code within `Matlab` to obtain the results presented here.

For data presented below in Figs. 4.2 and 4.3, we have used 25 periodic images of the central dislocation in all three directions x, y, and z with 5 segments per image. We have performed similar calculations using only 13 images in all directions and also using a small finite-sized obstacle rather than a point obstacle in pinning the dislocation. The differences in results are negligible. The finite size of our image array leads to shear stresses on the out-of-plane surfaces of at most

2 MPa, so that these surfaces are not truly traction free over the entire surface area, and this error decreases with increasing images as expected. Correcting for these stresses would lead to image stresses on the central dislocation that differ from our results by *less than* 2 MPa. Using the finite image array, we then calculate the driving stress τ_{yz} or τ_{xz} along the line of the curved central dislocation. We repeat this type of calculation for a range of simulation cell dimensions and magnitudes of dislocation bow-out for both nominally edge and screw dislocations.

4.2.2 Approximation using Straight Image Dislocations

Numerical computations of the image stresses of the curved dislocations can be performed but do not provide significant insights. Since the image dislocations are not usually too close to the central dislocation, the role of their curvature is decreased as the simulation cell size is increased. We therefore consider an image array where the curved image dislocations are replaced by a set of straight image dislocations, shown in Fig. 4.1c. This approximation allows for analytic estimates of the image stresses on the central curved dislocation. We account for the bow-out of the central curved dislocation by using a coordinate system for the image dislocations identical to that described in the previous section for the Airy stress function, where the origin is located at the *center-of-mass* line of the central bow-out ahead of the initial dislocation position, as indicated in Fig. 4.1d. For a dislocation bowing out in to a circular arc, the *center-of-mass* position is very accurately located at $2h/3$ ahead of the initial position, almost independent (within 2%) of the amount of bow-out h/L_x. Specifically, we define an (x,y,z) coordinate system with the x axis lying along the position $2h/3$ of the bow-out, so that the actual curved dislocation line ranges from the positions $(-L_x/2, -2h/3)$ and $(L_x/2, -2h/3)$ at the pinning points to $(0, h/3)$ at the point of greatest bow-out. The straight image dislocations then translate with the evolving bow-out in h, and always replicate the mean burgers vector distribution of the curved dislocation

structure. This simplification neglects dipolar dislocation segments with spacing and length on the order of L_x and h, leading to an error in the stress scaling as $\sim \mathcal{O}(\frac{bhL_x}{L_y^3})$.

The image stress at position (x,y,0) in the plane of the central dislocation is then given by the sum of the stresses due to the *2-dimensional* array of straight image dislocations and the *modified* periodic Airy stress function for the straight edge dislocation. The stress field of a 1-dimensional array of infinite straight edge dislocations aligned along the x axis and with periodicity L_y is given by [8],

$$\frac{\sigma_{yz}^{1d-edge}(Y,Z)L_y}{\mu b} = \frac{\sin(Y)(\cosh(Z)-\cos(Y)-Z\sinh(Z))}{2(1-\nu)(\cosh(Z)-\cos(Y))^2} \tag{4.7}$$

and similarly for the screw

$$\frac{\sigma_{xz}^{1d-screw}(Y,Z)L_y}{\mu b} = \frac{\sin(Y)}{2(\cosh(Z)-\cos(Y))} \tag{4.8}$$

where $Y(y) = 2\pi y/L_y$ and $Z(z) = 2\pi z/L_y$. For a 2-d periodic array with spacing L_z and alternating Burgers vectors, the stress field is obtained by shifting the 1-d solution by integer units of L_z, alternating the sign of the Burgers vector, and summing over all the images, leading to

$$\sigma_{yz}^{2d-edge}(y,z) = \sum_{n=-\infty}^{+\infty} (-1)^n \sigma_{yz}^{1d-edge}(Y, Z(z-nL_z)) \tag{4.9}$$

and

$$\sigma_{xz}^{2d-screw}(y,z) = \sum_{n=-\infty}^{+\infty} (-1)^n \sigma_{xz}^{1d-screw}(Y, Z(z-nL_z)) \tag{4.10}$$

We note the work of Cai and coworkers [113, 114] on conditional convergence issues related to these (2D) summations. In the most general case, a linear term and a constant spurious term arise due to the $\sim 1/R$ stress fields being summed over a 2d ($\sim RdR$) domain. For these two specific cases (eq. 4.9 and 4.10), it has been demonstrated [113] that the correction terms are zero, and hence absolute convergence is possible.

The image stresses should not include the stress due to the central dislocation itself, and so the approximate image stress fields in the (x,y,z=0) plane are

$$\tau_{img}^{edge}(y) = \tau_{img,Airy}^{edge}(y) + \sigma_{yz}^{2d-edge}|_{z=0} - \frac{\mu b}{2\pi y(1-\nu)} \tag{4.11}$$

and

$$\tau_{img}^{screw}(y) = \sigma_{xz}^{2d-screw}|_{z=0} - \frac{\mu b}{2\pi y} \tag{4.12}$$

which depend on the 2-d aspect ratio L_y/L_z. We numerically evaluate eqs. 4.11, and 4.12 for a range of aspect ratios and for positions y(x) along the line of the bowed out dislocation ($-L_x/2 < x < L_x/2$). We truncate the infinite summation at $|n| \leq 1001$ leading to $< 0.1\%$ error in the shear tractions on the upper and lower surfaces.

4.2.3 Analytic Scaling of Image Forces and an Effective Image Stress

To gain insight into the scaling of the image stress fields with respect to both the cell dimensions and bow-out, we analyze the results of the previous section further. Recognizing that y/L_y is small because $|y| \leq h$ and $h \leq L_y$ (see Fig. 4.1d), we expand 4.11 and 4.12 to first order in y/L_y. Defining the out-of-plane aspect ratio as $\bar{L} = L_y/L_z$, the image stress at the position $y(x)$ along the curved dislocation can be written as

$$\frac{\tau_{img}^{edge}[y(x)]L_y}{\mu b} = [\bar{L}^2 A(\bar{L}) + B(\bar{L})]\left(\frac{y(x)}{L_y}\right) \tag{4.13}$$

and

$$\frac{\tau_{img}^{screw}[y(x)]L_y}{\mu b} = C(\bar{L})\left(\frac{y(x)}{L_y}\right) \tag{4.14}$$

where

$$
\begin{aligned}
A(\bar{L}) =& \frac{2}{\pi(1-\nu)} \int_0^\infty \frac{n^3 \tanh^2(n) \sin((2N+1)(n\bar{L}))}{(n - \cosh(n)\sinh(n)) \sin(n\bar{L})} \mathrm{d}n \\
B(\bar{L}) =& \frac{\pi}{(1-\nu)} \left[\sum_{n=1}^{\infty} (-1)^n \operatorname{csch}^2\left(\frac{n\pi}{\bar{L}}\right) \left(1 - \frac{2n\pi}{\bar{L}} \coth\left(\frac{n\pi}{\bar{L}}\right)\right) - \frac{1}{6} \right] \\
C(\bar{L}) =& 2\pi \left[\sum_{n=1}^{\infty} \frac{(-1)^n}{\cosh\left(\frac{2\pi n}{\bar{L}}\right) - 1} - \frac{1}{12} \right]
\end{aligned}
\tag{4.15}
$$

This approximate image stress field thus scales directly with the distance y from the origin, with $-2h/3 < y < h/3$, and has no explicit dependence on L_x, as expected. Several further manipulations can then be made. First, a general reference stress for dislocation bow-out problems is the Frank-Read source operation stress, which scales as $\tau_{FR} \sim \frac{\mu b}{L_x}$. Second, since the cost of molecular simulations scales directly with the volume of the simulation cell, we define a normalized volume $\bar{V} = L_y L_z / L_x^2$. Introducing these quantities into eqs. 4.13 and 4.14, we obtain the image stress fields in terms of $\bar{L}$ and $\bar{V}$ as

$$
\tau_{img}^{edge}[y(x)] = \left(\frac{\mu b}{L_x}\right) \left(\frac{y(x)}{L_x}\right) \bar{\tau}_{img}^{edge}(\bar{L}, \bar{V}) \tag{4.16}
$$

$$
\tau_{img}^{screw}[y(x)] = \left(\frac{\mu b}{L_x}\right) \left(\frac{y(x)}{L_x}\right) \bar{\tau}_{img}^{screw}(\bar{L}, \bar{V}) \tag{4.17}
$$

where we have defined the dimensionless image stress gradient as

$$
\bar{\tau}_{img}^{edge}(\bar{L}, \bar{V}) = \frac{\bar{L}^2 A(\bar{L}) + B(\bar{L})}{\bar{V}\bar{L}} \tag{4.18}
$$

and

$$
\bar{\tau}_{img}^{screw}(\bar{L}, \bar{V}) = \frac{C(\bar{L})}{\bar{V}\bar{L}} \tag{4.19}
$$

While the image stress *fields* along the line of the dislocation (eqs. 4.16 and 4.17) provide insight, they are not directly interpretable relative to the *true* applied stress and the *nominally* applied stress in a PAD simulation. Consequently, we now derive an *effective* image stress, $\tau_{img,eff}$, that is (i) spatially constant,

that (ii) represents the net effect of the image forces on the bowing dislocation, and that can be (iii) directly subtracted from the nominally applied stress in a PAD simulation. The *effective* image stress $\tau_{img,eff}$ is determined as a net configurational force acting on the bowing out dislocation in the following manner. Imagine a dislocation bowed out into an arc of a circle with maximum bow-out h and consider an incremental increase in both the bow-out and the 2d image array so that the maximum bow-out is $h + \delta h$ while the image array translates by $\frac{2}{3}\delta h$. We denote the incremental area swept out as δA. Through this process, the image stress *field* $\tau_{img}[y(x)]$ acts along the arc of the dislocation, in some places pushing the dislocation forward and in places pushing it back. The total incremental work done by the image stresses in making the incremental motion ($\mathrm{d}A = A(h + \delta h) - A(h)$) is

$$\delta W = \iint\limits_{A} \tau_{img}[y(x)] b \mathrm{d}A \tag{4.20}$$

Using the analytic expressions for $\tau_{img}[y(x)]$ in Eq. 4.16a or b, the work can be computed to first order in h/L_x as

$$\delta W \approx \left(\frac{\mu b^2}{L_x}\right)\left(\frac{4h}{45L_x}\right)\bar{\tau}_{img}(\bar{L},\bar{V})\delta A \tag{4.21}$$

for the edge and similarly for the screw. The net incremental work when including the *effective* image stress acting over the same incremental area however must be zero, so

$$\iint\limits_{A} \tau_{img,eff} b \mathrm{d}A = -\delta W \tag{4.22}$$

and hence our final estimate for the effective image stress is

$$\tau^{edge}_{img,eff} \approx -\left(\frac{\mu b}{L_x}\right)\left(\frac{4h}{45L_x}\right)\bar{\tau}^{edge}_{img}(\bar{L},\bar{V}) \tag{4.23}$$

and

$$\tau^{screw}_{img,eff} \approx -\left(\frac{\mu b}{L_x}\right)\left(\frac{4h}{45L_x}\right)\bar{\tau}^{screw}_{img}(\bar{L},\bar{V}) \tag{4.24}$$

4.3 Results

We start by comparing the results of the 3d curved image array and the 2d straight image approximation, 4.16 and 4.17. The independent variables which determine the image stress field are the two characteristic simulation cell dimensions $\bar{L}$ and $\bar{V}$. The image stress field, normalized by the Frank-Read stress, acting along the bow-out dislocation position, $(y(x) + 2h/3)/L_y$ as predicted by the analysis 4.16, 4.17 and the 3d curved image array is shown in Figs. 4.2a,b for edge and screw dislocations, respectively, for several different normalized volumes ($\bar{V} = L_y L_z / L_x^2$). Agreement between the fully numerical and analytical results is very good along the entire line in all except the most extreme cases, e.g. $\bar{V} < 0.3$. While the image stress field generated by the curved dislocation array is complex, the 2d-model captures the essential physics, scaling, and magnitude of the image fields. Both analyses also demonstrate that the magnitude of the image stresses is largest at the pinning points (positive, acting to push the dislocation outward) and near the peak (negative, acting to oppose increased bow-out).

We verify the agreement between the 3d curved image array and the 2d analysis more generally in the following manner. The image stresses at position (x,y,0) are uniquely specified by the y coordinate since x is a function of y. We therefore use a normalized position y/h ranging from $-2/3$ at the pinning points ($x = +/-L_x/2$) to $+1/3$ at the point of peak bow-out ($x = 0$) in accordance with Fig. 4.1d. The scaling analysis, eqs. 4.16,4.17 and 4.18,4.19, suggests that the image stress *field* is proportional to both the Frank-Read stress, $\mu b/L_x$ and the extent of bow-out, h/L_x, and scales inversely with the normalized volume ($\bar{V} = L_y L_z / L_x^2$). Figures 4.3a,b show the normalized image stress *fields* ($\tau_{img}[y(x)]/\left[(\mu b/L_x)(h/L_x)\right]$) at the two extremities of the bow-out (i.e. the peak: $(x = 0, y = h/3)$ and the

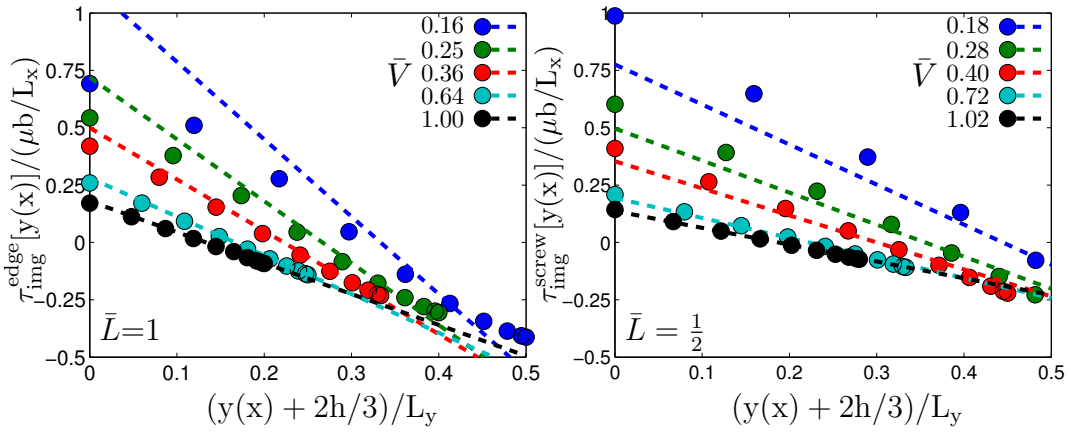

(a) **Edge** (b) **Screw**

Figure 4.2: (a) Edge and (b) Screw. Image stress *field*, normalized by the Frank-Read stress ($\mu b/L_x$), versus normalized position along the (curved) dislocation line for several normalized volumes ($\bar{V} = L_y L_z / L_x^2$) and $h = 0.2L_x$, as predicted by the 3d discrete analysis (symbols) and by the 2d model (dashed lines). The curved dislocation spans the range from the pinning point, $y(x) = -2h/3$ (and hence $(y(x) + 2h/3)/Ly = 0$), to the peak $y(0) = h/3$ (and hence $(y(x) + 2h/3)/Ly = h/Ly$). For the cases h=0.2Lx shown here, the peak is then at $0.2(Lx/Ly) = 0.2/\sqrt{\bar{L}\bar{V}}$.

pinning points: $(x = +/- L_x/2, y = -2h/3)$) for a wide range of cell aspect ratios ($\bar{L} = L_y/L_z$), normalized volumes ($\bar{V} = L_y L_z / L_x^2$), and extents of bow-out (h/L_x), (i) as computed numerically (symbols) and (ii) as predicted by the analytic model (dashed lines) for the entire bow-out ($-2/3 \leq \frac{y(x)}{h} \leq 1/3$). In general, the results for different amounts of bow-out h collapse very well using this normalization. The analytic model and the numerical model agree quite well where $h/L_y << 1$; at larger h/L_y the neglected curvature in the 2d analytic model becomes non-negligible.

Having validated the 2d analysis against the 3d analysis, we now note several predicted scalings that emerge from the 2d analysis (eqs. 4.16,4.17 and eqs. 4.23,4.24). Both eqs. 4.16,4.17 and 4.23,4.24 show that the effects of cell simulation dimensions are contained in the quantities $\bar{\tau}^{edge}_{img}$ and $\bar{\tau}^{screw}_{img}$. Figure 4.4 thus shows these quantities, multiplied by the normalized volume $\bar{V}$, as a function of $\bar{L}$. As expected, for larger overall cells, the magnitude of the image stress decreases.

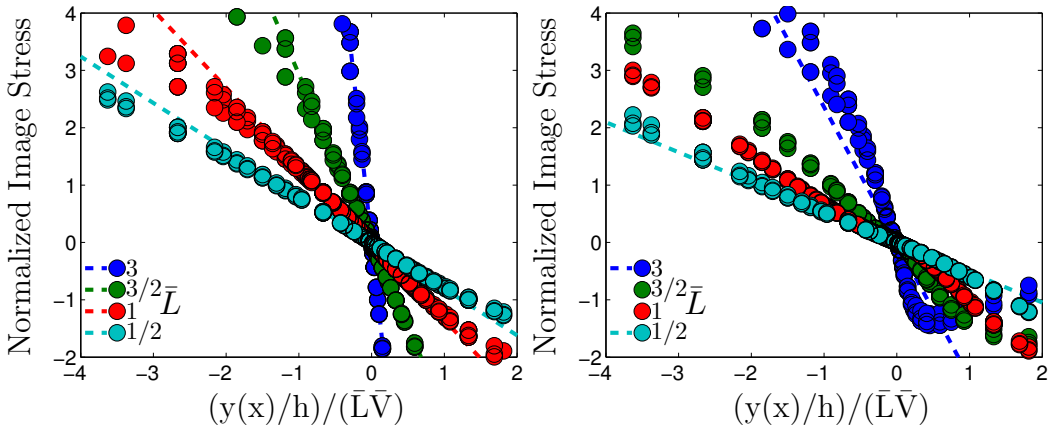

(a) **Edge** (b) **Screw**

Figure 4.3: (a) Edge and (b) Screw. Normalized image stress (image stress *field*, $\tau_{img}[y(x)]$, divided by Frank-Read stress, $\mu b/L_x$, and extent of bow-out, h/L_x) versus ratio of the normalized position along the dislocation line, $y(x)/h$, to the product of the normalized volume and aspect ratio, $\bar{V}\bar{L}$, (i.e. (y(x)/h)/($\bar{L}\bar{V}$)) for several aspect ratios as predicted by the 3d discrete analysis (symbols) and by the 2d analysis (dashed lines) for the peak ($y = h/3$) and pinning point ($y = -2h/3$).

However, there are wide variations in the trend as a function of the aspect ratio ($\bar{L}$). Therefore, the choice of simulation cell aspect ratio and normalized volume can have a significant affect on the apparent stresses and thus both simulation cell volume and shape must be chosen carefully. Other trends emerging from the analysis are that:

1. For a fixed nominal dislocation line length L_x, and fixed aspect ratio $\bar{L} = L_y/L_z$, the normalized image stress scales inversely with the simulation volume.

2. For an initial dislocation line length L_x and fixed volume V, the normalized image stress depends only on $\bar{L}$.

3. With varying length L_x, the normalized image stress is constant for constant normalized volume $\bar{V}$ and constant aspect ratio $\bar{L}$; in other words, increasing the overall system size proportionally has *no affect* on the normalized image stress.

4. For a given volume $\bar{V}$ there is an optimal aspect ratio $\bar{L}$ to minimize the image stresses independent of L_x, with $\bar{L}_{opt} \approx 0.8$ for the edge and $\bar{L}_{opt} \approx \sqrt{2}$ for the screw.

5. Since a bow-out of h scales with the applied stress as $\tau_{app} \sim (\mu b/L_x)(h/L_x)$, the effective image stress scales with the true applied stress, i.e. $\tau_{img,eff}/\tau_{app}$ remains constant, independent of the applied stress.

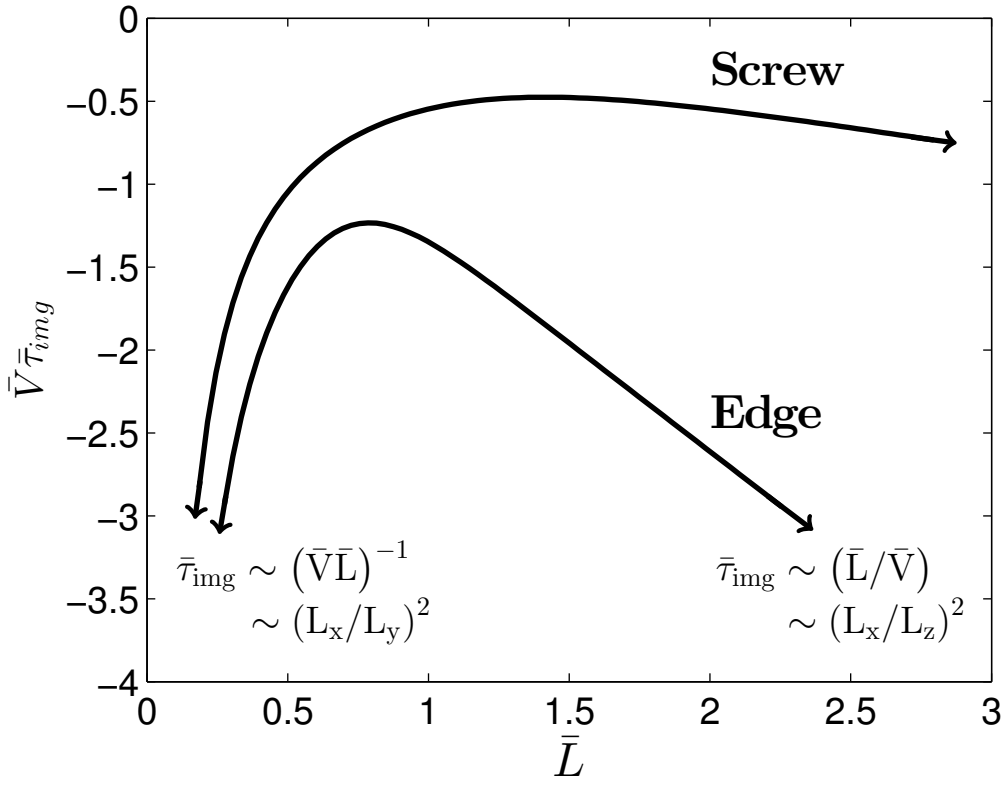

Figure 4.4: Dimensionless image stress gradient ($\bar{\tau}_{img}$) times normalized volume ($\bar{V} = \frac{L_y L_z}{L_x L_x}$) versus aspect ratio ($\bar{L} = \frac{L_y}{L_z}$) for the nominally edge and screw dislocation. The asymptotic behavior of $\bar{\tau}_{img}$ for $\bar{L} >> 1$ and $\bar{L} << 1$ is shown to be $\sim 1/L_z^2$ and $\sim 1/L_y^2$ respectively. The *optimal* aspect ratio which minimizes spurious image stress for the nominally edge dislocation is $\bar{L}_{opt} \approx 0.8$ and for the nominally screw dislocation is $\bar{L}_{opt} \approx \sqrt{2}$.

4.4 Discussion & Application

Our results show that the *effective* normalized image stress is approximately quadratic in L_x because of the inverse relationship with the normalized volume ($\frac{\tau_{img,eff}}{(\frac{\mu b}{L_x})(\frac{h}{L_x})} \sim \bar{V}^{-1} \sim L_x^2$). Thus, a typical study in which L_y and L_z are fixed and the length L_x is varied to study the effects of obstacle spacing can lead to large variations in image stresses that contaminate the intended measurements. Fig. 4.4 shows a large difference in the dimensionless image stress gradient, eqs. 4.18 and 4.19 between a nominally edge and screw dislocation PAD simulation. The dimensionless image stress gradient for the screw dislocation is much smaller than that for the edge e.g. $\left.\frac{\bar{\tau}_{img}^{screw}}{\bar{\tau}_{img}^{edge}}\right|_{\bar{L}=1} \approx \frac{1}{3}$. Furthermore, at a fixed applied stress,

a nominally edge dislocation is expected to bow-out more than a screw dislocation at the same applied stress due to the reduced *line tension* making the image stress, relative to the applied stress, much larger for the edge dislocation. For the nominally edge dislocation both the increased dimensionless image stress gradient and the increased bow-out at a fixed applied stress suggest that the image stress relative to the applied stress is generally much greater for the nominally edge dislocation. With all of these subtleties, extracting quantitative results from parametric studies requires a sufficiently large minimum cell volume as to mitigate spurious image type effects all together.

We now demonstrate, through example, the interpretation and usage of Fig. 4.4 as a guide to the design of studies involving dislocation/obstacle interactions. We examine a typical simulation of a nominally edge dislocation impinging on obstacles with spacing $L_x = 50$ nm in Al (FCC, lattice constant a = 4.03 $\mathring{A}$, atomic density = $61\frac{atoms}{nm^3}$). We start by considering equal glide and out-of-plane periodic lengths, $L_y = L_z = 40$ nm for simplicity. These dimensions lead to $\bar{V} = L_y L_z / L_x^2 = 0.64$ and $\bar{L} = L_y / L_z = 1$. The number of atoms required for this simulation follows as $N = (L_x^3)(\bar{V})(61/nm^3) \approx 4.9$ million atoms. One or a few calculations at this size are computationally feasible, however numerous computations of this size quickly become computationally expensive. From Fig. 4.4, we find that $\bar{\tau}_{img}^{edge} \approx -1.4/0.64 = -2.19$ and the effective image stress is thus $\tau_{img,eff} = 2.19(\mu b/L_x)(4h/45L_x)$ at bow-out h. If this magnitude is acceptable, we might wish to use half the number of atoms and the same aspect ratio $\bar{L} = 1$, or $L_y = L_z = 28.3$nm. The effective image stress would then double because the volume is halved at fixed $\bar{L}$. But if instead we halved the number of atoms by changing the aspect ratio to $\bar{L} = 0.8$ with $L_y = 25.3$ nm, $L_z = 31.6$nm, and thus $\bar{V} = 0.32$, we obtain an effective image stress of $\tau_{img,eff} = 3.91(\mu b/L_x)(4h/45)$ which is less than twice the original value.

To further validate our analysis quantitatively, we now compare results in a typical PAD simluation and in a multiscale image-free simulation [109] of the same

problem: bow-out of a pinned nominally edge dislocation under an applied stress. The studies were performed on Al using the Ercolessi-Adams [115] EAM potential having material properties $\mu = 30.8$ GPa, $|\mathbf{b}| = 2.85$ $\mathring{A}$ and $\nu = 0.35$, with an obstacle spacing of $L_x = 50$ nm. The PAD simulation, reported in [116], used dimensions $L_y = L_z = 20$ nm. The multiscale image-free simulation was performed using the Coupled Atomistic/Discrete Dislocation (CADD) method [109, 117], in which an atomistic domain is embedded in a fully anisotropic continuum elastic domain with a seamless atom/continuum interface that introduces no spurious forces. The multiscale simulation corresponds effectively to infinite dimensions L_y, L_z. In Fig. 4.5, we show the equilibrium configurations of three curved dislocation structures: two using the traction PAD method [116] under a PAD simulation applied stresses of ~ 30 MPa and ~ 45 MPa and one using the multiscale image-free method [109] under a (true) applied stress of ~ 30 MPa. The traction PAD simulation at ~ 45 MPa closesly matches the image-free result at ~ 30 MPa, indicating that the image stresses correspond to an effective applied stress of ~ 15 MPa, one-half of the true applied value. The traction PAD simulation at a simulation stress equal to that in the multiscale simulation, ~ 30 MPa, exhibits significantly less bow-out; in fact, the peak bow-out is approximately 2/3 that of the traction PAD simulation at 3/2 larger applied stress, as expected since both the bow-out and the effective image stress scale with the applied stress. We now use our results to predict the effective image stress. For this PAD simulation cell, $\bar{L} = 1$ and $\bar{V} = 0.16$. From Fig. 4.4, we find $\bar{\tau}^{edge}_{img} = -(1.4/0.16)$ and thus from eq. 4.23a $\tau^{edge}_{img,eff} = (1.4/0.16)(\mu b/L_x)(4h/45L_x)$. From Fig. 4.5, $h/L_x \approx 0.14$ and so $\tau^{edge}_{img,eff} = 18.4$ MPa. The predicted effective image stress agrees very well with the measured image stress, with an error of $\approx 25\%$. The over-estimate for this particular case is consistent with Fig. 4.2a, where the analytic 2d result (dashed blue line) over-estimates the numerical 3d result (symbols) for $\bar{V} = 0.16$.

Finally, we extend the analyses to several dislocation/obstacle simulation studies available within the literature. In Table 4.1 we report the absolute dislocation

line length L_x, aspect ratio ($\bar{L}$), and normalized volume ($\bar{V}$) reported for various simulation cells. For these values, we compute the normalized *effective* image stress ($\tau_{img,eff} / \left[\left(\frac{\mu b}{L_x}\right)\left(\frac{4h}{45L_x}\right)\right]$) for studies involving nominally edge and screw dislocations. We note that the normalized effective image stress for the PAD depicted in Fig. 4.5 corresponds to the value ~ 8.2 which corresponded to an error of $\approx 50\%$ (45 MPa versus 30 MPa) in the applied stress. With the exception of the simulation reported by Cheng and coworkers [14], all of the other edge studies have effective image stresses that are comparable to or worse than the result in Fig. 4.5. Osetsky [118] and Dong [116] attempted some limited convergence studies by increasing the simulation cell in the in-plane direction (L_y) for a fixed obstacle spacing. As predicted by 4.18, however, these studies reproduced nearly the same normalized effective image error while adding computational cost with the approximately doubled volume. Thus, although the coarse results appear to have converged, they still have the same image error embedded in the results! Several similar studies involved "*strain*" controlled boundary conditions on the top and bottom surfaces, where the dislocation is driven by an imposed displacement rather than an imposed stress. As noted by Rodney [119], the image stresses for the displacement boundary conditions are expected to be comparable to, but larger than, those for traction control. Our estimates of the effective image stresses are thus probably conservative in these cases. Table 4.1 also shows the normalized effective image stress for three nominally screw simulation cells [21] *but for illustrative purposes only* because the actual studies did not involve bow-out type configurations confined to the central slip plane. We conclude with a brief, general discussion about testing the size of simulation cells for converged simulation results. As seen in Table 4.1, it is remarkably easy to change a single length of the simulation cell, either the out-of-plane length L_z or the periodic glide length L_y, and recover a "*converged*" yet wrong result. Examination of eqs. 4.18, 4.19 and Fig. 4.4 provides a quantitative explanation for this, demonstrating that when $\bar{L} >> 1$ or $\bar{L} << 1$ changing L_y or L_z, respectively, has virtually no influence on

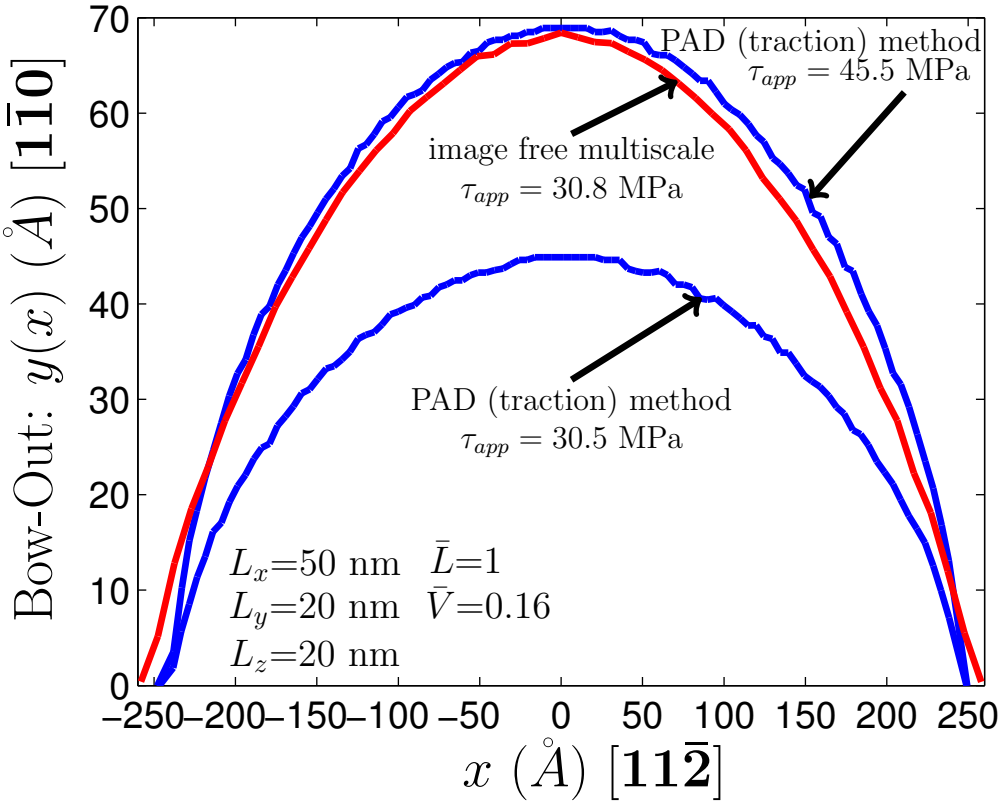

Figure 4.5: Equilibrium configurations of a nominally edge dislocation bowing out under an applied stress using the traction PAD method [116] (blue) and an image free multiscale method [109] (red). The PAD simulation cell contained an obstacle spacing of L_x= 50 nm with periodicity and free surfaces a distance $L_y = L_z = 20$ nm. Two PAD bow-outs are depicted under a nominal applied stress of $\sim$ 30 MPa and $\sim$ 45 MPa. A single artifact free bow-out is shown at an applied stress of $\sim$ 30 MPa corresponding with the PAD bow-out of $\sim$ 45 MPa. For this simulation cell geometry, nominal dislocation structure (edge) and Ercolessi-Adams [115] potential: $\frac{\tau^{edge}_{img,eff}}{\tau_{app}} \approx 50\%$. Partial dislocations were detected using a common neighbor analysis and averaged to yield a single, continuous center line for the dislocation bow-out.

the image stress. Instead, fixing the aspect ratio ($\bar{L}$) to the optimum value and varying the normalized volume ($\bar{V}$) is a more suitable method to test for converged results.

Edge	L_x (nm)	$\bar{L}$	$\bar{V}$	$\tau^{edge}_{img,eff} / \left[\left(\frac{\mu b}{L_x}\right)\left(\frac{4h}{45L_x}\right)\right]$
Osetsky* *et. al.* [118] C1	41.4	1.5	0.33	5.8
C2	41.4	3	0.66	5.8
C3	83	1.5	0.085	22.5
Cheng *et. al.* [14]	28	2	1.02	2.5
Dong [116]	50	1	0.16	8.2
	80	1	0.063	20.9
	80	1.7	0.11	20.3
	80	2.1	0.13	20.3
Screw				$\tau^{screw}_{img,eff} / \left[\left(\frac{\mu b}{L_x}\right)\left(\frac{4h}{45L_x}\right)\right]$
Rodney* [21]	20	1.38	0.85	0.6
	37.3	1.38	0.24	2.0
	59.7	1.38	0.1	4.8

Table 4.1: Simulation cell obstacle spacing (L_x), aspect ratio ($\bar{L} = L_y/L_z$), normalized volume ($\bar{V} = L_y L_z / L_x^2$), and resulting normalized *effective* image stress analysis, eqs. 4.23 and 4.24 applied to several dislocation/obstacle interaction studies (ν=1/3). The dimensionless image stress gradient has been calculated directly from 4.18 and 4.19 for the nominally edge and screw dislocation respectively. When $\bar{L} >> 1$ or $\bar{L} << 1$ doubling the simulation volume can result in an identical (and non-negligible) image stress (e.g. Osetsky [118] C1 and C2 and Dong [116]). *These simulations were performed using either a "*strain*" controlled (Osetsky [118]) or alternatively bounded (Rodney [21]) PAD and so the computation of $\bar{\tau}_{img}(\bar{L}, \bar{V})$ remains inexact. As noted by Rodney [119] however, it is expected to be comparable to, but larger in the case of "*strain*" control due to the mismatch between the curved dislocation structure and straight dislocation field within the PAD region

4.5 Summary

We have investigated the nature of undesirable spurious image stresses arising from the bowing out of a dislocation around obstacles in a finite sized atomistic simulation volume, and have provided a general map of the magnitude of the spurious effects as a function of the simulation cell size and shape. We have further demonstrated that, independent of the cell size, these image stresses scale with the nominally applied load. For both a nominally edge and screw dislocation, we have found special aspect ratios ($\bar{L} = L_y/L_z$) which minimize spurious image forces for a given number of atoms (given simulation volume). We have made a direct comparison between a dislocation structure under an applied load in a

finite simulation cell and an image-free multiscale simulation [109] of the same problem, showing that our analysis is quantitatively accurate. Finally, we have evaluated the image stresses that would have arisen in several other studies within the literature, predicting comparable errors. Overall, this work provides a clear and simple benchmark for designing atomistic simulations with controlled and minimized image effects in the many physical situations involving dislocation bow-out.

Chapter 5

Robust Atomistic Calculation of Dislocation Line Tension

5.1 Introduction

The onset of flow in metals is governed by the inhibition of dislocation glide through the crystalline lattice. Dislocations are pinned by various types of obstacles, with applied stress and thermal activation allowing the dislocations to move through a field of obstacles [17, 18, 21, 22, 31, 32, 79, 80, 88, 108, 118, 120–124]. Increasingly sophisticated models are guiding the understanding of these processes, and their consequences on observable/measurable phenomena [23, 36, 38, 125, 126]. Central to many of these models is the concept of the dislocation line tension Γ, which is associated with the energy required to form curved dislocation structures. Formally, the line tension is related to the infinitesimal change in energy δW associated with an infinitesimal change in dislocation length δS [8, 127–129]

$$\Gamma = \lim_{S \to 0} \frac{\delta W}{\delta S}. \tag{5.1}$$

Dislocation line tension is thus a function of the dislocation configuration, which is implicitly contained in W and S. For simplicity, the line tension Γ is often assumed to be a local quantity, i.e. associated with local line length and curva-

ture. However, Γ actually consists of contributions from both the local increase in dislocation length and the longer-range interactions among all segments of the dislocation line, which leads to a $ln(L)$ scaling with line length L. A simple approximation, $\Gamma \approx \frac{1}{2}\mu b^2$ [37, 122, 123, 130–135], where μ is the shear modulus and b the Burgers vector was originally proposed over half a century ago [133, 134]. A more nuanced model accounts for the long-range interactions by modifying the prefactor of 1/2 and adding the $ln(L)$ scaling that emerges from elasticity. Such estimates of Γ have provided insight into a range of key processes in materials, such as dislocation junction formation and breaking, [90, 131, 136, 137], dislocation-obstacle interactions [17, 18, 88, 120], and solute strengthening models [23, 36]. Many of these models for dislocation pinning by obstacles lead to predictions for the critical resolved shear stress (CRSS) τ_c of the form

$$\tau_c = \alpha\Gamma/bL \tag{5.2}$$

where L is the distance between pinning points, and α is a parameter related to the local dislocation/obstacle interactions. Additionally, numerical methods (2D [100] and some 3D discrete dislocation dynamics [34, 35, 110, 138]) rely on a phenomenological line tension to avoid the singular fields associated with elasticity. Continuum dislocation line models also rely on the assumption that dislocations are adequately represented by smooth curves or discretized straight segments, and that the atomic-scale phenomena of the Peierls stress τ_P can be accurately represented as a homogeneous stress opposing motion of the dislocation. If these assumptions are valid, direct atomistic simulations are then also required to calibrate the "material parameters" (line tension Γ, dislocation core energy E_{core}, Peierls stress τ_P, dislocation mobility B, and their variations with dislocation character ranging from screw to edge) that enter into the continuum model. As computational materials science moves into an era of increasing accuracy and predictive capability for τ_c, accurate values for all of the material parameters, including dislocation line tension, become increasingly important.

As a result of this importance, and with the increasing availability of efficient parallelized molecular dynamics algorithms [12], a number of attempts have been made to calculate the line tension directly from atomistic simulations [14, 23, 85, 121, 139–143]. The simplest realization of such a calculation is the periodic small bow-out problem [8] in which an infinite initially-straight dislocation is pinned at a periodic array of obstacles with a spacing L. A driving resolved shear stress τ_{app} is then applied, causing the free regions of the dislocation to bow-out in between the pinning points, as shown in figure 5.1; this problem is thus closely related to models of strengthening via pinning of dislocations. The work $\tau_{app} b d\mathrm{A}$ done by τ_{app} over the incremental area $d\mathrm{A}$, over which the upper and lower surfaces are displaced relatively by one Burgers vector b, is balanced by the additional energy ΓdS of the line tension eq. 5.1 associated with the incremental increased length dS of the dislocation. An equilibrium configuration is achieved when these incremental energies (i.e. configurational forces) are equal, so that the line tension can be directly related to the evolving shape of the dislocation as

$$\Gamma = \tau_{app,eff} b \frac{\mathrm{d}A}{\mathrm{d}S} \tag{5.3}$$

Bacon, Osetsky and Rodney [87] have reviewed many of the methods employed in this type of calculation for obstacles such as clusters of solute atoms, vacancies, and recently forest dislocations. Unfortunately, previous atomistic studies have yielded vastly different results for the same dislocation in the same material, e.g. an edge dislocation in Al as described by a given interatomic potential. Attempts have been made to identify and compensate for spurious boundary-induced stresses [116, 140, 144], inertial effects [14], artificial pinning-point interactions [22, 121], and the Peierls stress τ_P. The Peierls stress, usually measured on a straight dislocation, is either treated as a uniform applied internal back stress so that the effective applied stress is $\tau_{app} - \tau_P$ or is neglected. After such adjustments/corrections, however, the literature values for the line tension of an edge dislocation in Al using the Ercolessi-Adams (EA) EAM potential range from 0.06

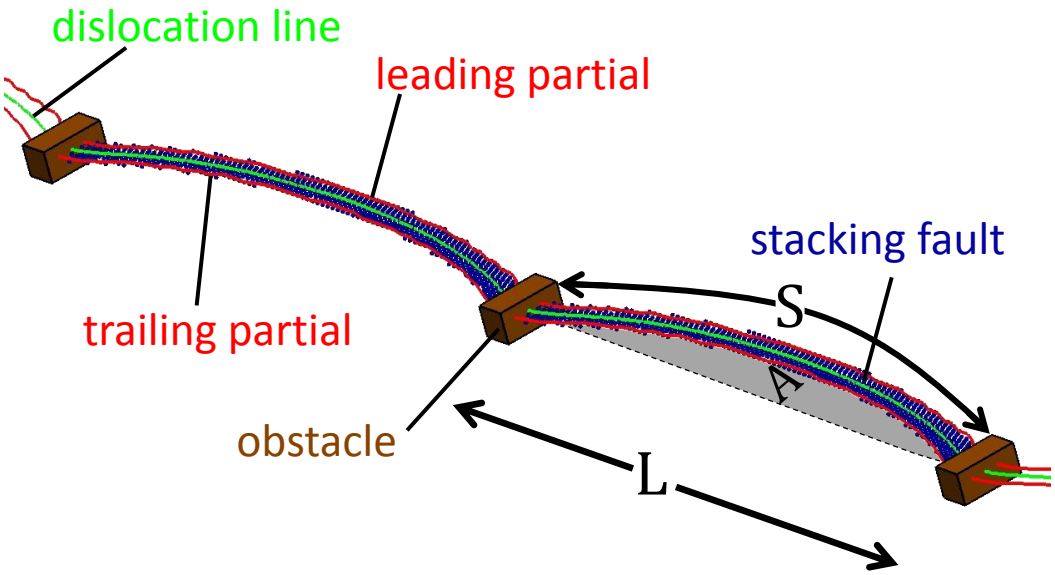

Figure 5.1: Schematic of the dislocation-obstacle bow-out configuration. The simulation cell is periodic along the line direction with length L and pinned by a periodic array of obstacles. Under a homogeneous shear stress or strain, the dislocation bows out into some equilibrium shape having contour length S and swept-out area A. In fcc materials, the full dislocation dissociates into two Shockely partial dislocations (red) with a stacking fault (blue) in between; the averaged smoothed dislocation line (green) determines S and A relative to the initial straight dislocation.

$\leq \Gamma \leq 1$ eV/Å[14, 23, 121, 140]. Since the CRSS τ_c is directly proportional to Γ, per eq. 5.2 above, this range of estimates suggests an order-of-magnitude uncertainty in the CRSS in a given material system, which is obviously unacceptable for guiding the design of new materials.

In this paper, we report a robust and accurate atomic-level measurement of the line tension for both edge and screw dislocations in Al within the context of the small bow-out problem described above (see figure 1). We use an accurate 3D multiscale method that is devoid of spurious image forces common in finite-size MD simulations [109], and use eq. 5.3 directly to measure the line tension. We also describe carefully how an effective Peierls stress τ_P enters into the analysis so as to yield consistent results for both loading and unloading of bowed dislocations, and discuss the conditions over which consistent results can be obtained. Precise values for the line tension are then obtained that are weakly dependent on the

interatomic potential. We obtain a $ln(L)$ scaling but with a coefficient that differs somewhat from the prediction of anisotropic elasticity, and we find a ratio of $\Gamma_{screw}/\Gamma_{edge}$ that differs significantly from anisotropic elasticity predictions; these differences are attributed to fundamental features of curved atomistic dislocations that are absent from continuum elasticity theory.

The remainder of this paper is organized as follows. In Sec. 2, we review the elastic theory for line tension to set a clear background for our analysis. In Sec. 3, we describe our simulation and analysis methods. In Sec. 4, we present and discuss our results in depth. In Sec. 5, we discuss important implications of our results for both materials science applications and continuum discrete-dislocation simulations, and then summarize our major results.

5.2 Line Tension within Isotropic and Anisotropic Elasticity

The line tension has been widely studied within the elastic theory of dislocations for both isotropic [8, 135] and anisotropic [145–147] materials. Within elasticity theory, the Burgers vector displacement discontinuity is assumed to terminate abruptly at the dislocation core resulting in a local, weak divergence in the elastic energy. Analytical and numerical results for the self- and interaction-energies of discrete dislocation segments thus require the introduction of ad-hoc core-cut-offs or regularization procedures. Denoting the (singular) dislocation self-interaction cut-off radius as r_0, the elastic energy of a discrete dislocation segment may be denoted as $W_{self}(r_0)$ [8], and no additional core energy is added. Cai and coworkers [33] proposed an isotropic elastic non-singular theory that smears the core over a finite region of length r_c to eliminate the singularity and included an additional core energy E^{NS}_{core}, resulting in a discrete dislocation segment energy $W_{self}(r_c, E^{NS}_{core})$ [40]. In both theories, the *total* energy of an arbitrary dislocation configuration is computed by summing the self and interaction energies of each discrete seg-

ment ($W = \sum W_{self} + \sum W_{int}$), from which forces can then be derived and the dislocation configuration evolved in time; this is achieved within various available 3D-Discrete Dislocation codes such as `ParaDiS` [34].

Within the above theories, the line tension eq. 5.1 can be computed for various problems such as the small periodic bow-out problem of figure 1. Usually, for a given parametric geometry (triangle, sinusoid, arc of a circle, and periodic or not), the *total* energies $W(S)$ and $W(S + \delta S)$ are computed for two self-similar geometries having an incremental increase in bow-out length from S to $S + \delta S$. Following eq. 5.1 the line tension is the (*energetic*) difference between these two configurations and is computed as $\Gamma^{el} = [W(S + \delta S) - W(S)]/\delta S$ and in the limit $\delta S \to 0$ we recover eq. 5.1. Following Hirth and Lothe (1982, [8]), the line tension Γ^{el} resulting from such calculations can be written as a term linear in $ln(L)$ plus a constant which, including a general E_{core} term, yields

$$\Gamma^{el} = C_1(\phi) ln(L/b) + C_0(\phi; \frac{r_0}{b}, E_{core}) \tag{5.4}$$

where ϕ is the character angle of the initial straight dislocation and small bow-out is assumed. Both incremental geometries corresponding to S and $S + \delta S$ are thus incremental with respect to the original straight dislocation. In isotropic elasticity theory, the first term of the above equation is

$$\begin{aligned} C_1(\phi) ln(L/b) &= \left(W_{self}(\phi) + \frac{\partial^2 W_{self}(\phi)}{\partial \phi^2} \right) \\ &= \left(\frac{\mu b^2}{4\pi(1-\nu)} \right) \left(1 + \nu[\cos^2(\phi) - 2\sin^2(\phi)] \right) ln(L/b) \end{aligned} \tag{5.5}$$

The C_1 prefactor is thus well defined. The term C_0 depends on the incremental change in interaction energies ($\sum \delta W_{int}/\delta S$), which are geometry specific, and also the arbitrary (singular) cut-off parameter r_0/b and the core energy E_{core}, and can be written as [40],

$$C_0(\phi; \frac{r_0}{b}, E_{core}) = -C_1(\phi) ln(r_0/b) + C_1(\phi)(4\pi E_{core}/\mu b^2) + C_{00}(\phi) \qquad (5.6)$$

Table 5.1 shows the computed results for the $ln(L/b)$ prefactor C_1 and the constant C_0 for several similar bow-out geometries, using (singular) cut-off parameter $r_0/b = 1$ and $E_{core} = 0$ so that the quoted value coincides with C_{00}, for initially straight screw ($\phi = 0$) and edge ($\phi = 90$) dislocations. For specific numerical computations, we use the isotropic constants of the Ercolessi-Adams Al [115] interatomic potential (μ= 30.8e9, ν= 0.35) with Burgers vector b= 2.851Å . While E_{core}^{NS} itself, as implemented within `ParaDiS`, has no character dependence the term appearing within the line tension, $(C_1(\phi) \times E_{core}^{NS})$ does (see [34, 40] for further details). Also shown are the analytic results for the non-periodic small triangle bow-out of [8] and the small-amplitude sinusoidal bow-out [148], and also the computed results for NS theory with $r_c/b = e$ replacing $r_0/b = 1$. Aside from a small deviation for the NS screw case, the C_1 coefficient is the same in all of these problems and the ratio of screw to edge values is ≈ 4, as is well-known. The coefficient C_{00} differs slightly with the geometry and theory, because of the chosen cut-off and core parameters, but all cases give fairly similar results. Any additional explicit core energy can be added. Thus, elasticity theory provides a robust value for the coefficient C_1 associated with the $ln(L/b)$ scaling but, in the absence of atomistic information about the core energy, does not provide any absolute line energy or line tension.

The elastic term $C_1 ln(L/b)$ dominates for sufficiently large L, and so the C_0 term and core energy are often neglected. However, with no core energy, elasticity predicts line tension to be negative at "small" L. Since $C_0 \approx 4C_1$, the line tension is zero at $ln(L/b)$ $\sim$4 or L $\approx$16nm for b $\approx$0.3nm. Dislocation densities relevant in real materials range from from $10^{12} - 10^{15}$ /m^2, so that the typical spacing between dislocation junctions is $L \sim$ 30 - 300 nm, a range also comparable to precipitate spacings in many alloys. The core energy is therefore essential at the

Type	$C_1/\frac{\mu b^2}{4\pi(1-\nu)}$	$C_0/\frac{\mu b^2}{4\pi(1-\nu)}$
Small Triangular Bow-out		
Edge[8]	0.33	-1.31
Screw[8]	1.33	-3.51
Small-amplitude Sinusoid		
Edge	0.33	-1.32
Screw[148]	1.33	-3.54
Periodic Small Bow-out		
Elasticity		
Edge	0.33	-1.49
Screw	1.33	-4.20
Periodic Small Bow-out (NS Theory[33])		
Edge	0.33	-0.92
Screw	1.20	-4.15

Table 5.1: Line Tension (Γ^{el}) coefficients for several characteristic bow-out problems ν is taken to be 1/3, the singular cut-off parameter $r_0 = |\mathbf{b}|$, the non-singular cut-off parameter $r_c = |\mathbf{b}|e$ and $E^{NS}_{core} = 0$.

lowest relevant scales, $ln(L/b)$ ≈4 and is likely non-negligible up to $ln(L/b) \sim$ 6 corresponding to L ≈120 nm. An accurate core energy and elimination of arbitrary cut-off parameters are thus necessary to obtain a line tension value that would be accurate for many materials science applications, assuming that elasticity is otherwise valid.

Within anisotropic elasticity theory, the line energy and line tension depend not only on the character of the nominally straight dislocation but also on its orientation with respect to the lattice [146, 147]. For Al, we have computed Eq. 5.4 for both isotropy and general anisotropy (detailed in the appendix) using the full elastic stiffness tensors corresponding to the Ercolessi-Adams [115] and Mishin [149] interatomic potentials at 0K, respectively. Table 5.2 shows the $ln(L)$ prefactor C_1. Al is relatively isotropic so that the effects of anisotropy are relatively small (≤10%).

Finally, fcc dislocations dissociate into partial dislocations, so it is possible that the line tension for the full dislocation might also be considered as due to two interacting partial dislocations. Since line tension of an individual dislocation scales as b^2, it is unclear whether the line tension of two interacting partial dis-

Elasticity	Isotropic (eV/Å)	Anisotropic (eV/Å)
$\text{Edge}^{\text{Ercolessi-Adams}}$	0.060	0.065
$\text{Edge}^{\text{Mishin}}$	0.052	0.055
$\text{Screw}^{\text{Ercolessi-Adams}}$	0.258	0.266
$\text{Screw}^{\text{Mishin}}$	0.238	0.244
MD (guide to the eye)		
$\text{Edge}^{\text{atom, Ercolessi-Adams}}$		0.072
$\text{Screw}^{\text{atom, Ercolessi-Adams}}$		0.139

Table 5.2: $\ln(L)$ prefactor, C_1, of the dislocation line tension Γ for the Ercolessi-Adams [115] and Mishin [149] interatomic potentials, using both isotropic and anisotropic elasticity. Also shown is the value obtained and plotted (^{atom}, dashed in figure 5.5) from the present atomistic study for each case.

locations with burgers vectors $b_p = b\sqrt{3}/3$ is equal to that of a full dislocation of burgers vector b. This problem is analytically tractable within isotropic elasticity, and the result shows that the line tension for two partial dislocations depends on the partial spacing d divided by the obstacle spacing L. For partial dislocations in Al, $d \sim 1$ nm and $d/L << 1$ for relevant dislocation lengths of $L > 30$ nm, so that the line tension is essentially equal to that of the full undissociated ($d = 0$) dislocation.

5.3 Molecular Dynamics Simulation and Analysis to Compute Line Tension

5.3.1 MD Simulation Details

Low temperature (1K) Molecular Dynamics (MD) simulations were performed using a multiscale method that couples a small atomistic region ($\sim$ 1 million atoms) to a large surrounding continuum region. The method uses the standard large-scale parallel atomistic simulation software `LAMMPS` [12] in conjunction with a parallelized finite element scheme developed for large 3D multiscale simulations [109]. The coupling between atomistic and continuum regions creates zero errors when dislocations are more than $\approx$ 1 nm from the atom/continuum interface,

and the very large surrounding continuum domain eliminates all spurious image forces that would otherwise arise due to interactions of the curved dislocations with the outer boundaries of the sample [144]. Thus, no corrections for boundary conditions are needed.

The simulation cell is a single crystal fcc sample. Different fcc lattice orientations are used for studies involving edge or screw dislocations, but always maintaining the dislocation line along the periodic Y direction. For all cases, Z =[1 1 1] is normal to the dislocation glide plane, while X and Y (glide and line) directions are [1 $\bar{1}$ 0] [1 1 $\bar{2}$] and [1 1 $\bar{2}$] [1 $\bar{1}$ 0] for edge and screw dislocations, respectively. The atomistic portion of the much-larger simulation cell has dimensions of X $\approx$ 18 nm, Y $\approx$ 13-52 nm (varying dislocation line length), and Z $\approx$ 10 nm. The Al interatomic potentials developed by Ercolessi and Adams [115] and by Mishin *et al* [149] describe the nonlinear interactions between atoms. We insert a single initially-straight dislocation into the atomistic region by displacing atoms and nodes of the multiscale model according to the singular Volterra solution and external applied boundary conditions as specified in [109]. The inner nodes and atoms are allowed to relax using explicit dynamics at 1 K, during which the singular dislocation core dissociates into two partials. A damping stadium method is used to control the temperature in the atomistic region. The obstacles are then created by identifying small cubic volumes of $\sim$1 nm^3 encompassing the dislocation core that are then held fixed during subsequent simulations. Spurious stress fields created by these rigid obstacles scale with the applied load and can be approximated to leading order as $\tau_{obs} < \frac{\tau_{app}}{32}\left(\frac{a}{R}\right)^3$, where $a = 1$ nm is the characteristic obstacle length and R is the distance from the obstacle. For all simulation results reported here, τ_{obs}(R>1.5nm) < 3 MPa and we consider its influence on bowing out of the dislocation over scales of ≥ 10 nm to be negligible. A homogeneous resolved shear stress τ_{app} (τ_{xz} for the edge, τ_{yz} for the screw) is applied using a homogeneous shear strain ϵ and the appropriate shear modulus $\mu = (C_{44} + C_{11} - C_{12})/3$ so that $\tau_{app} = \mu\epsilon$. Upon loading, the (pinned) dislocation bows out. Inertial effects

[14] are avoided by using small loading increments of $\Delta\tau_{app} \approx 5$ MPa to obtain essentially quasi-static equillibrium shapes. The dislocation structure (partial dislocations, stacking fault) were detected using common neighbor analysis (CNA) and `AtomEye` [150] for visualization.

5.3.2 Configurational Analysis

The outcome of the MD simulation for a given L and τ_{app} is a bowed-out dislocation configuration. Evaluation of the configurational derivative (i.e. $\mathrm{d}A/\mathrm{d}S$) appearing in eq. 5.3 first requires measurement of the total length of dislocation line, S, and the area enclosed by the bow-out, A. Using a moving average procedure, each partial dislocation is detected using CNA and its line is divided into discrete segments (shown in red in figure 5.1). The two partial dislocations are then averaged to create a single, continuous curve (shown in green in figure 5.1). The line length S is the sum of the lengths of the discrete segments and the area A is calculated using Simpsons rule. There is no assumption about the overall shape of the dislocation. We have verified that the stacking fault area is unchanged during the bowing-out process, although there are small differences in the partial separation of $\pm b_p$ along the dislocation line associated with slightly different lateral positions of CNA-visualized "kinks" along the two partials.

Evaluation of the derivative dA/dS is difficult to perform accurately by purely numerical means based on a sequence of bow-out configurations. We thus develop a general analytic model to assist with this differentiation, as follows. We assume that the dislocation bows-out into a curved geometry with a non-constant radius (as discussed and detailed in [151]), which is expected due to the difference in line tension for screw and edge dislocations. There is no analytic closed-form relationship between the length S and area A associated with a general arc having a chord length L. However, for the small bow-out problem of interest, where L is much less than the minimum radius (i.e. $S/L \approx 1$), the relationship between A and S is almost independent of the non-constant radius and thus essentially equal

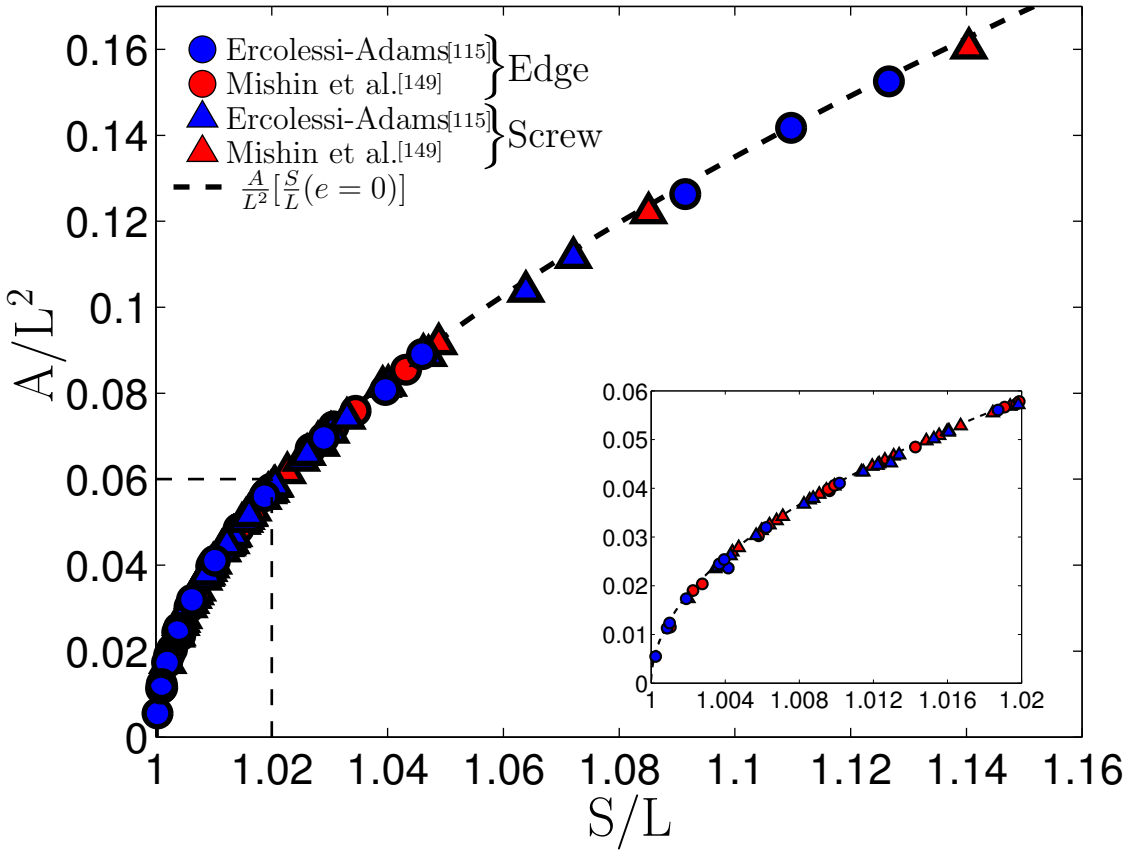

Figure 5.2: Normalized area enclosed by the bow-out ($\frac{A}{L^2}$) versus normalized line length ($\frac{S}{L}$) for each bow-out configuration. Also shown (- -) is the relationship between A and S used in calculating R. Inset: Normalized area enclosed by the bow-out versus normalized line length for $\frac{A}{L^2}$ <0.06 and $\frac{S}{L}$ ≤1.02

to that of a circular arc. In the limit of an ellipse (with eccentricity, e), it can be readily verified that for an elliptical arc and a circular arc of equal arc length S and bisected length L, the difference in area A is negligibly small,

$$(A[S(e)] - A[S(e=0)])/L^2 \approx \mathcal{O}\left(\frac{eL}{R_{maj}}\right)^2 \tag{5.7}$$

Using the circle radius R as a parametric variable, the area A versus arc length S can be solved by eliminating R from the two equations

$$S = 2R\sin^{-1}(\frac{L}{2R}), \quad A = \left(R^2\sin^{-1}(\frac{L}{2R}) - \frac{RL}{2}\sqrt{1-\frac{L^2}{4R^2}}\right) \tag{5.8}$$

Figure 5.2 shows the resulting relationship between A/L^2 and S/L, the ac-

curacy of which we have also validated with explicit numerical computations on ellipses. Also shown in figure 5.2 are our simulation results for both edge and screw dislocations for a range of L and a range of τ_{app}. All of our data fall on the analytic line of A/L^2 versus S/L, indicating that the measured shapes (whatever they may be) are consistent with elliptical arcs in terms of the relationship between S/L and A/L^2, despite not having actually quantified the shapes. For any individual data point lying on this "universal" curve of A/L^2 versus S/L, we can accurately calculate the derivative dA/dS using the universal curve at the given value of A and S. There is then no need for finite-difference derivatives between numerically-simulated configurations that would be inaccurate due to small numerical noise in our measurements of A and S.

5.3.3 Effective Peierls stress

Due to the discrete atomistic lattice, dislocations encounter a periodic resistance to motion with a wavelength of b that is the Peierls stress τ_P. The influence of τ_P must be considered when evaluating the line tension. The line tension is primarily a continuum concept applied to a smooth continuous dislocation line. Within a similar continuum framework, the discrete features giving rise to τ_P at the scale of b are neglected in favor of a continuous resistance of τ_P acting at all points along a dislocation line to oppose motion. Thus, under a true applied stress τ_{app}, the effective applied stress, in the sense of a Peach-Koehler [41] force, $\tau_{app,eff}$ acting on a straight dislocation is taken as

$$\tau_{app,eff} = \tau_{app} - sgn(\Delta\tau_{app})\tau_P \tag{5.9}$$

where $\Delta\tau_{app}$ denotes the difference in applied load between the current and the previous loading increment and the *sgn* term ensures that the Peierls stress opposes the dislocation motion in the direction of $\Delta\tau_{app}$. The Peierls stress thus leads to a hysteresis in the response of a dislocation as it glides forward and backward. The

implication for dislocation bow-out is that during the bowing out process occuring during loading, the effective applied stress should correspond to $\tau_{app,eff} = \tau_{app} - \tau_P$. If, after some amount of bow-out, the applied load is then reduced, the dislocation should retreat but the configurations should correspond to an effective applied stress $\tau_{app,eff} = \tau_{app} + \tau_P$ since the Peierls stress will oppose the retreating motion. Therefore, at any position, the difference in applied stresses required to move the dislocation forward and to move the dislocation backward is $2\tau_P$. In computing the line tension, the appropriate $\tau_{app,eff}$ must be used along with the dislocation configuration (and associated dA/dS).

The Peierls stress τ_P is calculated atomistically for straight dislocations as the applied stress needed to initiate dislocation flow in an infinite material, and depends on the dislocation character ϕ. The Peierls stresses for the edge and screw dislocations for the Ercolessi-Adams and Mishin potentials are shown in table 5.3, as measured at both $T = 0K$ and $T = 1K$ with the differences being small. As is well-known, τ_P for the Al edge is quite small, ~ 2 MPa, while τ_P for the screw is non-negligible being on the scale of applied stresses needed to bow-out dislocations and varies between the two potentials. Focusing on the screw dislocation, if these values of τ_P for the perfectly straight dislocation are applied to the bow-out problem, then at any given configuration the applied stress to move a bow-out screw forward should be larger than the stress to retract the bowed-out screw by either 18 MPa or 60 MPa, for the EA and Mishin cases at $T = 1K$ respectively. Simulations of the motion of bowed-out screw dislocations show no such large hysteresis. Figure 5.3 shows loading and unloading configurations corresponding to the same applied load τ_{app}, for several values, achieved during loading up to 168 MPa and then unloading, in small load increments. The differences in configurations of the dislocation during loading and unloading at the same applied stress τ_{app} are nearly the same, differing by only $\sim 2b$ at the peak of the bow-out. Although the initially straight dislocation requires an applied load greater than τ_P to begin bowing, the dislocation bowing for moderately-curved dislocations does

	$\tau_{Peierls,0K}$ (MPa)	$\tau_{Peierls,1K}$ (MPa)	$\tau_{P,eff}$ (MPa)
Edge$^{\text{Ercolessi-Adams}}$	2.4	<2	0.25
Edge$^{\text{Mishin}}$	2	<2	0.1
Screw$^{\text{Ercolessi-Adams}}$	14	9	0.6
Screw$^{\text{Mishin}}$	33	30	3.6

Table 5.3: Measured Peierls stress of straight and curved dislocations. The $\tau_{P,eff}$ values are taken directly from the converged values of the atomistic simulations with sufficiently high kink density (see text and figure 5.4), and are used in the subsequent calculation of Γ in figure 5.5.

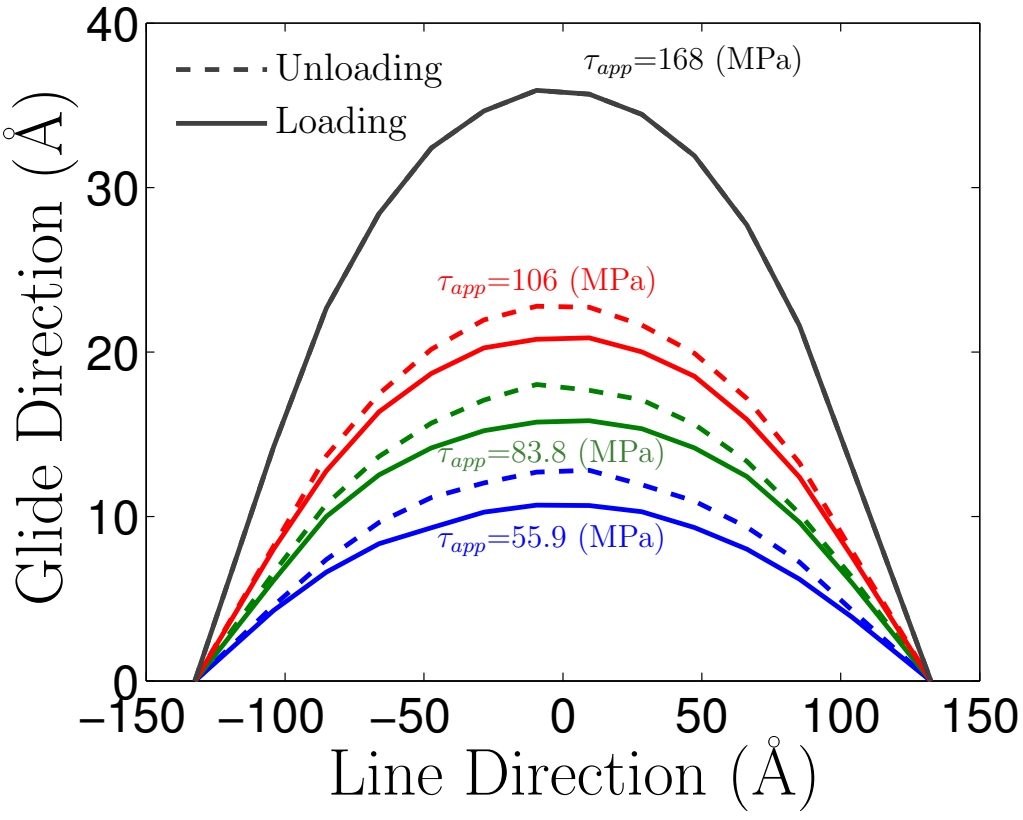

Figure 5.3: Hysteresis in the bow-out of the Mishin [149] initially screw dislocation at three applied loads. The amount of bow-out for loading (solid, $\Delta\tau_{app} > 0$) is only slightly less than the amount of bow-out for unloading (dashed, $\Delta\tau_{app} < 0$). Also shown is the configuration at the peak load of $\tau_{app} = 168$ MPa from which point the unloading commenced.

not correspond or conform to the behavior predicted using eq. 5.9 with τ_P for the straight dislocation. In other words, the measured τ_P for a straight dislocation cannot be used as the Peierls stress for a curved dislocation.

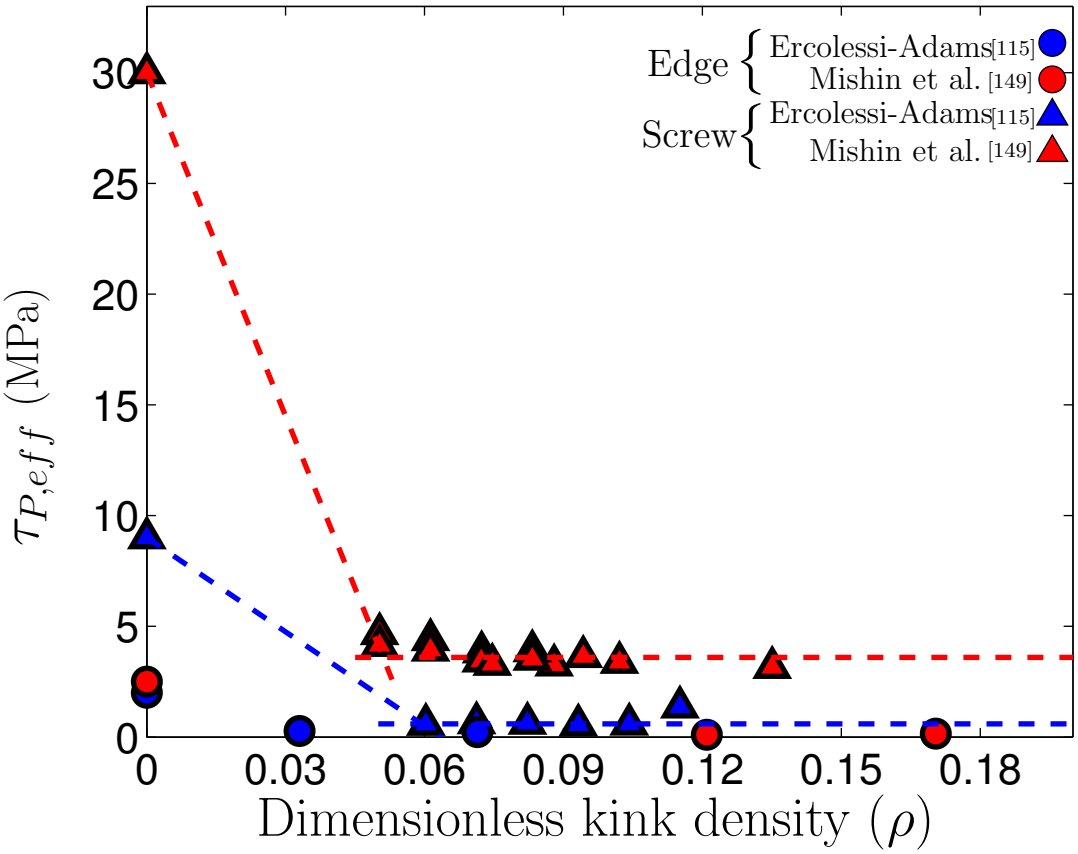

Figure 5.4: Effective Peierls stress, $\tau_{P,eff}$, versus dimensionless kink density ($\rho \propto h/L$) in the bowed-out configuration, for both nominally edge and screw dislocations. The dimensionless kink density is related to the peak bow-out distance h as $\rho = 2h/L$ and $2\sqrt{3}h/3L$ for edge and screw, respectively. The converged $\tau_{P,eff}$ values for both the Ercolessi-Adams and Mishin nominally screw dislocations are shown as blue and red dashed lines respectively at $\tau_{P,eff} = 0.6$ and 3.6 MPa, and are tabulated in table 5.3 along with those for straight dislocations.

The loading and unloading configurations are slightly different, with the unloading configuration always ahead of the loading configuration (by $\sim 2b$) at the same applied stress. This indicates that there is some *effective* Peierls stress $\tau_{P,eff}$ acting on the curved dislocations that is much lower than the Peierls stress acting on straight dislocations (τ_P). To deduce the value of $\tau_{P,eff}$ for such a continuum curved dislocation, we assume that $\tau_{P,eff}$ acts as a continuum Peierls stress, similar to τ_P, to oppose the dislocation motion according to eq. 5.9. For any pair of loading and unloading bow-out configurations (A_l, S_l, R_l) and (A_u, S_u, R_u) with the associated parametric variable, R (from eqs. 5.8) measured at the *same*

applied stress, we assume that the line tension Γ is the same for the two configurations. The two configurations must then be related through eq. 5.3 and eq. 5.9, leading to a system of two linear equations that when solved for $\tau_{P,eff}$ is

$$\tau_{P,eff} = \tau_{app} \left(\frac{1 - \frac{R_u}{R_l}}{1 + \frac{R_u}{R_l}} \right) \tag{5.10}$$

Inserting the *effective* Peierls stress (eq. 5.10) applicable to curved dislocations in to eq. 5.9 leads to an effective applied stress for the bow-out dislocations considered in this study:

$$\tau_{app,eff} = \tau_{app} \left(1 - sgn(\Delta\tau_{app}) \left(\frac{1 - \frac{R_u}{R_l}}{1 + \frac{R_u}{R_l}} \right) \right) \tag{5.11}$$

This definition of $\tau_{P,eff}$ enforces equality of both Γ, and $\tau_{app,eff}$ for two configurations at the same applied load with the same spacing between obstacles (L), independent of $sgn(\Delta\tau_{app})$. The computed $\tau_{P,eff}$ for a number of loading/unloading configurations (various L and τ_{app}), for both edge and screw dislocations, is shown in figure 5.4. In figure 5.4, $\tau_{P,eff}$ is shown versus the dimensionless kink density, $\rho^{edge} = 2h/L$ or $\rho^{screw} = 2\sqrt{3}h/3L$, required to achieve the peak bow-out h in each configuration. Each data point is completely independent. For dislocations with a low kink density (small bow-out relative to the dislocation length), $\rho < 0.05$, the discrete nature of the dislocation bow-out makes a smooth continuum description inappropriate. This is manifested in, among other ways, an inability to measure an effective Peierls stress for very low kink densities $\rho \leq 0.05$, and so no data is shown. However, for larger bow-out or modestly-curved dislocations, $\rho \geq 0.05$, an effective Peierls stress $\tau_{P,eff} << \tau_P$ emerges that is nearly independent of configuration (independent of ρ, L, τ_{app}) and thus represents an appropriate "*continuum-level*" Peierls stress for the curved dislocation. For the edge dislocations, which have small τ_P, the effective $\tau_{P,eff}$ is nearly zero for both interatomic potentials. For the screw dislocations, which have larger τ_P, the effective $\tau_{P,eff}$ is small, typically $\sim$ 0.5 MPa for the EA potential and $\sim$ 3.6 MPa for the Mishin potential. The

consistency of the deduced value of $\tau_{P,eff}$ across a range of configurations, for each initial character and interatomic potential, supports the notion that a single value of continuum (effective) Peierls stress can be considered to operate for moderately curved dislocations. These effective values are appropriate at the temperature of our simulations, $T = 1K$ and are tabulated in the final column of table 5.3.

5.4 Results

In the previous section, we presented the essential pieces of the simulation and analysis needed to compute Γ. For an initial length L, we have measured A/L^2 and S/L at various values of τ_{app} (figure 5.2). We have also deduced the effective applied stress $\tau_{app,eff} = \tau_{app} \pm \tau_{P,eff}$ acting on the bowed-out dislocation in the presence of the effective Peierls stress (figure 5.4). For each configuration, our analytic analysis for the geometry of A/L^2 versus S/L yields the value of dA/dS necessary to obtain Γ. In light of the predictions of elasticity theory (eq. 5.4), we present the computed line tension Γ versus $ln(L/b)$, as shown in figure 5.5 for the two interatomic potentials [115, 149], three obstacle spacings L, and initially edge and screw dislocations. For moderate bow-outs $\rho \geq 0.05$ where the continuum description is valid, the results are independent of the amount of bow-out to leading order in h/L (e.g. S, A, and/or h) and therefore the derived line tension is a function primarily of obstacle spacing (L) and dislocation character (ϕ). The atomistic computation of the line tension (Γ) is the first main result of this paper.

The line tension Γ_{edge} for the edge dislocation is quite consistent between the two potentials, with the Mishin potential yielding slightly smaller values, ≈ -0.05 eV/Å. Both potentials show a good linear scaling in $ln(L/b)$ with similar slopes. The line tension for the screw dislocation is larger than that for the edge, as expected, and both potentials predict comparable values for Γ_{screw}, with the Mishin potential greater by ≈ 0.05 eV/Å at the smallest and largest sizes, with twice that difference at the intermediate length $L/b \approx 90$. The results for the EA potential

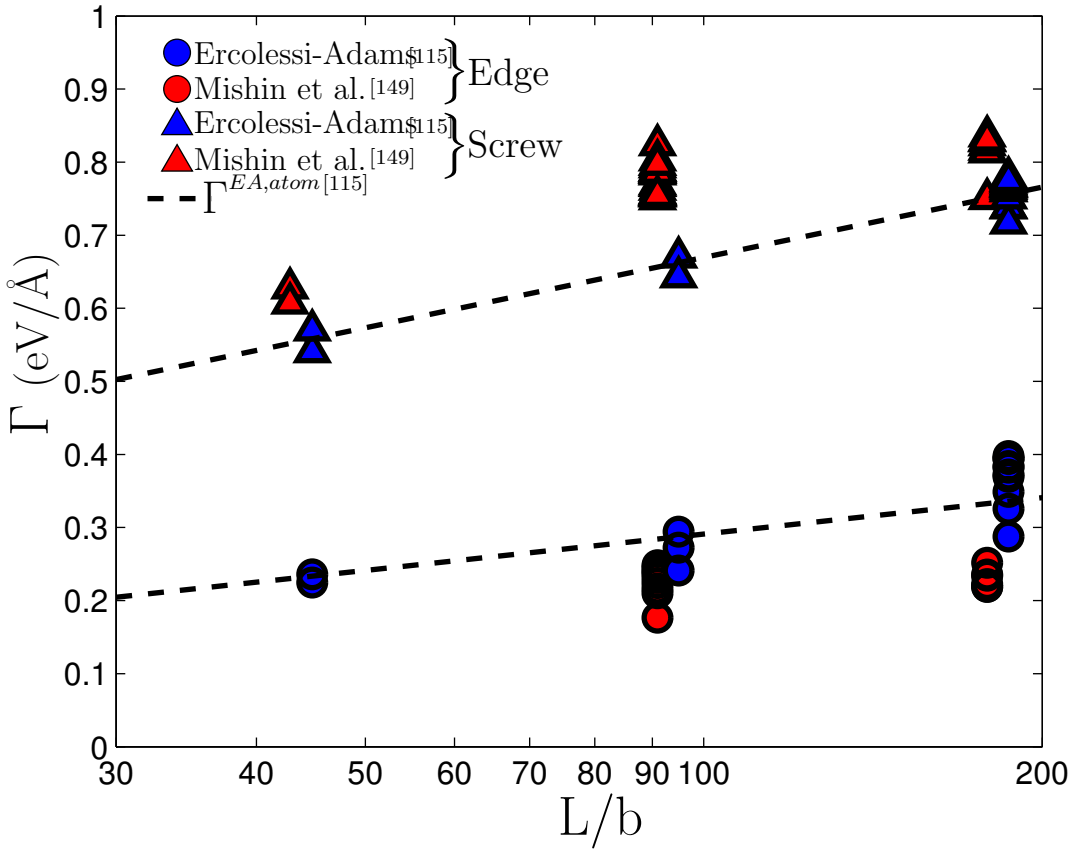

Figure 5.5: Γ versus $ln(L/b)$ for the interatomic potentials of Ercolessi-Adams [115] (blue) and Mishin [149] (red) for nominally edge (circles) and screw (triangles) dislocations. The data collapses well, indicating the robustness of the method. Both data sets have been shifted by ~ 2 Burgers vectors from their true L/b values to improve clarity of the figure. Dashed lines show fits to the form $\Gamma = C_1^{atom} ln(L/b) + E_{core}^{atom}$ for the Ercolessi-Adams potential, yielding $\Gamma_{edge}^{EA,atom}$=0.072ln(L/b)-0.04 (eV/Å) and $\Gamma_{screw}^{EA,atom}$=0.139ln(L/b)+0.03 (eV/Å).

again show a good linear scaling in $ln(L/b)$ while the Mishin potential results are inconclusive about a $ln(L/b)$ scaling. The Mishin screw has a rather high Peierls stress for the straight dislocation, suggesting that the potential may have some inaccurate features that are not easily identifiable but are reflected in the Peierls stress and also influence the bowing and the line tension. Here, we thus focus attention on the consistent EA results, while retaining the knowledge that the general magnitudes of Γ when comparing the EA and Mishin potentials are quite comparable for both edge and screw, over this range of L. Our results for the atomistic line tension for the EA potential can be fit to the form of elasticity plus

a core energy term,

$$\Gamma^{atom} = C_1^{atom} ln(L/b) + C_0^{atom} \tag{5.12}$$

For the edge dislocation, we obtain $C_1^{atom} = 0.072$ eV/Å and $C_0^{atom} = -0.04$ eV/Å . For the screw dislocation, we obtain $C_1^{atom} = 0.139$ eV/Å and $C_0^{atom} = +0.03$ eV/Å .

The variations in Γ for one potential at one length L reflect the level of accuracy of the measurements of A, S, and $\tau_{P,eff}$. Numerical measurements of A versus S for various L for perfect ellipses with moderate ellipticity $e < 0.7$ show near-perfect agreement with the analytic result for the circle $A[S(e = 0)]$ curve. Thus, deviations in our results are due to the fact that the dislocations are not smooth lines, which leads to associated small numerical errors in general. For very small bow-outs, both the evolution of the bow-out shape (i.e. dA/dS) and the effective Peierls stress are ill-defined and so our analyses and results are restricted to the domain $\rho > 0.05$. In this regime, a continuous smooth bow-out description is applicable, a configuration-independent effective Peierls stress can be obtained (see figure 5.4), and a reliable Γ computed.

5.5 Discussion

We start with discussion of the C_1 coefficient, which has an unambiguous value within elasticity theory. For the edge, $C_1^{atom} \approx C_1^{aniso}$, within the uncertainty of our measurements. For the screw, however, $C_1^{atom} << C_1^{aniso}$, differing by a factor of $C_1^{aniso}/C_1^{atom} \approx 2$, which is not negligible. The C_1 term arises in elasticity theory due to the change in self-energy (due to both rotation, and elongation) of each infinitesimal segment as the dislocation bows-out. It therefore would seem sensible that elasticity should apply. Our failure to match anisotropic elasticity might cast doubt on the validity of the atomistic simulation and results but the results are very robust and our final values for Γ are very consistent across different amounts

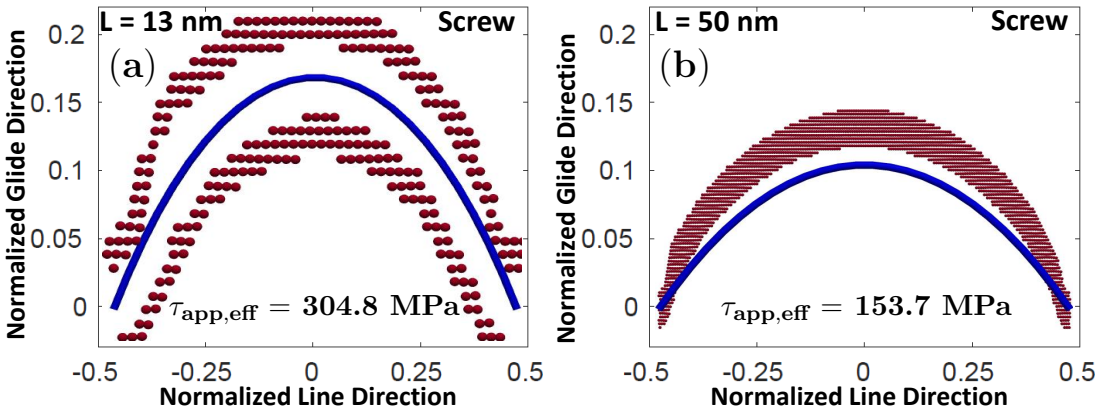

Figure 5.6: Configuration of two bowed-out dislocations of lengths L=12.5 nm (a, left) and L=50 nm (b, right) for a nominally straight, screw dislocation, as computed via MD (red) and via DD (blue). The MD computations were performed with the Ercolessi-Adams [115] interatomic potential while the DD bow-outs were computed using a single core cutoff parameter (r_0) which was selected to *fit* the small (a, left) screw bow-out. In both comparisons the *effective* applied stress ($\tau_{app,eff}$) extracted from the MD simulations was used in computing the DD configurations and is shown within each figure. The large (right) bow-out as computed via MD and DD is not in good agreement because of the discrepancy in the $ln(L/b)$ prefactor, C_1 (i.e. $C_1^{aniso} \neq C_1^{atom}$) for the nominally screw dislocation (see table 5.2). Central atoms have been removed from visualization for the small bow-out (a, left) to improve clarity.

of bow-out and applied stress. Furthermore, the bowed-out atomistic dislocation is not a smooth continuous line in the sense assumed within the elastic theory or within standard discrete dislocation modeling [8]. Instead the atomistic dislocation consists of a displacement discontinuity profile along the slip-plane which evolves as the dislocation bows-out in response to the applied stress and to the underlying landscape of the generalized stacking fault energy surface. The long-ranged elastic fields arise from the gradient of the displacement discontinuity profile along the slip plane within the dislocation core. Here, we are studying evolving curved dislocations, complete with Shockley partial dislocations separated by a stacking fault, that might also be characterized in terms of dislocation segments and *kinks*, and so it is perhaps surprising that a $ln(L/b)$ scaling emerges at all. In fact, we have performed DD computations of Γ by representing the bowed-out dislocation by a discrete set of dislocation segments with each segment having a character

chosen from only a few high symmetry orientations (0, 30, 60, 90) similar in spirit to those examined by Kang et al. [152]. The resulting C_1 coefficient is very sensitive to both the spatial distribution of the kinks and the assumed character angles of the *kinks*, with the screw dislocation being particularly sensitive. We will report on more details of this type of analyses in the future, but these studies are generally consistent with the differences between *smooth* continuum elasticity and our atomistic results. Moreover, for a self-similar geometry, i.e. fixed ratio of maximum bow-out h to length L, a longer length simply has more kinks or, equivalently, the kink density depends only on h/L and not L, and hence kink-kink interactions would not diminish in importance for larger L. The difference between atomistic and elasticity $ln(L/b)$ scaling is the second main result of this paper.

The difference in bow-out due to the mismatched $ln(L)$ coefficient ($C_1^{iso}/C_1^{atom} \approx 2$) for the nominally screw dislocation can be directly illustrated. Assuming no core energy contribution, eq. 5.4 and eq. 5.6 can be rearranged to solve for the core cut-off parameter (r_0) as a function of our *measured* line tension for the L=12.5 nm Ercolessi-Adams [115] (screw) bow-out and the coefficients given in table 5.1. Using a measured line tension of Γ^{atom}(L=12.5 nm) = 0.57 eV/Å for the small, periodic bow-out the core cut-off parameter when equating $\Gamma^{el} = \Gamma^{atom}$ at L=12.5 nm is:

$$\begin{aligned} r_0 &= (L)\, e^{(C_{00}-\Gamma^{atom})/C_1} \\ &\approx 0.35b \end{aligned} \tag{5.13}$$

By approximating the bow-out as a circular arc [8] and using the effective applied shear stress ($\tau_{app,eff}$) computed via eq. 5.11 the radius of the bow-out, not to be confused with the parametric variable used in Sec. 5.3.2, then follows as,

$$R = \frac{\Gamma^{el}\big|_{r_0=0.35b}}{\tau_{app,eff} b} \tag{5.14}$$

Figure 5.6 shows a screw bow-out for the Ercolessi-Adams [115] screw dislocation at both L=12.5 nm (where we have fit elasticity) and at L=50 nm for both our atomistic simulations as well as our computed DD bow-outs. There is excellent agreement between our atomistic calculation and our isotropic elastic calculation for the L=12.5 nm bow-out *only*. In contrast, there is significant deviation for the larger (L=50 nm) bow-out which ultimately shows poor agreement, where the elastic dislocation has less bow-out than the atomistic dislocation. This is because elasticity predicts a stronger $ln(L)$ scaling than our atomistic results and hence an artificially high line tension creating an artifically small extent of bow-out ($\Gamma h \approx$ constant). These direct comparisons of configurations are thus entirely consistent with the differences in line tension. The inability to match atomistic configurations using standard discrete-dislocation modeling techniques, even after fitting parameters to match one atomistic case, is the third main result of this paper.

Finally, we address the range of line tension (Γ) values published previously in the literature. The combination of processing and post-processing schemes employed here in computing Γ are far beyond those in any of the earlier attempts [14, 85, 87, 121, 139–142]. First, spurious effects are caused by finite simulation volumes because the image stresses on a bowing-out dislocation scale linearly with the amount of bow-out [144], leading to error in τ_{app} and thus Γ. Shenoy et al. [140] estimated the image stress and corrected their calculated line tension but the final results remain qualitative. The use of large stress increments ($\Delta\tau_{app}$) is computationally efficient but the existence of a Peierls energy barrier in conjunction with inertial effects [14] of the gliding dislocation creates a continuous range of metastable equilibrium configurations; we have observed this explicitly in our simulations and have used sufficiently small load increments to avoid such issues. Here, we find that it is essential to introduce an *effective* Peierls stress for curved dislocations. Thus, neglecting the Peierls stress (e.g. [140]) or assuming it is equal to the value for the straight dislocation (e.g. [116]) both introduce significant er-

rors. For the Al edge, the effective Peierls stress is small and so in this particular case it can be safely neglected. The line tension is a configurational force acting on a smooth, continuous bow-out (e.g. [8]) and is not the line energy, as used in refs. [14, 121]. It is also important to account for ellipticity, which has been neglected in all atomic scale studies of dislocations. Finally, the concept of line tension, as applied to a smooth, continuous bow-out, is inapplicable for very small bow-outs (kink density $\rho <\sim 0.05$; Figure 5.4), and results in this domain are not consistent [85].

5.6 Summary

We have reported accurate, atomically-resolved measurements of the dislocation line tension for the periodic bow-out of both initially edge and screw dislocations, using two distinct interatomic potentials. This has been achieved with the use of a unique 3D multiscale method that eliminates all spurious image forces [109] and with the development of new analysis methods. We have also introduced, out of necessity, the concept of an *effective* Peierls stress applicable to curved, bow-out dislocation configurations to accurately account for the measured forward and reverse motion of curved dislocations. We have found that, up to lengths of $L = 50$ nm, the $ln(L/b)$ dependence of the dislocation line tension for the screw is much weaker than that predicted by elasticity theory, and weakly dependent on the interatomic potential. With all of these results and direct comparisons between atomistic and continuum simulations, we have shown that there are inherent limits to the ability of continuum-level dislocation models to quantitatively reproduce atomistic simulations of dislocation behavior. The present results can be used (i) to best-fit continuum dislocation parameters in existing models, (ii) to provide reference configurations for future continuum methods to match, and (iii) to provide quantitative numerical values of the line tension for use in analytic theories of plasticity phenomena.

5.7 Appendix

The line tension Γ^{el} of a dislocation within anisotropic elasticity depends on both the character angle ϕ of the nominally straight dislocation and a second orientation vector with respect to the cardinal crystal axes. For convenience we have chosen the unit vectors $\mathbf{n} = [111]/\sqrt{3}$ to represent the glide plane normal, and $\mathbf{t}$ to represent the dislocation line direction, so $\mathbf{b} \cdot \mathbf{t} = |\mathbf{b}| \cos(\phi)$. We may then define a third, mutually perpendicular vector as

$$\mathbf{m} = \mathbf{n} \times \mathbf{t} \tag{5.15}$$

Following along the lines of Barnett and coworkers [146, 147] and more recently Aubry *et al* [145] the dislocation line energy (per unit length) scales with $ln(L)$ as

$$W_{self}(\mathbf{t}(\phi), \mathbf{n}) = \mathbf{b} \cdot \mathbf{B}(\mathbf{t}, \mathbf{n}) \cdot \mathbf{b} \ln(L), \tag{5.16}$$

where the second-order tensor $\mathbf{B}$ is defined as

$$\begin{aligned} \mathbf{B}(\mathbf{t}, \mathbf{n}) = & \frac{1}{8\pi} (\mathbf{m} \otimes \mathbf{m} + \mathbf{n} \otimes \mathbf{n}) : \mathbf{C} \\ & - \frac{1}{4\pi^2} \int_0^{\pi} (\mathbf{M} \cdot \mathbf{C} \cdot \mathbf{N}) \cdot (\mathbf{N} \cdot \mathbf{C} \cdot \mathbf{N})^* \cdot (\mathbf{N} \cdot \mathbf{C} \cdot \mathbf{M}) \mathrm{d}\eta \end{aligned} \tag{5.17}$$

with $\mathbf{C}$ denoting the stiffness tensor, $(\mathbf{N} \cdot \mathbf{C} \cdot \mathbf{N})^*$ defined as the inverse of $(\mathbf{N} \cdot \mathbf{C} \cdot \mathbf{N})$ satisfying $(\mathbf{N} \cdot \mathbf{C} \cdot \mathbf{N})^* \cdot (\mathbf{N} \cdot \mathbf{C} \cdot \mathbf{N}) = \mathbf{I}$ and the vector(s) over which the integral is taken, $\mathbf{M}$ and its derivative $\mathbf{N}$ defined conveniently in terms of a single angle, η as

$$\mathbf{M} = \mathbf{m} \cos(\eta) + \mathbf{n} \sin(\eta) \tag{5.18}$$

$$\mathbf{N} = -\mathbf{m} \sin(\eta) + \mathbf{n} \cos(\eta) \tag{5.19}$$

The integral in $\mathbf{B}$, as noted by Aubry *et al* [145], involves the ratio of a fourth-

order polynomial to a sixth-order polynomial and so is analytically insoluble. Any numerical integration technique however, such as Simpson's rule will suffice. Given $W_{self}(\mathbf{t}(\phi), \mathbf{n})$, the line tension prefactor may be computed numerically as

$$C_1(\phi, \mathbf{n}) \ln(L) = \left(W_{self}(\mathbf{t}(\phi), \mathbf{n}) + \frac{\partial^2 W_{self}(\mathbf{t}(\phi), \mathbf{n})}{\partial \phi^2} \right) \tag{5.20}$$

Chapter 6

Summary and Conclusions

Within this thesis we have motivated research in to metals and alloys by the demands of a variety of industries. We have also introduced the dislocation as a dominant mechanism to explain many of the differences observed experimentally between alloys and processing-mechanical property relationships. We started by reviewing a methodology to simulate elastic dislocations via 3d-Discrete Dislocation Dynamics in chapter 2. We then looked at three examples where the macroscopic measureable mechanical properties, such as *strength* were dependent on additional (small) lengths inherent to the geometry which markedly influenced the flow properties of dislocation(s). We have examined the role of large stress gradients (in chapter 3) where the magnitude of the stress gradient determines the magnitude of the strengthening and hardening effect. We have examined a dimensionality effect in the form of a *thin film* type of problem where the *width* of the film effectively determines the strengthening effect in chapter 4. Finally, in chapter 5 we have examined the coefficient associated with a size effect generated by a dislocation interacting with rows of obstacles i.e. the *line tension* (Γ).

In chapter 3, we observed the operation of a single FrankRead (FR) source in the presence of a spatial stress gradient using 3D discrete-dislocation dynamics (DDD) simulations and analytic models. We found that under a sufficiently large stress gradient, the FR source shows a new stable configuration controlled by the

low-stress region of the graded stress field. Successive emissions from the source generate a growing dislocation pile-up that exerts an increasing back stress on the source, leading to hardening. The operation of the FR source in the gradient field was indeed well-approximated by a single critical stress at a unique critical location (x_c, τ_c), allowing for the development of an analytic model of the source operation. These results were applied to rationalize the size-scaling of strength measured in simulations of single-crystal beam bending using DDD and in experiments on bending of single-crystal cantilever beams. This chapter demonstrated that size effects in plasticity emerge naturally from the mechanics of dislocation sources operating within a stress gradient, and in this case the relevant material length scale is the length of the FR source.

In chapter 4 we examined molecular dynamics simulations of dislocation/obstacle interactions which are enhancing our physical understanding of plasticity. However, despite increasing computational power, the interaction between simulation cell boundaries and the long ranged fields of dislocations make spurious image effects inevitable. By examining these image effects in detail we provided a general map of the spurious image stress as a function of simulation cell size, aspect ratio and bow-out for both nominally edge and screw dislocations. we achieved this using an approximate image solution of the resulting boundary value problem as well as an analytic model that captures most of the spurious image effects. A unique simulation cell shape is found to minimize spurious image effects for a fixed simulation volume (i.e. fixed total number of atoms) and specified initial dislocation line length. We used the results to estimate image stress effects in various literature studies involving dislocation bow-out. The image effects are non-negligible. Several case studies involving simulation cell dimensions were shown to converge due to a near-zero scaling of the image stress with respect to the simulation cell dimensions used. Finally, we made a direct comparison between a dislocation bow-out configuration under an applied load in a finite simulation cell and an image-free multiscale simulation of the same problem and the difference was shown to be

consistent with our estimated image stresses. Overall, the results here provide guidance for both the development and interpretation of quantitative molecular dynamics studies involving curved dislocation structures.

In chapter 5, we examined the line tension Γ of a dislocation which is an important and fundamental property ubiquitous to continuum scale models of metal plasticity. However, the precise value of Γ in a given material has proven difficult to assess, with literature values encompassing a wide range. We presented results from a multiscale simulation and robust analysis of the dislocation line tension, for dislocation bow-out between pinning points, for two widely-used interatomic potentials for Al. A central part of the analysis involves an effective Peierls stress applicable to curved dislocation structures that markedly differs from that of perfectly straight dislocations but is required to describe the bow-out both in loading and unloading. The line tensions for the two interatomic potentials are similar and provide robust numerical values for Al. Most importantly, the atomic results show notable differences with singular anisotropic elastic dislocation theory in that (i) the coefficient of the ln(L) scaling with dislocation length, L, differs and (ii) the ratio of screw to edge line tension is smaller than predicted by anisotropic elasticity. These differences are attributed to local dislocation core interactions that remain beyond the scope of elasticity theory. The many differing literature values for Γ are attributed to various approximations and inaccuracies in previous approaches. The results here indicate that continuum line dislocation models, based on elasticity theory and various core-cut-off assumptions, may be fundamentally unable to reproduce full atomistic results, thus hampering the detailed predictive ability of such continuum models.

In summary, this work has accomplished (i) the demonstration of size and dimensionality effects in metal plasticity where a purely continuum description lacking any material length scale is insufficient to describe the plastic behavior, and (ii) the reconciliation of discrepancies between a continuous elastic (DDD) line tension model and that computed directly from Molecular Statics Simulations.

This work was accomplished through the usage of DDD and MS simulations as well as simple analytical models. Despite the three examples presented within this thesis providing insight, all of this work demonstrates the need for a better, more general understanding of the interactions between dislocations and both interfaces and obstacles for better design of engineering materials.

Bibliography

[1] Tylecote RF. *A History of Metallurgy*. Maney Publishing, 2^{nd} edition, 1992.

[2] Kaufman B. Metallugy and ecological change in the ancient near east. *Backdirt*, pages 86 – 92, 2011.

[3] Agricola G. *De re Metallica*. Dover Books, 1556.

[4] Rehren T, Belgya T, Káli G, Kasztovszky Z, Kis Z, Kovács I, Maróti B, Martinón-Torres M, Miniaci G, Pigott VC, Radivojević M, Rosta L, Szentmiklósi L, and Szókefalvi-Nagy Z. 5,000 years old egyptian iron beads made from hammered meteoritic iron. *Journal of Archaeological Science*, 40:4785 – 4792, 2011.

[5] Frenkel J. Zur theorie der elastizitätsgrenze und der festigkeit kristalinischer körper. *Zeitschrift für Physik*, 37:572 – 609, 1926.

[6] Tinder RF and Washburn J. The initiation of plastic flow in copper. *Acta Metallurgica*, 12:129 – 137, 1964.

[7] Volterra V. Sur l'equilibre des corps élastiques multiplement connexes. *Annales Scientifiques de l'École Normale Supérieure*, 24:401 – 517, 1907.

[8] Hirth JP and Lothe J. *Theory of Dislocations*. Wiley, 1982.

[9] Dash WC. Growth of silicon crystals free from dislocations. *Journal of Applied Physics*, 30:459 – 474, 1959.

[10] Hall EO. The deformation and ageing of mild steel: Iii discussion of results. *Proceedings Physical Society B*, 64:747 – 753, 1951.

[11] Petch NJ. The cleavage strength of polycrystals. *Journal Iron Steel Institute of London*, 173:25 – 28, 1953.

[12] Plimpton S. Fast parallel algorithms for short-range molecular-dynamics. *Journal of Computational Physics*, 117:1 – 19, 1995.

[13] Möller JJ and Bitzek E. Comparative study of embedded atom potentials for atomistic simulations of fracture in α-iron. *Modelling and Simulation in Materials Science and Engineering*, 22:045002, 2014.

[14] Cheng Y, Bitzek E, Weygand D, and Gumbsch P. Atomistic simulation of dislocation-void interactions under cyclic loading. *Modelling and Simulation in Materials Science and Engineering*, 18:025006, 2010.

[15] Hatano T and Matsui H. Molecular dynamics investigation of dislocation pinning by a nanovoid in copper. *Physical Review B*, 72:094105, 2005.

[16] Robach JS, Robertson IM, Lee HJ, and Wirth BD. Dynamic observations and atomistic simulations of dislocation-defect interactions in rapidly quenched copper and gold. *Acta Materialia*, 54:1679–1690, 2006.

[17] Osetsky YN and Bacon DJ. Comparison of void strengthening in fcc and bcc metals: Large-scale atomic-level modelling. *Materials Science & Engineering A*, 400-401:374–377, 2005.

[18] Osetsky YN and Bacon DJ. An atomic-level model for studying the dynamics of edge dislocations in metals. *Modelling and Simulation in Materials Science and Engineering*, 11:427–446, 2003.

[19] Osetsky YN, Bacon DJ, and Mohles V. Atomic modelling of strengthening mechanisms due to voids and copper precipitates in α-iron. *Philosophical Magazine*, 83:3623–3641, 2003.

[20] Schmauder S and Kohler C. Atomistic simulations of solid solution strengthening of α-iron. *Computational Materials Science*, 50:1238–1243, 2011.

[21] Rodney D. Molecular dynamics simulation of screw dislocations interacting with interstititial frank loops in a model fcc crystal. *Acta Materialia*, 52:607–614, 2004.

[22] Rodney D and Martin G. Dislocation pinning by glissile interstitial loops in a nickel crystal: A molecular-dynamics study. *Physical Review B*, 61:8714–8725, 2000.

[23] Olmsted DL, Hector Jr. LG, and Curtin WA. Molecular dynamics study of solute strengthening in al/mg alloys. *Journal of the Mechanics and Physics of Solids*, 54:1763–1788, 2006.

[24] Golubov SI, Osetsky YN, and Stoller RE. Void hardening in bcc-iron studied by atomic-scale modelling. *Unpublished*, pages 108 – 111.

[25] Van Swygenhoven H, Derlet PM, and Froseth AG. Stacking fault energies and slip in nanocrystalline metals. *Nature Materials*, 3:399 – 403, 2004.

[26] Brandl C, Derlet PM, and Van Swygenhoven H. General-stacking-fault energies in highly strained metallic environments: *Ab initio* calculations. *Phys. Rev. B*, 76:054124, Aug 2007.

[27] Brandl C, Derlet PM, and Van Swygenhoven H. Strain rates in molecular dynamics simulations of nanocrystalline metals. *Philosophical Magazine*, 89:3465 – 3475, 2009.

[28] Froseth AG, Van Swygenhoven H, and Derlet PM. The influence of twins on the mechanical properties of nc-al. *Acta Materialia*, 52:2259 – 2268, 2004.

[29] Bitzek E, Brandl C, Derlet PM, and Van Swygenhoven H. Dislocation cross-slip in nanocrystalline fcc metals. *Physical Review Letters*, 100:235501 – 235505, 2008.

[30] Bitzek E, Derlet PM, Anderson PM, and Van Swygenhoven H. The stress-strain response of nanocrystalline metals: A statistical analysis of atomistic simulations. *Acta Materialia*, 56:4846 – 4857, 2008.

[31] Froseth AG, Derlet PM, and Van Swygenhoven H. Twinning in nanocrystalline fcc metas. *Advanced Engineering Materials*, 7:16 – 20, 2005.

[32] Farkas D, Froseth AG, and Van Swygenhoven H. Grain boundary migration during room temperature deformation of nanocrystalline Ni. *Scripta Materialia*, 55:695 – 698, 2006.

[33] Cai W, Athanasios A, Weinberger CR, and Bulatov VV. A non-singular continuum theory of dislocations. *Journal of Mechanics and Physics of Solids*, 54:561 – 587, 2006.

[34] Arsenlis A, Cai W, Tang M, Rhee M, Oppelstrup T, Hommes G, Pierce TG, and Bulatov VV. Enabling strain hardening simulations with dislocation dynamics. *Modelling and Simulation in Materials Science and Engineering*, 15:553 – 595, 2007.

[35] Devincre B and Kubin LP. Mesoscopic simulations of dislocations and plasticity. *Materials Science and Engineering: A*, 234:8 – 14, 1997.

[36] Leyson GPM, Curtin WA, Hector Jr LG, and Woodward CF. Quantitative prediction of solute strengthening in aluminum alloys. *Nature Materials*, 9:750 – 755, 2010.

[37] Dong Y, Nogaret T, and Curtin WA. Scaling of dislocation strengthening by multiple obstacle types. *Metallurgical and Materials Transactions A*, 41A:1954 – 1960, 2010.

[38] Bulatov VV, Hsiung LL, Tang M, Arsenlis A, Bartelt MC, Cai W, Florando JN, Hiratani M, Rhee M, Hommes G, Pierce TG, and Rubia TD. Dislocation multi-junctions and strain hardening. *Nature Letters*, 440:1174 – 1178, 2006.

[39] Bulatov V and Cai W. *Computer Simulations of Dislocations*. Oxford University Press, 1^{st} edition, 2006.

[40] Fitzgerald SP and Aubry S. Self-force on dislocation segments in anisotropic crystals. *Journal of Physics: Condensed Matter*, 22:295403, 2010.

[41] Peach M and Koehler JS. The forces exerted on dislocations and the stress fields produced by them. *Physical Revew*, 80:436 – 439, 1950.

[42] Kumar A and Kumble RG. Viscous drag on dislocations at high strain rates in copper. *Journal of Applied Physics*, 40:3475 – 3480, 1969.

[43] Liebfried G. Uber den einfluss thermisch angeregter schallwellen auf die plastische deformation. *Zeitschrift Fur Physik*, 127:344 – 356, 1950.

[44] Uchic MD, Dimiduk DM, Florando JN, and Nix WD. Sample dimensions influence strength and crystal plasticity. *Science*, 305:986 – 988, 2004.

[45] Nicola L, Xiang Y, Vlassak JJ, Van der Giessen E, and Needleman A. Plastic deformation of freestanding thin films: Experiments and modeling. *Journal of the Mechanics and Physics of Solids*, 54:2089 – 2110, 2006.

[46] Choi YS, Uchic MD, Parthasarathy TA, and Dimiduk DM. Numerical study on microcompression tests of anisotrpic single crystals. *Scripta Materialia*, 57:849 – 852, 2007.

[47] Dehm G, Motz C, Scheu C, Clemens H, Meyrhofer PH, and Mitterer C. Mechanical size-effects in miniaturized and bulk materials. *Advanced Engineering Materials*, 8:1033 – 1045, 2006.

[48] Benzerga AA and Shaver NF. Scale dependence of mechanical properties of single crystals under uniform deformation. *Scripta Materialia*, 54:1937 – 1941, 2006.

[49] Demir E, Raabe D, and Roters F. The mechanical size effect as a mean-field breakdown phenomenon: Example of microscale single crystal beam bending. *Acta Materialia*, 58:1876 – 1886, 2009.

[50] Motz C, Schöberl T, and Pippan R. Mechanical properties of micro-sized copper bending beams machined by the focused ion beam technique. *Acta Materialia*, 53:4269 – 4279, 2005.

[51] Fleck NA, Muller GM, Ashby MF, and Hutchinson JW. Strain gradient plasticity: Theory and experiment. *Acta Metall. Mater.*, 42:475 – 487, 1994.

[52] Gao H, Huang Y, Nix WD, and Hutchinson JW. Mechanism-based strain gradient plasticity-i. theory. *Journal of the Mechanics and Physics of Solids*, 47:1239 – 1263, 1999.

[53] Nix WD and Gao H. Indentation size effects in crystalline materials: A law for strain gradient plasticity. *Journal of the Mechanics and Physics of Solids*, 46:411 – 425, 1998.

[54] Acharya A and Bassani JL. Lattice incompatibility and a gradient theory of crystal plasticity. *Journal of the Mechanics and Physics of Solids*, 48:1565 – 1596, 2000.

[55] Gurtin ME. On the plasticity of single crystals: Free energy, microforces, plastic-strain gradients. *Journal of the Mechanics and Physics of Solids*, 48:989 – 1036, 1999.

[56] P Gudmundson. A unified treatment of strain gradient plasticity. *Journal of the Mechanics and Physics of Solids*, 52:1379 – 1406, 2004.

[57] Greer JR and Nix WD. Nanoscale gold pillars strengthened through dislocation starvation. *Physical Review B*, 73:245410, 2006.

[58] Nix WD, Greer JR, Feng G, and ET Lilleodden. Deformation at the nanometer and micrometer length scales: Effects of strain gradients and dislocation starvation. *Thin Solid Films*, 515:3152 – 3157, 2006.

[59] Greer JR, Oliver WC, and Nix WD. Size dependence of mechanical properties of gold at the micron scale in the absence of strain gradients. *Acta Materialia*, 53:1821 – 1830, 2005.

[60] Espinosa HD, Prorok BC, and Peng B. Plasticity size effectsin free-standing submicron polycrystalline fcc films subjected to pure tension. *Journal of the Mechanics and Physics of Solids*, 52:667 – 689, 2004.

[61] Greer JR and Nix WD. Size dependence of mechanical properties of gold at the sub-micron scale. *Applied Physics A*, 80:1625 – 1629, 2005.

[62] Parthasarathy TA, Rao SI, Dimiduk DM, Uchic MD, and Trinkle DR. Contribution to size effect of yield strength from the stochastics of dislocation source lengths in finite samples. *Scripta Materialia*, 56:313 – 316, 2007.

[63] Rao SI, Dimiduk DM, Tang M, Parthasarathy TA, Uchic MD, and Woodward C. Estimating the strength of single-ended dislocation sources in micron-sized single crystals. *Philosophical Magazine*, 87:4777 – 4794, 2007.

[64] Rao SI, Dimiduk DM, Parthasarathy TA, Uchic MD, Tang M, and Woodward C. Athermal mechanisms of size-dependent crystal flow gleaned from three-dimensional discrete dislocation simulations. *Acta Materialia*, 56:3245 – 3259, 2008.

[65] Gao H, Huang Y, and Nix WD. Modeling plasticity at the micrometer scale. *Naturwissenschaften*, 86:507 – 515, 1999.

[66] Taupin V, Varadhan S, Chevy J, Fressengeas C, Beaudoin AJ, Montagnat M, and Duval P. Effects of size on the dynamics of dislocations in ice single crystals. *Physical Review Letters*, 99:155507, 2007.

[67] Gruber PA, Solenthaler C, Arzt E, and Spolenak R. Strong single-crystalline au films tested by a new synchrotron technique. *Acta Materialia*, 56:1876 – 1889, 2008.

[68] Kiener D, Grosinger W, Dehm G, and Pippan R. A further step towards an understanding of size-dependent crystal plasticity: In situ tension experiments of miniaturized single-crystal copper samples. *Acta Materialia*, 56:580 – 592, 2008.

[69] Chakravarthy SS and Curtin WA. Stress-gradient plasticity. *Proceedings of the National Academy of Sciences of the United States of America*, 108:15716 – 15720, 2011.

[70] Chakravarthy SS and Curtin WA. Origin of plasticity length-scale effects in fracture. *Physical Review Letters*, 105:115502, 2010.

[71] Chakravarthy SS and Curtin WA. Effect of source and obstacle strengths on yield stress: A discrete dislocation study. *Journal of the Mechanics and Physics of Solids*, 58:625 – 635, 2010.

[72] Espinosa HD, Berbenni S, Panico M, and Schwarz KW. An interpretation of size-scale plasticity in geometrically confined systems. *Proceedings of the National Academy of Sciences of the United States of America*, 102:16933 – 16938, 2005.

[73] Senger J, Weygand D, Gumbsch P, and Kraft O. Discrete dislocation simulations of the plasticity of micro-pillars under uniaxial loading. *Scripta Materialia*, 58:587 – 590, 2007.

[74] Eshelby JD. Screw dislocations in thin rods. *Journal of Applied Physics*, 24:176 – 179, 1953.

[75] Motz C, Weygand D, Senger J, and Gumbsch P. Micro-bending tests: A comparison between three-dimensional discrete dislocation dynamics simulations and experiments. *Acta Materialia*, 56:1942 – 1955, 2008.

[76] Simmons G and Wang H. *Single Crystal Elastic Constants and Calculated Aggregate Properties. A Handbook*. The MIT Press, 2^{nd} edition, 1971.

[77] Grujicic M and Columbus D. A comparative discrete-dislocation/crystal-plasticity analysis of bending of a single-crystalline microbeam. *Journal of Materials Science*, 36:2179 – 2188, 2001.

[78] Picu RC and Zhang D. Atomistic study of pipe diffusion in al-mg alloys. *Acta Materialia*, 52:161–171, 2004.

[79] Velasco M, Van Swygenhoven H, and Brandl C. Coupled grain boundary motion in a nanocrystalline grain boundary network. *Scripta Materialia*, 65:151 – 154, 2011.

[80] Hasnaoui A, Derlet PM, and Van Swygenhoven H. Interaction between dislocations and grain boundaries under an indenter - a molecular dynamics simulation. *Acta Materialia*, 52:2251 – 2258, 2004.

[81] Rao S, Parthasarathy TA, and Woodward C. Atomistic simulation of cross-slip processes in model fcc structures. *Philosophical Magazine*, 79:1167 – 1192, 1999.

[82] Bitzek E, Derlet PM, and Van Swygenhoven H. Dislocation cross-slip in nanocrystalline fcc metals. *Physical Review Letters*, 100:235501, 2008.

[83] Warner DH, Curtin WA, and Qu S. Rate dependence of crack-tip processes predicts twinning trends in fcc metals. *Nature Materials*, 6:876 – 881, 2007.

[84] Zhang Y, Liu XY, Millett PC, Tonks M, Andersson DA, and Biner B. Crack tip plasticity in single crystal uo_2: Atomistic simulations. *Journal of Nuclear Materials*, 430:96 – 105, 2012.

[85] Patinet S and Proville L. Dislocation pinning by substitutional impurities in an atomic-scale model for Al(Mg) solid solutions. *Philosophical Magazine*, 91:1581–1606, 2011.

[86] Proville L, Rodney D, Brechet Y, and Martin G. Atomic-scale study of dislocation glide in a model solid solution. *Philosophical Magazine*, 86:3893 – 3920, 2006.

[87] Bacon DJ, Osetsky YN, and Rodney D. Dislocation-obstacle interactions at the atomic level. *Dislocations in Solids*, 15:1–90, 2009.

[88] Tapasa K, Osetsky YN, and Bacon DJ. Computer simulation of interaction of an edge dislocation with a carbon interstitial in α-iron and effects on glide. *Acta Materialia*, 55:93–104, 2007.

[89] Monnet G. Mechanical and energetical analysis of molecular dynamics simulations of dislocation-defect interactions. *Acta Materialia*, 55:5081–5088, 2007.

[90] Madec R, Devincre B, Kubin L, Hoc T, and Rodney D. The role of collinear interaction in dislocation-induced hardening. *Science*, 301:1879 – 1882, 2003.

[91] Xiong L, Xu S, McDowell D, and Chen Y. Concurrent atomistic-continuum simulations of dislocation-void interactions in fcc crystals. *International Journal of Plasticity*, 65:33 – 42, 2015.

[92] Shim J-H, Cho YW, Kwon SC, Kim WW, and Wirth BD. Screw dislocation assisted martensitic transformation of a bcc Cu precipitate in bcc Fe. *Applied Physics Letters*, 90:021906, 2007.

[93] Shim J-H, Kim D-I, Jung W-S, Cho YW, and Wirth BD. Strengthening of nanosized bcc Cu precipitate in bcc Fe: A molecular dynamics study. *Materials Transactions*, 50:2229 – 2234, 2009.

[94] Lee H-J and Wirth BD. Molecular dynamics simulation of the interaction between a mixed dislocation and a stacking fault tetrahedron. *Philosophical Magazine*, 89:821 – 841, 2009.

[95] Khater HA, Monnet G, Terentyev D, and Serra A. Dislocation glide in Fe-carbon solid solution: From atomistic to continuum level description. *International Journal of Plasticity*, 62:34 – 49, 2014.

[96] Rong Z, Bacon DJ, and Osetsky YN. Dynamics of drag of self-interstitial clusters by an edge dislocation in iron. *Materials Science and Engineering: A*, 400-401:378 – 381, 2005.

[97] Bitzek E and Gumbsch P. Atomistic study of drag, surface and intertial effects on edge dislocation in face-centered cubic materials. *Materials Science and Engineering: A*, 387 - 389:11 – 15, 2004.

[98] Bitzek E and Gumbsch P. Dynamic aspects of dislocation motion: Atomistic simulations. *Materials Science and Engineering: A*, 400 - 401:40 – 44, 2005.

[99] Domain C and Monnet G. Simulation of screw dislocation motion in iron by molecular dynamics simulations. *Physical Review Letters*, 95:215506, 2005.

[100] Needleman A and van der Giessen E. Discrete dislocation plasticity: A simple planar model. *Modelling and Simulation in Materials Science and Engineering*, 3:689 – 735, 1995.

[101] Weinberger CR, Aubry S, Lee SW, Nix WD, and Cai W. Modelling dislocations in a free-standing thin film. *Modelling and Simulation in Materials Science and Engineering*, 17:075007, 2009.

[102] Barber JR. *Elasticity*. Kluwer, 2^{nd} edition, 2002.

[103] Weinberger CR and Cai W. Computing image stress in an elastic cylinder. *Journal of The Mechanics and Physics of Solids*, 55:2027 – 2054, 2007.

[104] Daw MS, Baskes MI, Bisson CL, and Wolfer WG. Conf. modelling enviornmental effects on crack growth processes. In Jones RH Gerberich WW (Metallurgical Society Warrendale PA 1986), editor, *Conf. Modelling Enviornmental Effects on Crack Growth Processes*, pages 99 – 124, 1986.

[105] Daw MS, Foiles SM, and Baskes MI. The embedded-atom method: a review of theory and applications. *Materials Science Reports*, 9:251 – 310, 1993.

[106] JR Beeler. *Radiation Effects Computer Experiments*, volume 13. Amsterdam: North-Holland Publishing Company, 1983.

[107] Bitzek E, Koskinen P, Gahler F, Moseler M, and Gumbsch P. Structural relaxation made simple. *Physical Review Letters*, 97:170201, 2006.

[108] Tang Y and El-Awady A. Atomistic simulations of the interactions of hydrogen with dislocations in fcc metals. *Physical Review B*, 86:174102, 2012.

[109] Pavia F and Curtin WA. A parallel multiscale algorithm for 3d concurrent continuum/atomic simulations using lammps. *Submitted to: Modelling and Simulation in Materials Science and Engineering*, 2014.

[110] Weygand D, Friedman LH, Van der Giessen E, and Needleman A. Aspects of boundary-value problem solutions with three dimensional dislocation dynamics. *Modelling and Simulation in Materials Science and Engineering*, 10:437 – 468, 2002.

[111] Chou YT. Screw dislocation arrays in a plate. *Journal of Applied Physics*, 37:796 – 797, 1966.

[112] Nabarro FR and Kostlan EJ. The stress field of a dislocation lying in a plate. *Journal of Applied Physics*, 49:5445 – 5448, 1978.

[113] Kuykendall WP and Cai W. Conditional convergence in 2-dimensional dislocation dynamics. *Modelling and Simulation in Materials Science and Engineering*, 21:055003, 2013.

[114] Cai W, Bulatov VV, Chang J, Li J, and Yip S. Periodic image effects in dislocation modelling. *Philosophical Magazine*, 83:539 – 567, 2003.

[115] Ercolessi F and Adams JB. Interatomic potentials from first-principles calculations: The force-matching method. *Europhysics Letters*, 26:583 – 588, 1994.

[116] Dong Y. *Coupled Dislocation/Dislocation and Solute Strengthening Mechanisms in Metal Alloys*. PhD thesis, Brown University, 2013.

[117] Shilkrot LE, Miller RE, and Curtin WA. Coupled atomistic and discrete dislocation plasticity. *Physical Review Letters*, 89:025501, 2002.

[118] Osetsky YN, Bacon DJ, and Mohles V. Atomic modelling of strengthening mecanisms due to voids and copper precipitates in α-iron. *Philosophical Magazine*, 83:3623 – 3641, 2003.

[119] Rodney D. Activation enthalpy for kink-pair nucleation on dislocations: Comparison between static and dynamic atomic-scale simulations. *Physical Review B*, 76:144108, 2007.

[120] Terentyev D, Bacon DJ, and Osetsky YN. Interaction of an edge dislocation with voids in α-iron modelled with different interatomic potentials. *Journal of Physics: Condenseed Matter*, 20:445007, 2008.

[121] Proville L and Patinet S. Atomic-scale models for hardening in fcc solid solutions. *Physical Review B*, 82:054115, 2010.

[122] Dong Y and Curtin WA. Thermally activated plastic flow in the presence of multiple obstacle types. *Modelling and Simulation in Materials Science and Engineering*, 20:075006, 2012.

[123] Xu Z and Picu RC. Thermally activated motion of dislocations in fields of obstacles: The effect of obstacle distribution. *Physical Review B*, 76:094112, 2007.

[124] Van Swygenhoven H, Derlet PM, and Hasnaoui A. Atomistic modelling of strength of nanocrystalline metals. *Advanced Engineering Materials*, 5:345 – 350, 2003.

[125] Greer JR. Nanotwinned metals: It's all about imperfections. *Nature Materials*, 12:689 – 690, 2013.

[126] Weinberger CR and Cai W. Surface-controlled dislocation multiplication in metal micropillars. *Proceedings of the National Academy of Sciences*, 105:14304 – 14307, 2008.

[127] DeWit G and Koehler JS. Interactions of dislocations with an applied stress in anisotropic crystals. *Physical Review*, 116:1113 – 1121, 1959.

[128] Foreman AJE. The bowing of a dislocation segment. *Philosophical Magazine*, 15:1011 – 1021, 1966.

[129] Bacon DJ, Kocks UF, and Scattergood RO. The effect of dislocation self-interaction on the orowan stress. *Philosophical Magazine*, 28:1241 – 1263, 1978.

[130] Li P, Picu RC, and Weiss J. Dynamics below the depinning transition of interacting dislocations moving over fields of obstacles. *Physical Review E*, 82:022107, 2010.

[131] Rodney D and Phillips R. Structure and strength of dislocation junctions: An atomic level analysis. *Physical Review Letters*, 82:1704 – 1707, 1999.

[132] Nogaret T and Rodney D. Finite-size effects in dislocation glide through random arrays of obstacles: Line tension simulations. *Physical Review B*, 74:134110, 2006.

[133] Mott NF and Nabarro FRN. *Report on Strength of Solids*. Physical Society, London, 1948.

[134] Cottrell AH. *Dislocations and Plastic Flow in Crystals*. Clarendon Press, Oxford, 1953.

[135] Friedel K. *Dislocations*. Addison-Wesly Publishing Company, 1964.

[136] Dupuy L and Fivel MC. A study of dislocation junctions in fcc metals by an orientation dependent line tension model. *Acta Materialia*, 50:4873 – 4885, 2002.

[137] Wickham LK, Schwarz KW, and Stölken JS. Rules for forest interactions between dislocations. *Physical Review Letters*, 83:4574 – 4577, 1999.

[138] Khraishi TA, Zbib HM, and Rubia TD. The treatment of traction-free boundary condition in three-dimensional dislocation dynamics using generalized image stress analysis. *Materials Science and Engineering A*, 309:283 – 287, 2001.

[139] Brailsford AD. Effective line tension of a dislocation. *Physical Review*, 139:1813 – 1817, 1965.

[140] Shenoy VB and Phillips R. Finite-sized atomistic simulations of screw dislocations. *Philosphical Magazine A*, 76:367, 1997.

[141] Proville L, Ventelon L, and Rodney D. Prediction of the kink-pair formation enthalpy on screw dislocations in α-iron by a line tension model parameterized on empirical potentials and first-principles calculations. *Physical Review B*, 87:144106, 2013.

[142] Rodney D and Proville L. Stress-dependent peierls potential: Influence on kink-pair activation. *Physical Review B*, 79:094108, 2009.

[143] Zhou X, Ward DK, Wong BM, Doty PF, and Zimmerman JA. Molecular dynamics studies of dislocations in cdte crystals from a new bond order potential. *The Journal of Physical Chemistry*, 116:17563 – 17571, 2012.

[144] Szajewski BA and Curtin WA. Analysis of spurious image forces in atomistic simulations of dislocations. *Modelling and Simulation in Materials Science and Engineering*, 23:025006, 2015.

[145] Aubry S, Fitzgerald SP, and Arsenlis A. Methods to compute dislocation line tension energy and force in anisotropic elasticity. *Modelling and Simulation in Materials Science and Engineering*, 22:015001, 2014.

[146] Bacon DJ, Barnett DM, and Scattergood RO. Anisotropic continuum theory of lattice defects. *Progress in Materials Science*, 23:51 – 262, 1979.

[147] Barnett DM, Asaro RJ, Gavazza SD, Bacon DJ, and Scattergood RO. The effects of elastic anisotropy on dislocation line tension in metals. *J. Phys. F: Metal Phys.*, 2:854 – 864, 1972.

[148] Indenbom VL and Lothe J. *Elastic Strain Fields and Dislocation Mobility*. Number 31 in Modern Problems in Condensed Matter Sciences. North-Holland (March 1992), 1992.

[149] Mishin Y, Farkas D, Mehl MJ, and Papconstantopoulos DA. Interatomic potentials for monoatomic metals from experimental data and *Ab Initio* calculations. *Physical Review B*, 59:3393 – 33407, 1999.

[150] Li J. Atomeye: an efficient atomistic configuration viewer. *Modelling and Simulation in Materials Science and Engineering*, 11:173 – 177, 2003.

[151] Cash WD and Cai W. Dislocation contribution to acoustic nonlinearity: The effect of orientation-dependent line energy. *Journal of Applied Physics*, 109:01415, 2011.

[152] Kang K, Bulatov VV, and W Cai. Singular orientations and faceted motion of dislocations in body-centered cubic crystals. *Proceedings of the National Academy of Sciences of the United States of America*, 109:15174, 2012.